# Nano-scale Petrophysical Studies of The Gothic Shale Interval in the Paradox Basin, Colorado, U.S.A.

by:

Marvin Dunbar II

Presented to the Faculty of the Graduate School of

The University of Texas at Arlington in Fulfillment

of the Requirement

for the Degree of

MASTER OF SCIENCE IN GEOLOGY

THE UNIVERSITY OF TEXAS AT ARLINGTON

November 2017

# Acknowledgements

I would like to thank and acknowledge my thesis advisor, Dr. Qinhong Hu, as well as the thesis committee members who include, Dr. Naresh Kumar and Dr. John Wickham. Their guidance and insight were exceptional, making this thesis possible. Special thanks to the United States Geological Survey Core Repository Center who provided the samples to make this research possible, and Drillinginfo for providing a complementary subscription to Dr. Q.H. Hu's research group. I would also like to thank the other members associated with Dr. Hu's research group who helped me along the way, including Shawn Zhang, Golem Kibria, Ray Yang, and Scott Leaseburge. Furthermore, I would also like to express my gratitude to GeoMark Research for pyrolysis, and Weatherford Laboratories as well as Shimadzu Center at the University of Texas at Arlington for XRD measurement. Finally, I want to thank my family for their continual support and love while obtaining this achievement.

November 2, 2017

# Abstract

Nano-scale Petrophysical Studies of The Gothic Shale Interval in the Paradox Basin,

Colorado, U.S.A.

Marvin Dunbar II, MS

The University of Texas at Arlington, 2017

Supervising Professor: Qinhong Hu

Hydrocarbon production from shale has become a main energy source for the United States. Consequently, an increased knowledge of the petrophysical properties of shale such as porosity, permeability, tortuosity, and fluid-rock interactions (e.g., contact angle, imbibition) will improve production efficiency. Because of their minute size (nanoscale), the knowledge of pore structure (i.e., pore geometry and connectivity) has proven difficult to understand. Analyzing the pore size distribution and pore connectivity of Gothic Shale from selected locations in the Montezuma County of Colorado will lead to recommendations for greater oil production efficiency, fostering innovation into a thriving, environmentally safe, oil and gas industry.

This study investigated the pore structure and fluid interaction of Gothic Shale to understand the movement of hydrocarbon molecules in unconventional shale reservoirs, specifically focusing on the nano-scale pore geometry and connectivity of the organic matter and minerals, which are affected by maturity and mineralogy. In order to achieve this, a total of 10 core samples collected from four wells (A for 9-21 Antelope; KF for 1-4 Kissinger Federal; NF for 1-4 Norton Federal; UM for 44-34 Ute Mountain) received tests for organic carbon, pyrolysis, x-ray diffraction, contact angle, mercury injection capillary pressure, and fluid imbibition.

Pyrolysis results showed samples contained a percent carbonate from 42 – 69% with one outlier, sample UM8741, having a percent carbonate of 34%. TOC content varies within the dataset, containing values from 0.74 – 2.14. $T_{max}$ values ranged from 445 – 529ºC corresponding with a vitrinite reflectance range from 0.92 – 1.79. Most samples are classified as a type of carbonate mudstone (i.e. mixed or silica-rich) and are dominated by either calcite or dolomite minerals. Samples NF5913 and UM8741 deviated from the other samples and contained a majority of quartz, these samples were classified as a mixed mudstone.

Dependent upon the availability of sample size, contact angle and core plug porosity /permeability were conducted for selected samples. MICP results show that many of the samples have porosity that fell within 0.5-1.0%. The dataset had an average porosity of 0.593% with the lowest porosity, 0.224%, found in the NF5915 (5915 ft of 1-4 Norton Federal) sample, and the highest, 0.951%, in sample NF5871, both of which are calcite dominated carbonate mudstones. Most samples had pore types that were dominated by either micro-fractures, particularly 1-10 micrometer sized pores, or inter-clay platelet pores (2.8-5 nm sized pore-throats). Furthermore, no correlation was found between pore size distribution and mineralogy or maturity. Permeability values reached 1.378 mD for sample A5989; however, this was an exception. The average value of the dataset was 0.541 mD.

Contact angle results show both API brine and 10% IPA are good wetting fluids, however 10% IPA typically displays better wettability. For most samples, n-decane imbibition showed higher slopes for pore connectivity in the rock matrix, indicating that the pore system has a better connection to oil wetting fluids, the only exceptions being KF5898 and A5985. Correlations between mineralogy (clay, carbonates, quartz) and pore connectivity are found, and discussed in further detail.

# Table of Contents

# List of Illustrations

# List of Tables

# List of Equations

# Chapter 1 – Introduction

As a result of new drilling technologies (horizontal drilling) and production strategies (hydraulic fracturing), the development of additional oil and gas wells in unconventional reservoirs have seen an uptick in the United States. This has had a profound impact on the economic status of many cities and states in the United States, while also changing the energy sector throughout the world. However, innovation never stops. Questions now arise regarding the nature and connectivity of pores in unconventional hydrocarbon reservoirs with the expectation that answers will provide insight into more economic and efficient production methods.

The Paradox Basin has gained recognition for containing one of the largest oil fields in the United States, such as Aneth, which has produced over 440 million barrels of oil (Chidsey et al., 2009), as well as over one trillion cubic feet (TCF) of gas (Tesoro, 2014). The Gothic Shale interval is the most prevalent source rock in the region, while the Chimney Rock, Hovenweep, and Cane Creek Shales also generate hydrocarbons (Tesoro, 2014). Nevertheless, as of 2015, there were not many companies producing oil from shales in the region. Cabot Oil Corporation had only permitted one well in 2008, and Encana Oil and Gas permitted only one well in 2009. For perspective, the most active current player participant, Bill Barrett Corporation, has permitted 12 wells in the past two years (Tesoro, 2014).

In 2011, utilizing well and production data obtained from IHS Energy Group, the United States Geological Survey (USGS) assessed the amount of undiscovered oil and gas resources of the Paradox Basin (Anna et al, 2011). Four unconventional assessment units (Cane Creek, Chimney Rock, Hovenweep, and Gothic Shale) were estimated to hold an average of 471 million

barrels of oil (MMBO), 11,868 billion cubic feet of gas (BCFG), and 472 million barrels of natural gas liquids (MMBNGL) (Table 1-1).

**Table 1-1.** USGS Assessment results for potential unconventional oil and gas resources in the Paradox Basin (Anna et al., 2011). F95 represents a 95-percent chance of at least the amount tabulated; other fractiles are defined similarly.

| Total petroleum systems (TPS) and assessment units (AU) | Field type | Total undiscovered resources | | | | | | | | | | | |
|---|---|---|---|---|---|---|---|---|---|---|---|---|---|
| | | Oil (MMBO) | | | | Gas (BCFG) | | | | NGL (MMBNGL) | | | |
| | | F95 | F50 | F5 | Mean | F95 | F50 | F5 | Mean | F95 | F50 | F5 | Mean |
| Paradox Formation TPS | | | | | | | | | | | | | |
| Cane Creek Shale Oil AU | Oil | 103 | 198 | 382 | 215 | 84 | 175 | 364 | 193 | 6 | 14 | 31 | 15 |
| Cane Creek Shale Gas AU | Gas | | | | | 2,473 | 4,284 | 7,420 | 4,530 | 88 | 168 | 319 | 181 |
| Gothic, Chimney Rock, Hovenweep Shale Oil AU | Oil | 126 | 238 | 449 | 256 | 91 | 186 | 382 | 205 | 7 | 15 | 32 | 16 |
| Gothic, Chimney Rock, Hovenweep Shale Gas AU | Gas | | | | | 3,342 | 6,075 | 11,042 | 6,490 | 120 | 238 | 472 | 260 |
| Kaiparowits Plateau Coalbed Gas AU | Gas | | | | | 205 | 411 | 824 | 450 | 0 | 0 | 0 | 0 |
| Total continuous resources | | 229 | 436 | 831 | 471 | 6,195 | 11,131 | 20,032 | 11,868 | 221 | 435 | 854 | 472 |

In 2015, Hu and Ewing (2015a) noted that when low pore connectivity exists, topological factors in Barnett Shale have a more significant influence than the geometrical (pore size, shape, and distribution) factors. Focusing on the dynamics of pore topology in the Gothic Shale, this research aims to understand how the nano-sized pores affect the fluid flow and chemical transport.

# Chapter 2 – Geological Setting

Extending from the southeast corner of Colorado into the southwest corner of Utah, the black dolomitic shale is the main source of oil and gas recovered in the Paradox Basin (Figure 2-1). Thickness of this interval throughout the region varies from 80 to 150 feet, at depths ranging from 5500 – 8850 feet (Anna et al., 2011).

The Paradox Basin is an asymmetric foreland basin, located in the Colorado Plateau, and encompasses parts of Colorado, Utah, Arizona, and New Mexico. Halite and potash salts deposited during the Middle Pennsylvanian define the areal confines of the basin. The basin has a northwest-southeast orientation; it extends approximately 190 miles, and has a northeast-southwest width of approximately 95 miles (Figure 2-1, Condon, 1997).


**Figure 2-1**. Extent of Paradox Basin (Utah Geological Survey, 2014).

The northeast border of the basin is well-defined by the Uncompahgre Plateau, a broad anticline cored by Precambrian rocks (Figure 2-2). The San Juan Dome, an area that is partially covered by Tertiary volcanic rocks, marks the eastern boundary. The Hogback monocline that is located in the region of Durango, Colorado through northwestern New Mexico, defines the southeast end of the basin. Topographic and structural challenges exist in the south and southwestern part of the Paradox Basin leading to an ill-defined border near the Monument Upwarp and the Four Corners. Conversely, the San Rafael Swell restricts the northwest side, and the northern- most end of the basin merges with the south end of the Uinta Basin.

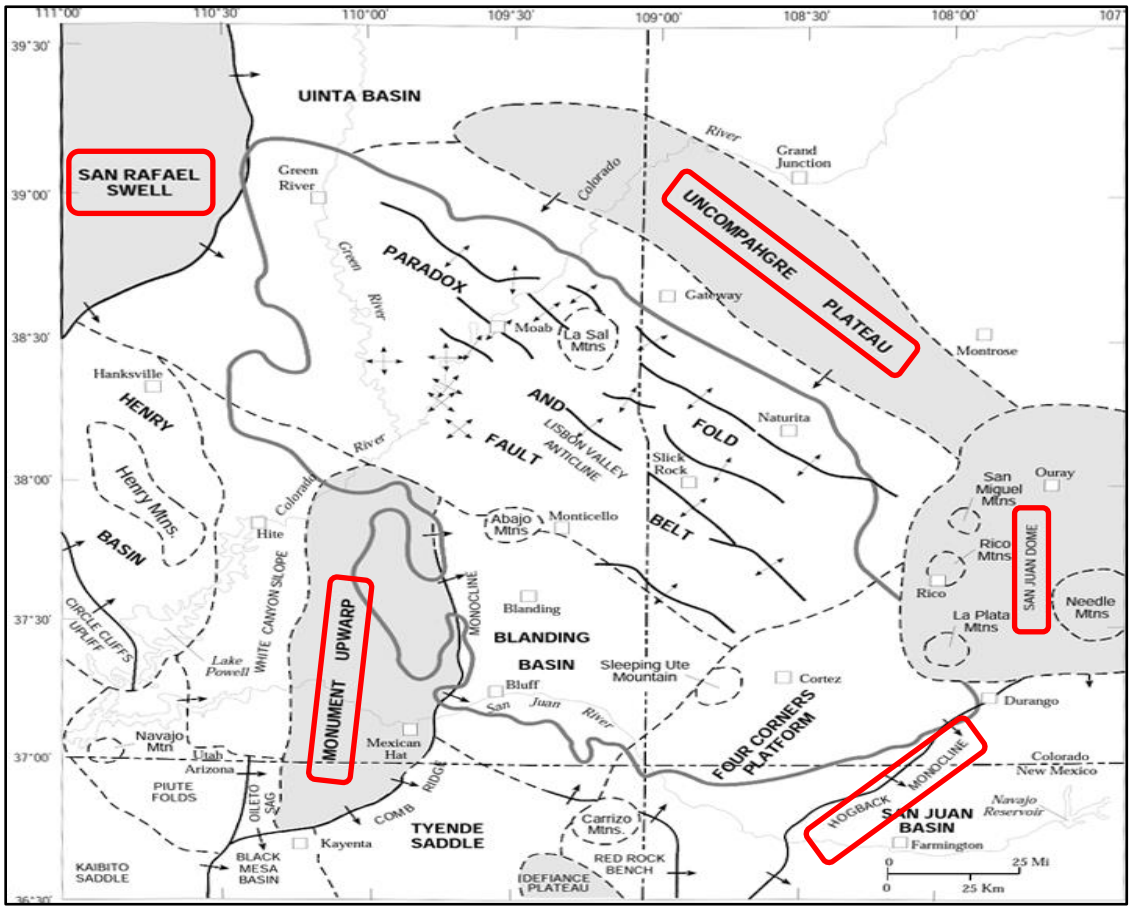


**Figure 2-2.** Map showing structural elements confining the Paradox Basin (modified from Kelley, 1958a; b).

Extensive research by Baars (1966; 1968) showed that the structure of the region was fixed by the Late Precambrian time and the tectonic features seen at the surface today were only modified by repeated reconfiguration of the basement structure. During the Precambrian, two major rift systems, the Olympic Wichita Lineament and the Colorado Lineament, formed the major structures of the Colorado Plateau (Baars, 1976; Figure 2-3). As time progressed into the Pennsylvanian, the Uncompahgre uplift and the Paradox Basin formed along the rift systems due to the East-West extension of the crust (Baars, 1981).

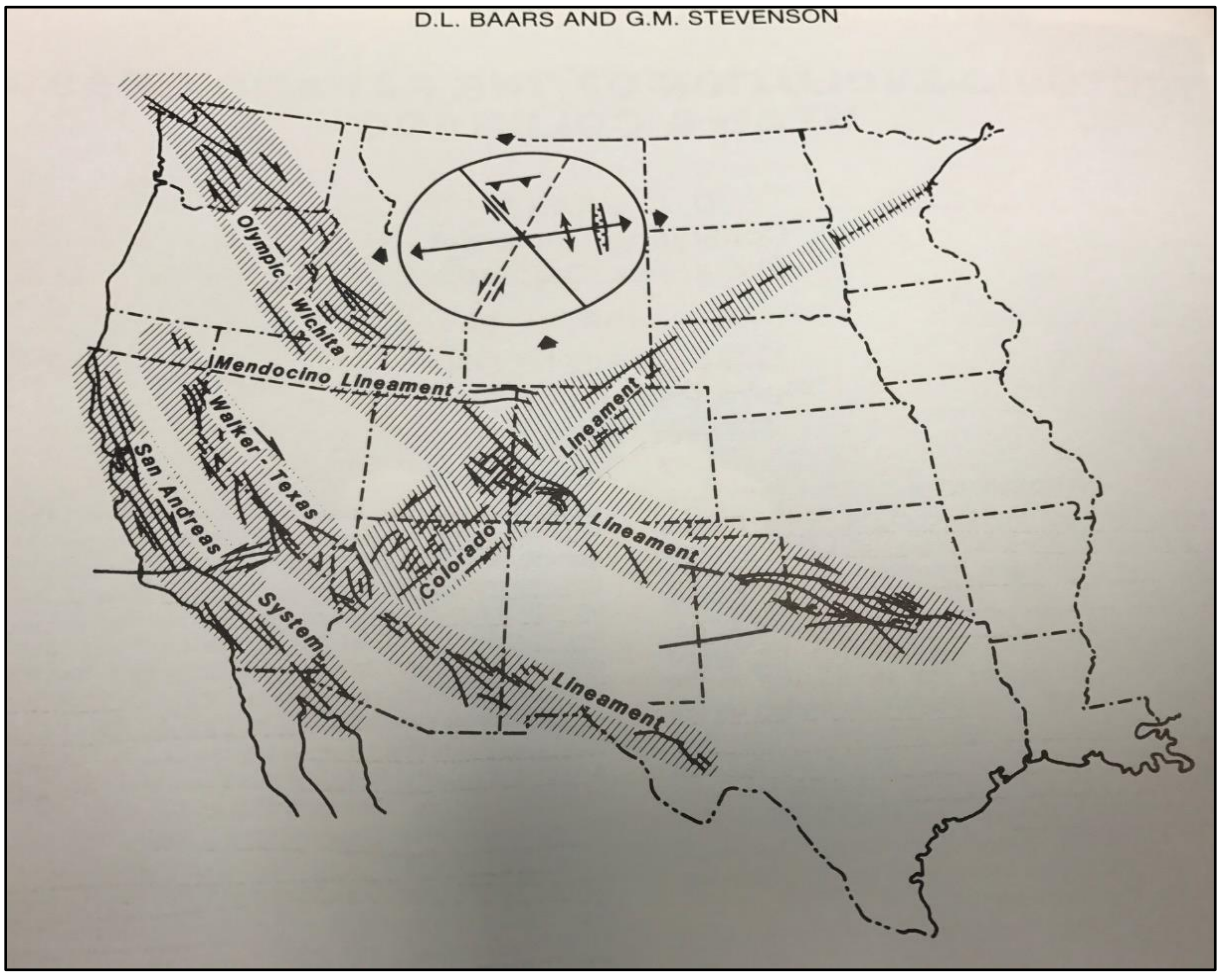


**Figure 2-3.** Map showing two major rift systems during the Precambrian that transected the now Paradox Basin as we know it today (Baars and Stevenson, 1981).

The Gothic Shale interval is part of the Paradox Formation; it overlies the Pinkerton Trail formation and underlies the Honaker Trail formation (the end members of the Hermosa Group; Figure 2-4). The Paradox Formation is a sequence of carbonate and evaporate cycles consisting of thick halite, together with anhydrite, gypsum, limestone, black dolomitic shale, and potash salts. Significant petroleum discoveries in the 1950s led to further subdivision of the Paradox Formation in the Four Corner area creating the four main intervals of Ismay, Desert Creek, Akah, and Baker Creek (Figure 2-4). There are 29 halite beds, each associated with a partial or complete cyclothem. The Gothic Shale unit is a part of evaporite cycle 3 in the Ismay interval, and is a marker between the Ismay interval and the Desert Creek interval (Figure 2-4).

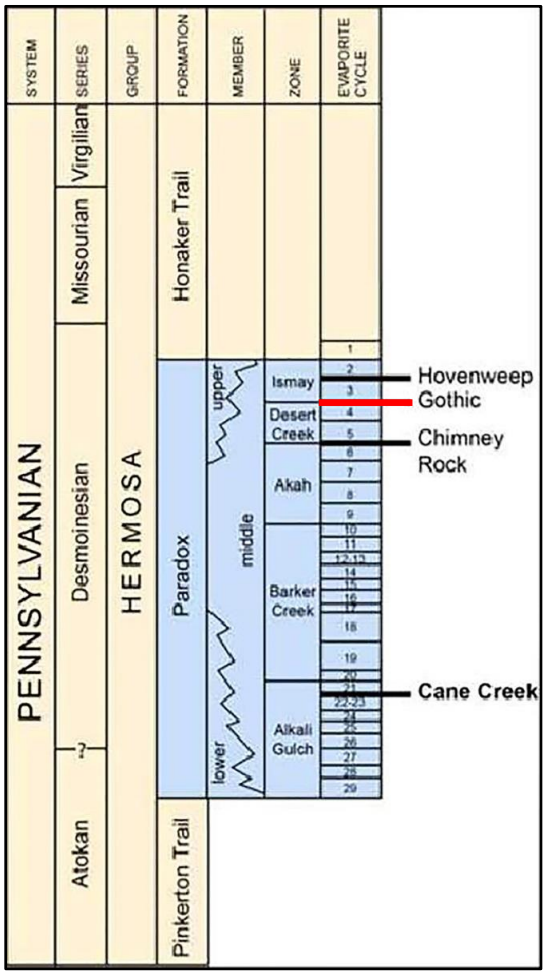


**Figure 2-4.** Stratigraphy of the Paradox Basin (Utah Geological Survey, 2014).

Previously mentioned in the studies of Herman and Sharp (1956), the Middle Pennsylvanian rocks in the Paradox Basin have classic lateral and vertical facies changes. Lateral changes from the evaporate basin onto the shelf carbonate are shown in Figure 2-5. Ideal vertical facies change of the evaporate 3 cycle (Lower Ismay) represents a depositional sequence of anhydrite, silty dolomite, black shale, dolomite, anhydrite, and halite. There is an abundance of black shale units, used as time markers in the Middle Pennsylvania strata of the Paradox Basin, making regional correlations easy. Furthermore, Hite (1967) showed the stratigraphy of each cycle correlates across the basin into the shelf carbonate facies. However, the Paradox Formation, is characterized by when the evaporite facies grades into the carbonate platform and evaporites no longer exist (Figure 2-6). When this occurs within the Hermosa Group, the Honaker Trail Formation cannot be differentiated from the Pinkerton Trail Formation (Figure 2-6).

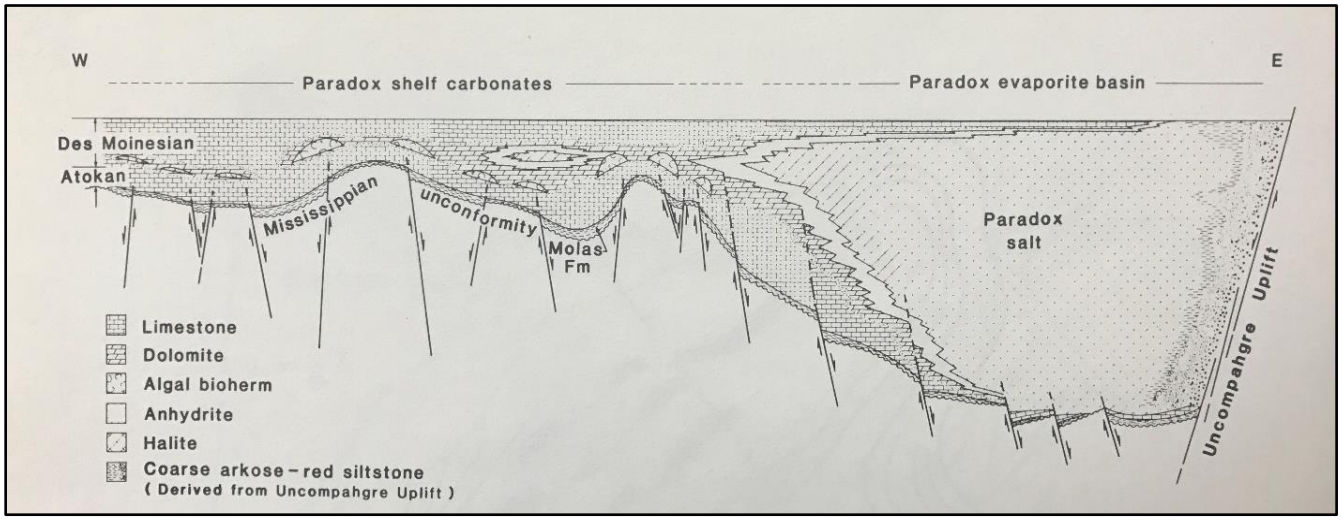


**Figure 2-5.** Lateral changes from the Paradox shelf carbonate to the Paradox evaporite basin (Baars and Stevenson, 1981).

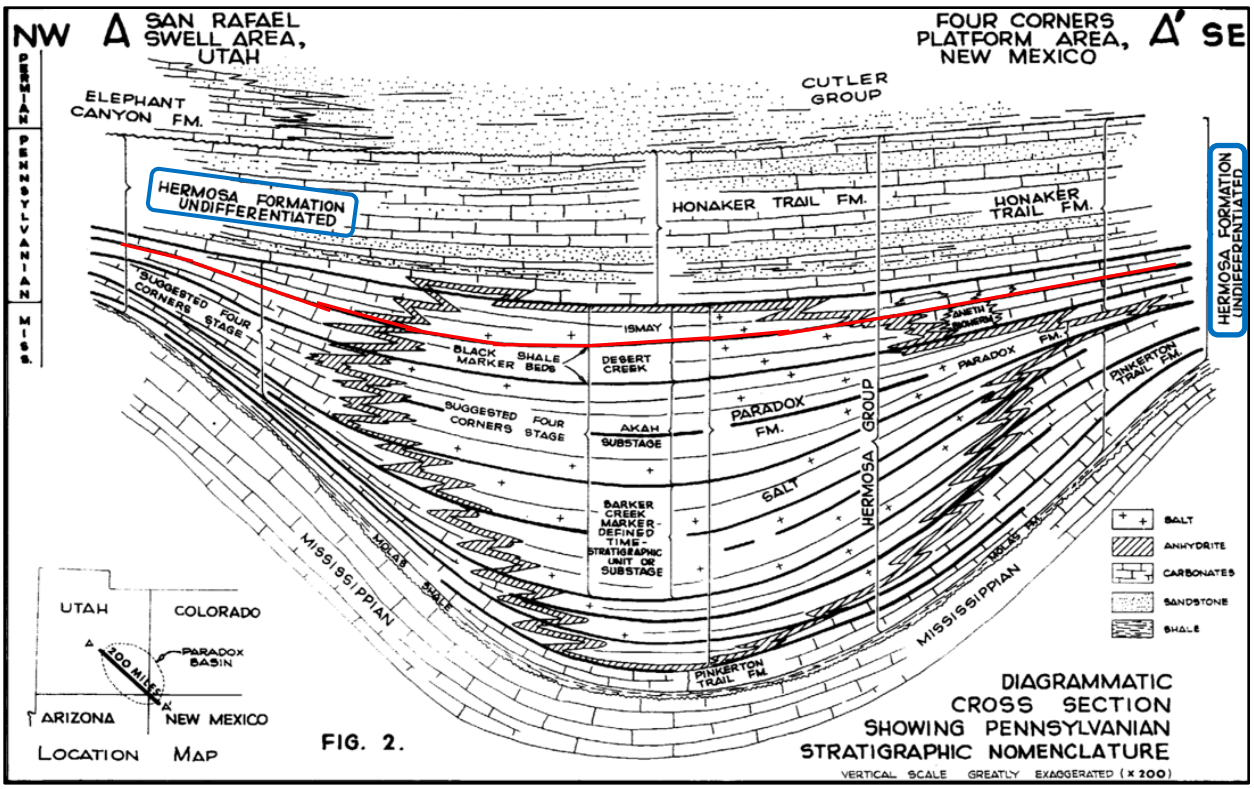


**Figure 2-6.** Cross section of Paradox Basin showing terminology and lithofacies. Gothic shale bed is highlighted red. (Baars et al., 1967).

# Chapter 3 – Methods

## *3-1 Sample Acquisitions*

To investigate the pore structure of Gothic Shale, core plugs obtained from core slabs were acquired from wells 1-4 Norton Federal (with an initial of NF in sample ID), 1-4 Kissinger Federal (KF), 44-34 Ute Mountain (UM), and 9-21 Antelope (A) from the USGS Core Repository; these wells are located within the Montezuma county of Colorado (Figure 3-1). Samples were chosen based on vitrinite reflectance, location, and depths resulting in different maturities, mineralogy, and potentially petrophysics characteristics. The depths of each core sample are identified, in feet, by the number in the sample name. Core plugs were measured and weighed to record their dimensions and mass before laboratory testing occurred (Table 3-1). Additionally, photos of each sample were taken with the USGS library number and sample depth documented on each (Figure 3-2). In these photos, a distinctively pink line was drawn on each sample to distinguish the orientation of the bedding plane (if any) as samples were cut. Previous work had been performed by Weatherford Laboratories on some of the samples, and this data being reported to USGS are incorporated into the data collected during this research, which is described in detail in this chapter.


**Figure 3-1.** Well locations from which core samples were taken.

To achieve research objectives, core samples were processed to different sizes to undergo tests of pyrolysis (powder), X-ray diffraction (powder), wettability (10 mm L × 10 mm W × 2 mm H slab), mercury injection capillary pressure (MICP, 1 cm-sided cube) and fluid imbibition (1 cm-sided cube).

**Table 3-1.** Dimensions of Gothic shale samples.

| Sample ID | Well Name | Depth (ft) | Diameter (cm) | Height (cm) | Weight (g) | Bulk Density (g/cm3) |
|---|---|---|---|---|---|---|
| A5985 | 9-21 Antelope | 5985 | 2.36 | 7.9 | 90.2 | 2.632 |
| A5989 | 9-21 Antelope | 5989 | 2.40 | 7.3 | 86.3 | 2.6188 |
| NF5871 | 1-4 Norton Federal | 5871 | 2.52 | 4.6 | 57.3 | 2.5369 |
| NF5873 | 1-4 Norton Federal | 5873 | 2.46 | 4.6 | 57.1 | 2.6468 |
| NF5913 | 1-4 Norton Federal | 5913 | 2.44 | 4.4 | 53.6 | 2.6383 |
| NF5915 | 1-4 Norton Federal | 5915 | 2.41 | 3.9 | 46.4 | 2.6583 |
| KF5898 | 1-4 Kissinger Federal | 5898 | 2.50 | 6.1 | 72.2 | 2.6256 |
| KF5901 | 1-4 Kissinger Federal | 5901 | 2.32 | 6.0 | 65.7 | 2.6156 |
| UM8741 | 44-34 Ute Mountain | 8741 | 2.42 | 3.7 | 42.6 | 2.5966 |

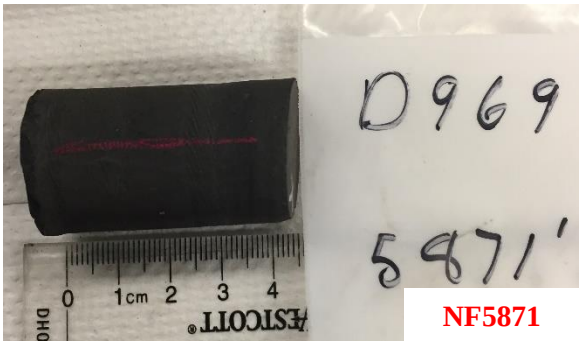

NF5871

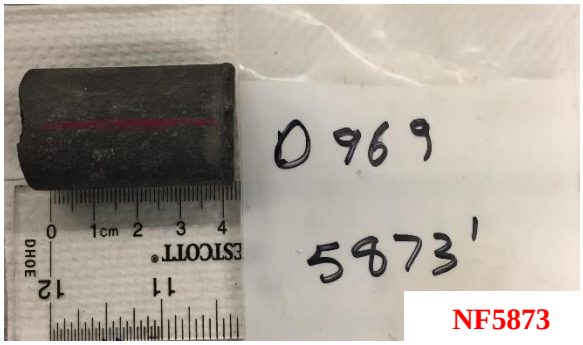

NF5873


**Figure 3-2.** Pictures showing core samples with sample ID in red.

*3-2 X-ray Diffraction Analysis for Mineralogy*

To obtain the mineralogy of the core samples approximately two to three grams of each sample were acquired using a Hi-Tech Diamond saw. Afterwards, core samples were crushed into powder form, using a mortar and pestle, then sieved with a mesh size of #200. The powder form was then sent to the Shimadzu Center at The University of Texas at Arlington for x-ray diffraction (XRD) analysis, with the procedure outlined in Appendix A - Methods and Procedures for X-ray Diffraction Analysis at the Shimadzu Center. Samples also had XRD analysis performed by Weatherford Laboratories and are described in Appendix B - Methods and Procedures of X-ray Diffraction Analysis at Weatherford Laboratories. The mineral percentages obtained were then used to calculate the lithology of each sample according to the sCore Lithofacies for organic mudrocks (Gamero-Diaz et al, 2013).

*3-3 Pyrolysis for Geochemistry*

Weatherford Laboratories executed pyrolysis and total organic carbon (TOC) data on most samples in this study, with the results provided from USGS. Other samples (A5985, NF5873, NF5913, and KF898) were sent to GeoMark Research to obtain their pyrolysis and TOC. The methods used for Weatherford Laboratories and GeoMark Research are described in detail in Appendix C and Appendix D, respectively.

The pyrolysis results include the percent carbonate, S1, S2, S3, $T_{max}$, and vitrinite reflectance. The measurement of free hydrocarbons before the sample is pyrolyzed is measured by the S1 peak. S2, the number of hydrocarbons that formed during the thermal pyrolysis, is used to approximate the remaining hydrocarbon generating potential of the sample. S3 represents the $CO_2$ produced during thermal breakdown of kerogen. $T_{max}$ is the temperature at which the

maximum rate of hydrocarbon generation occurs during pyrolysis as denoted by the peak of S2. Finally, vitrinite reflectance is calculated from $T_{max}$, which measures the thermal maturity (Jarvie, 2012). However actual vitrinite reflectance, the percentage of light reflected off the surface of vitrinite molecules, is available for only half of the samples via Weatherford Laboratories.

*3-4 Mercury Injection Capillary Pressure (MICP)*

Mercury injection capillary pressure is used to characterize the pore system. Characteristics such as bulk density, pore size distribution, porosity, total pore area, permeability and tortuosity are measured or estimated. These features help provide a greater understanding of the pore-throat size distribution and connectivity along with other attributes that affect fluid flow and productivity. Mercury, due to its nonwetting property, is used to invade pore throats of each sample. The nonwetting characteristic of mercury only allows external pressure to force the mercury into the pore space once the capillary pressure is exceeded (Gao and Hu, 2013). As greater pressure is applied, mercury can enter smaller pore throats. The MICP technique has been shown to explore a pore throat range down to 2.8 nm (Hu et al., 2017). The Washburn equation (Equation 3-1) allows for the determination of the pore throat radius, since the pore throat radius which is invaded remains inversely related to the applied external pressure (Washburn, 1921; Gao and Hu, 2013).

$$\Delta P = -\left(\frac{2\gamma \cos\theta}{R}\right) \quad \ldots\ldots (3.1)$$

Where;

$\Delta P$ = External pressure applied (psia);

$\gamma$ = Surface tension for mercury (dynes/cm);

$\theta$ = Contact angle between mercury and pore wall (degrees);

R = Pore throat radius (μm)

Since the original 1921 Washburn equation, new knowledge has been acquired that shows a constant contact angle and surface tension should not be assumed. In small pore throat diameters (<10 nm) the contact angle increases significantly as pore diameter decreases resulting in an error as high of 44% in small pore size distributions (Wang et al., 2016). A revised Washburn equation (Equation 3-2) is used to account for the variation in surface tension and contact angle (Wang et al., 2016).

$$\Delta P = -\frac{\left(2\gamma_{Hg}\,(R)\cdot\cos\theta_{Hg}\,(R)\right)}{R} \quad \ldots\ldots\ldots\ldots\ldots\ldots\ldots\ldots\ldots\ldots\ldots\ldots (3.2)$$

As previously mentioned, an estimation of permeability can be obtained from the MICP analysis as well. Permeability is indirectly derived from the MICP data via the Katz and Thompson equation (1986; 1987) (Equation 3-3).

$$K = \left(\frac{1}{89}\right)(L_{max})^2\left(\frac{L_{max}}{L_c}\right)\Phi S(L_{max}) \quad \ldots\ldots\ldots\ldots\ldots\ldots\ldots\ldots\ldots\ldots\ldots\ldots (3.3)$$

Where;

K = Absolute permeability ($\mu m^2$)

$L_{max}$ = Pore throat diameter when the hydraulic conductance is at its maximum (μm)

$L_c$ = Length of the pore throat diameter (μm) corresponding to the threshold pressure, which is determined from the inflection point of the cumulative intrusion curve

$\Phi$ = Porosity of sample (fraction)

S($L_{max}$) = Mercury saturation at $L_{max}$ (fraction)

*Procedure for Mercury Intrusion Capillary Pressure (MICP)*

Prior to samples being tested, 1 cm cube of sample is oven dried at 60 ºC for 24-48 hours then placed in a desiccator (~23 ºC) to allow for cooling in low relative humidity (10%). Afterwards the sample weight is documented. The sample, depending on its characteristics, is then inserted into a tool known as a penetrometer, which encompasses the sample and allows for the filling of mercury to take place. Before mercury fills the penetrometer, the penetrometer plus sample is weighed and recorded as well. These masses are inserted into the computer program under the analysis conditions before the low-pressure analysis is performed. After all the analysis conditions, such as filling pressure (5 psi, related to penetrometer), are entered into the computer, the low-pressure analysis is then performed. The Micromeritics Autopore IV 9510 (Figure 3-3) apparatus carries out the MICP analysis. In preparation for low pressure analysis, the sample is evacuated to 6.7 Pa (Hu et al., 2015b). Mercury then enters the penetrometer and may invade larger pores as the pressure rises from 5 psi to 30 psi, with an equilibration time of 10 sec for each pressure step. This first low-pressure assessment is to discover larger pores with an upper limit of approximately 50 μm in size, using a penetrometer suitable for samples with porosities around 0.5-5%.

Upon the completion of low-pressure analysis, the penetrometer and sample are removed from the low-pressure compartment of the machine and weighed, due to residual mercury not evacuating after the test. After documentation, the penetrometer is inserted into the high-pressure unit (Figure 3-3). Alongside the low-pressure parameters, the analysis conditions for the high-pressure run must be entered into the computer before the experiment resumes. A time of 30

seconds was set for the equilibration time. Once started, the pressure in the high-pressure unit will increase from 30 psi to 60,000 psi. The amount of intrusion is recorded and compared to the applied pressure throughout the process of both low and high-pressure analysis; whereas, the extrusion curve is only produced in the high-pressure analysis.

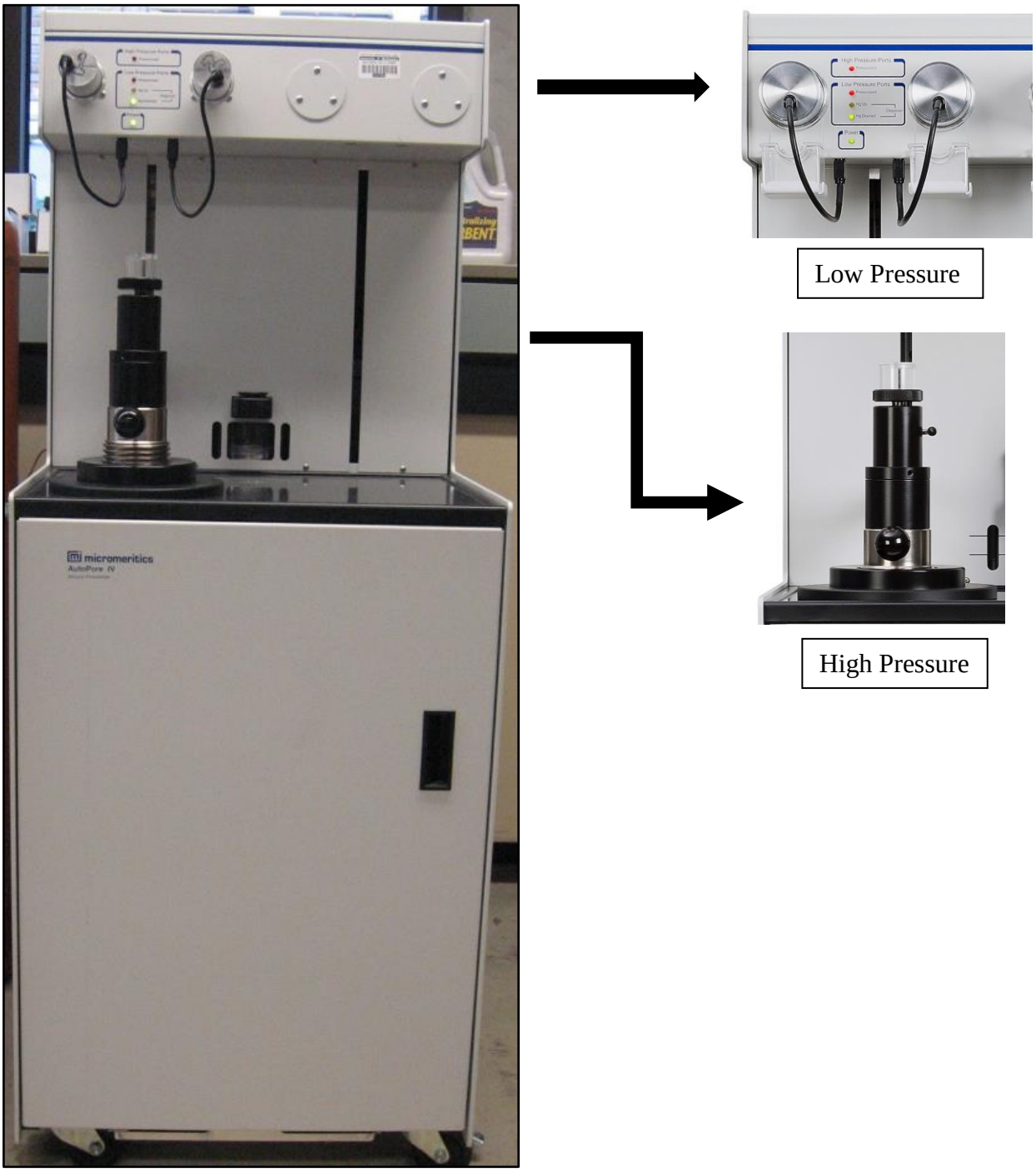


**Figure 3-3.** Micromeritics Autopore IV 9510.

### *3-5 Helium Porosity and Permeability*

Helium porosity and permeability were conducted by Chengdu University of Technology (CDUT) using the AP-608 Automated Porosimeter-Permeameter (Figure 3-4).

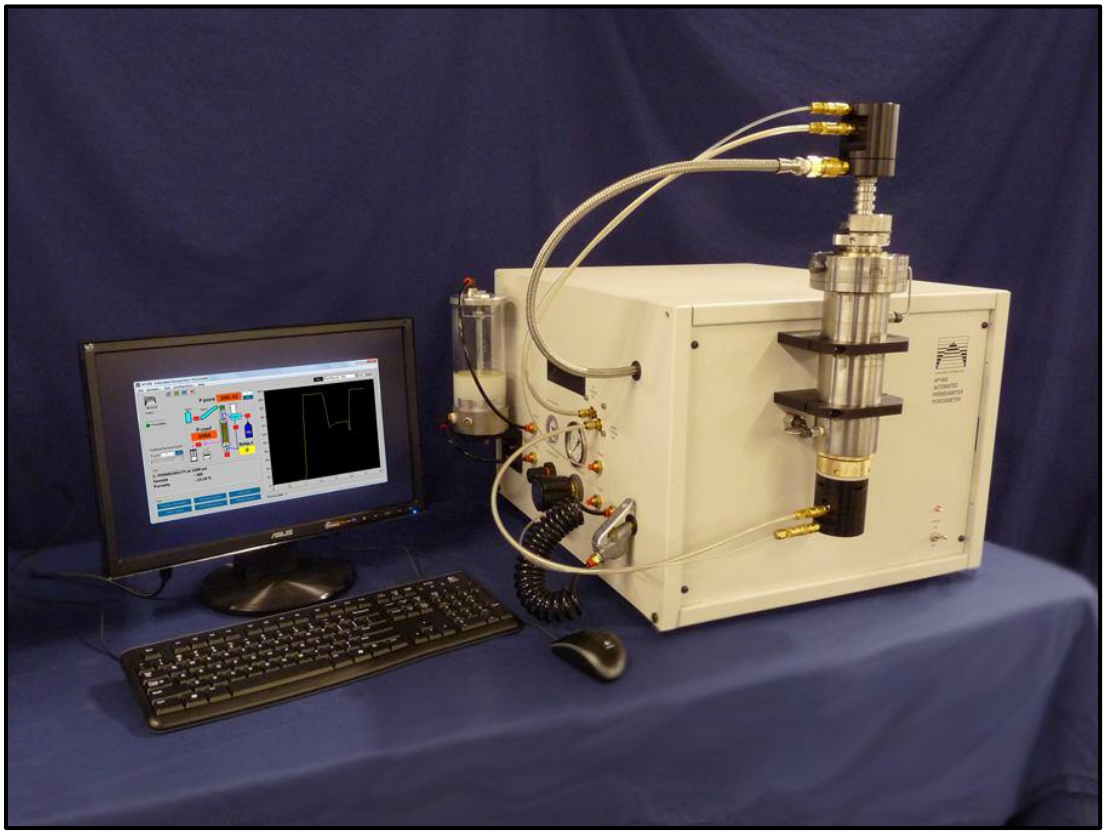

**Figure 3-4**. AP-608 Automated Porosimeter-Permeameter

When pressure is applied, the non-sorbing gas helium invades the pores. The AP-608 machine directly measures the pore volume for cylindrical core plugs by measuring the grain volume. Once the pore volume is obtained, the porosity can be calculated using Equation 3-4 if bulk volume is known (e.g., calculated from the dimensions of core plugs):

$$\Phi = \frac{PV}{BV} x\ 100 \ldots\ldots\ldots\ldots\ldots\ldots\ldots\ldots\ \ldots\ldots\ldots\ldots\ldots\ldots\ldots..(3.4)$$

Where;

$\Phi$ = porosity (%)

PV = pore volume ($cm^3$)

BV = bulk volume ($cm^3$)

The AP-608 apparatus uses the pressure-decay method to determine the Klinkenberg-corrected permeability. Shale samples consistently display low permeability, making the pulse-decay method viable in estimating permeability of a shale sample (API RP 40, 1998). This method only assumes Darcy flow during permeability test, so the gas slip effect is needed to consider differentiating gas permeability from that of liquids. Klinkenberg (1941) recognized gas slippage can be significant when the pore throat size is comparable to the mean free path of gas molecules. This gas slip effect was later called the Klinkenberg effect and included in his equation for permeability 3-5.

$$k_a = k_\infty \left(1 + \frac{b_k}{P_m}\right) \ldots\ldots\ldots\ldots\ldots\ldots\ldots\ldots\ldots\ldots\ldots\ldots\ldots\ldots\ldots\ldots (3.5)$$

Where;

$k_a$ = corrected permeability ($10^{-3}\ \mu m^2$)

$k_\infty$ = intrinsic permeability ($10^{-3}\ \mu m^2$)

$b_k$ = Klinkenberg factor (psi)

$P_m$ = mean pore pressure (psi)

To obtain $b_k$, the corrected permeability, ka, is measured at a minimum of three different mean pore pressures (API RP 40, 1998). The Klinkgenberg factor is found by Equation 3-6.

$$b_k = \frac{16c\mu}{w}\sqrt{\frac{2RT}{\pi M}} \ldots\ldots\ldots\ldots\ldots\ldots\ldots\ldots\ldots\ldots\ldots\ldots\ldots\ldots\ldots\ldots\ldots \quad (3.6)$$

Where;

c = constant typically taken as 0.9 (Wang et al., 2015)

μ = helium viscosity (Pa·s)

M = helium molecular weight (g/mol)

w = width of pore throat (μm)

R = universal gas constant (J/mol)

T = temperature (°C)

*Procedure for Helium Porosity and Permeability*

The Coretest Systems Operators Manual (2012) describes the procedure used when operating the AP-608 instrument. Initially, filling of the confining pressure system is required, a pressure setting for the confining fluid reservoir should be between 25 - 30 psi for optimal results. Then, a core sample is inserted into the core holder from the bottom and sealed. Once sealed a leak check are performed periodically by the software performed to insure good quality control. Afterwards, a reference volume calibration is completed to check for dead volume that may exist in the system. The system then applies 1,000 psi confining pressure to the core holder and 200 psi of pore pressure. After a stabilization period, valve 1 will close and the system will monitor for stability according to the parameters set in the configuration window (Figure 3-5). When the pressure has stabilized, P1 is recorded. Next, the volume adjuster will retract increasing the volume by a known, fixed amount. When the pressure has stabilized, P2 is recorded and the reference volume is calculated. A valid reference volume must be calculated before any

subsequent porosity or permeability measurements can be made. To begin a test, valve 1 will open to pressurize the system to the pressure specified in the configuration window. After one minute, valve 1 will close and the system will monitor for stability according to the parameters set in the configuration window. In cases of low permeability core, it may be necessary to reopen valve 1 to continue pressurization of the core. When the pressure has stabilized, the first pressure (P3) is recorded. Next, the volume adjuster will retract increasing the volume by a known, fixed amount. When the pressure has stabilized, the second pressure point (P4) is recorded and the pore volume is calculated.

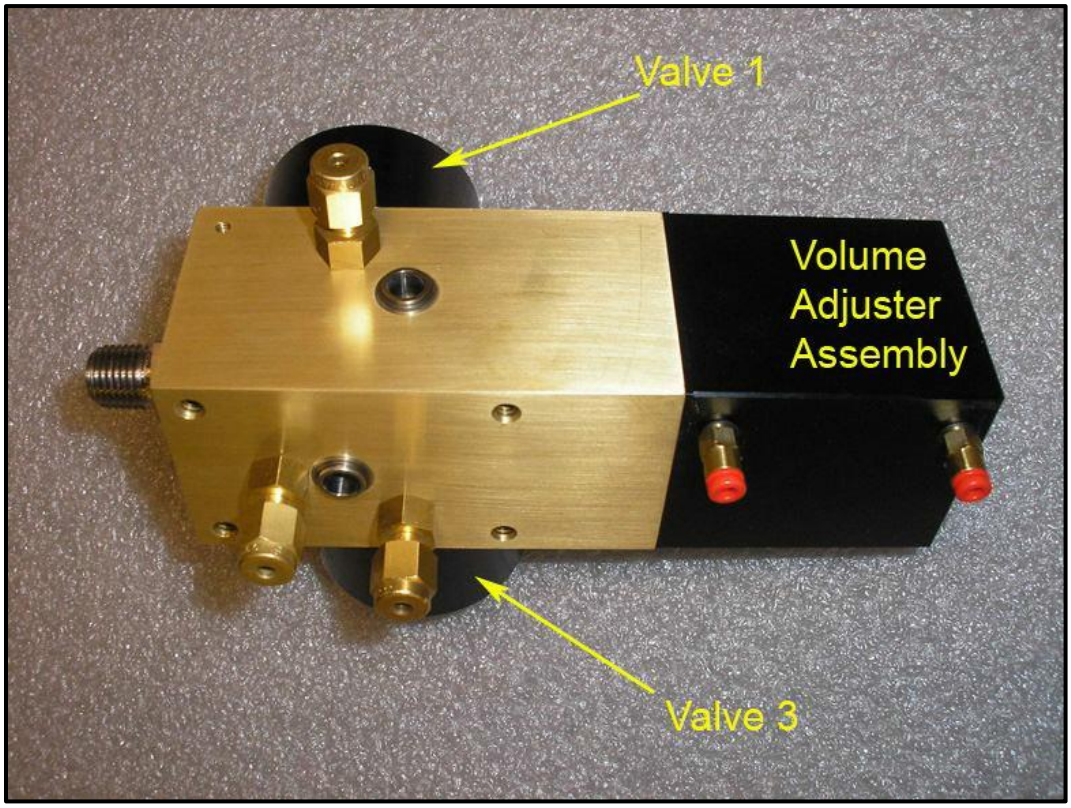


**Figure 3-5.** Valve's associated with the volume adjuster assembly.

*3-6 Contact Angle for Wettability*

The wettability of the rocks' surface was examined by first cutting two or three thin slabs (10 mm × 10 mm × 2-3 mm in size) of each sample, in order to apply API brine, and 10% IPA (isopropyl alcohol) in DI (deionized) water. These fluids were chosen with the purpose of showing the degree to which the rocks' surface is water wet (API brine) or oil wet (n-decane). A droplet of each fluid was placed on the rocks' surface where the angle of contact was measured and recorded as time progressed. The SL200 KB Optical Contact Meter apparatus was used for determining the contact angle (Figure 3-6). If the liquid is being absorbed by the sample surface, then this liquid is wetting the surface and there will be a small contact angle (<90). However, if the liquid rejects the surface of the rock and forms a bead, the surface is non-wetting to the liquid, and will have a greater contact angle (>90) (Figure 3-7).

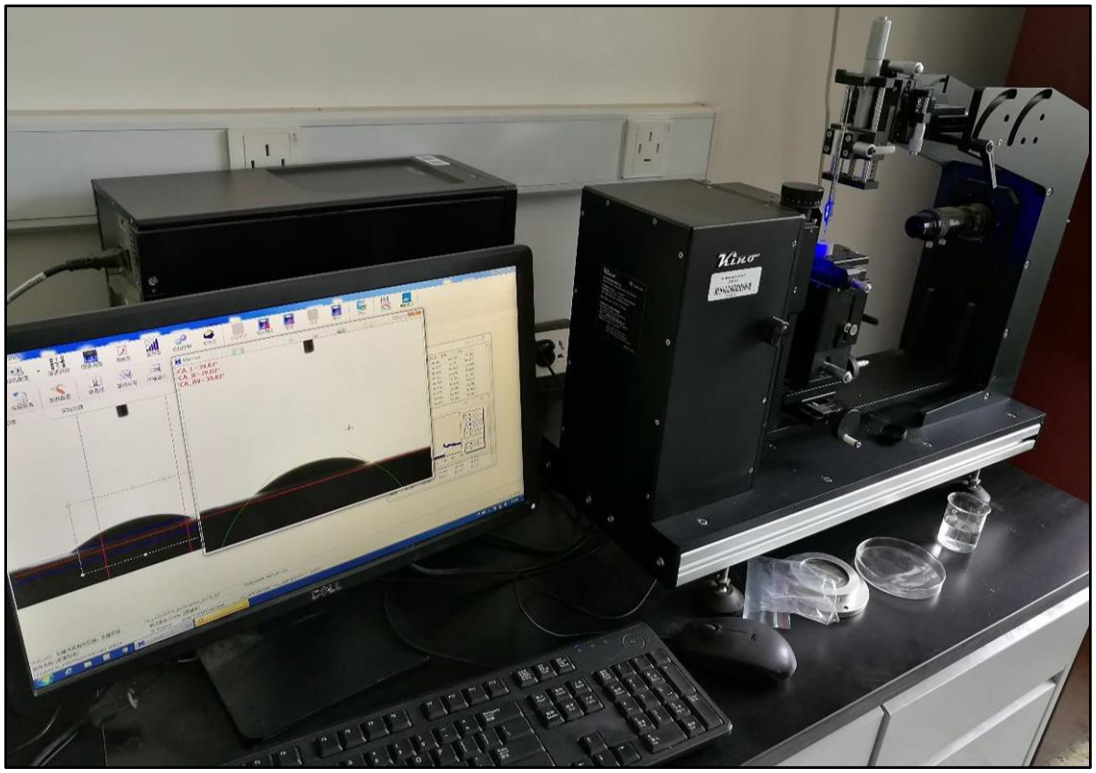

**Figure 3-6.** SL200 KB Optical Contact Angle Meter.

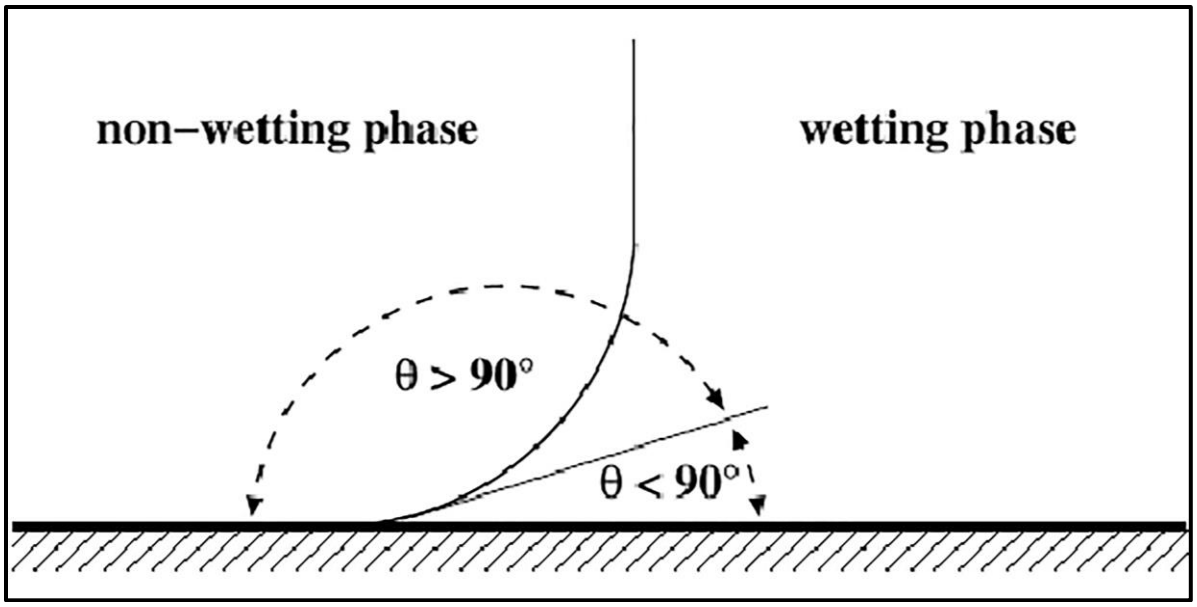


**Figure 3-7.** Contact angle relationship to wetting phase.

*3-7 Spontaneous Imbibition for Connectivity*

Spontaneous imbibition as described by Hu et al. (2012) is the process in which the nonwetting fluid (air) in a porous medium is displaced by a wetting fluid due to capillary forces. Imbibition test in this study measure the fluid uptake of both DI water and n-decane over a 24-hour period. The results of each imbibition test will give us a better understanding of the pore connectivity and interactions of the different fluids with each sample. As fluid is imbibed into the sample with time, the cumulative imbibition vs. time can be expressed by Equation 3-7.

$$I(t) = St^{0.5} \tag{3-7}$$

Where:

I(t) = Cumulative imbibition (mm)

S = Sorptivity ($mm/min^{0.5}$)

t = Time (min)

The slope of the log imbibed liquid mass versus log time allows for an estimation of pore connectivity (Hu et al., 2012). Generally, slopes greater than 0.5 are recorded at the beginning of the test due to edge accessible porosity affecting the wetting front. From there the slope decreases as the fluid enters further into the sample moving through the interior connected pore space. Upon finishing of the test, the slope will show either a well-connected pore system by having a value close to 0.5 (square-root-of-time relationship as described in Equation 3-1) or low connectivity with a value close to 0.25 (Hu et al., 2012).

*Procedure for Fluid Imbibition Tests*

Each core sample was dry cut, using a circular saw, into approximately two or three 1cm cubes. Afterwards, each cube had four sides epoxied, leaving just the bottom and top of the cube exposed, to minimize vapor absorption/evaporation of walls. Prior to any test being performed, individual cubes were oven dried at 60° C for 48 hours. After drying, the cubes would then be placed in a desiccator for 30 minutes to cool to room temperature. During the cooling process of the cubes, a petri dish filled with either DI water or n-decane was weighed. The mass was then recorded, and the petri dish was inserted into the imbibition chamber below the electronic microbalance. The cooled cube would also be weighed and recorded, along with the holder. This holder, which holds the sample firmly in place, is attached to a hook that is connected to the bottom of the balance. Once the holder and sample are securely emplaced, the chamber is closed. Next, an adjustable stage is moved vertically up, via a jack, until the sample encounters the fluid in the petri dish. An analytical microbalance (Shimadzu AUW 220D, with a resolution of 0.01 mg) records the weight change throughout the 24-hour period in which the experiment is run. This setup is demonstrated in Figure 3-8.

A)

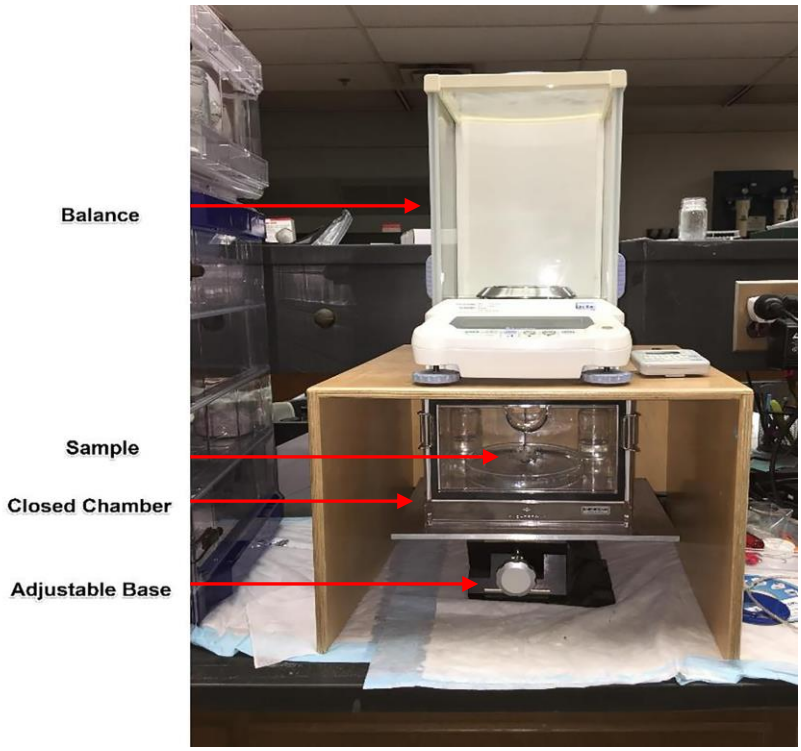


B)

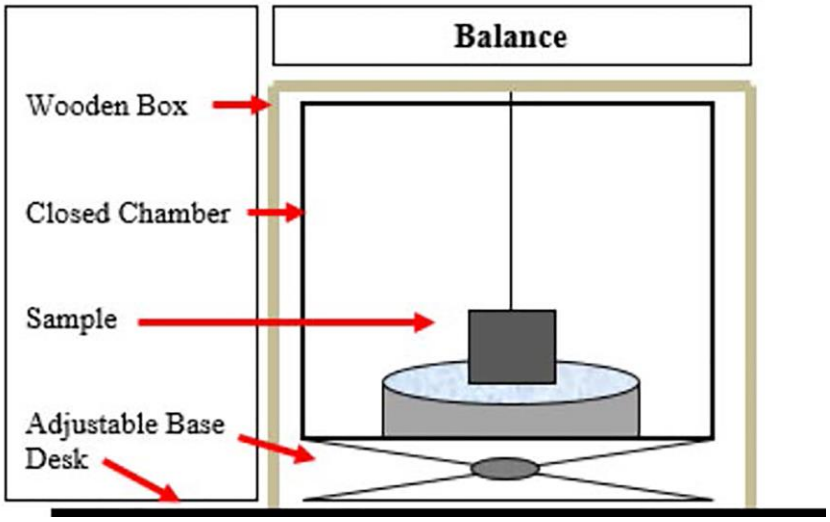


**Figure 3-8. A)** Picture of Imbibition testing system. **B)** Schematic view of imbibition testing arrangement.

The data collected is periodically recorded throughout the test by means of Excel. This is possible due to the balance allowing data to be sent to a computer at different time intervals resulting in the weight being documented throughout the test. During the first 2 minutes, the data is recorded for every 1 second time interval. Afterwards the time interval is changed to 30 seconds, until an hour of time passes. Finally, the time interval is set to 5 minutes until the remainder of the test is finish (~23 hours).

Upon the completion of an imbibition test, the holder and sample are detached from the hook so that the final weight can be determined then recorded. However, before the weight can be measured, residual excess fluid must be removed from the samples' surface. To accomplish this, a kimwipe slightly moistened with the imbibing liquid is weighed and then wiped across the face of the sample. The kimwipe absorbs the residual fluid and is then reweighed, after wiping. After documenting both weights, the sample and holder are both weighed and recorded, individually and together. Lastly, the petri dish is removed from the closed chamber to be weighed, allowing for the measurement of fluid loss. All the data is then processed and reviewed for pore connectivity and permeability analyses.

*3-8 Production Data*

A complimentary subscription from Drillinginfo provided to Dr. Qinhong Hu's research group gives access to production, completion, well logs, and other data analytics for wells. This allows data to be viewed and linked to petrophysical and geochemical studies performed in the lab.

# Chapter 4 – Results

## *4-1 Mineralogy*

Mineral composition of the samples contains of a majority of either calcite, dolomite, or quartz (Figure 4-1). However, other mineral traces can also be found, including pyrite, anhydrite, plagioclase, k-feldspar, muscovite, glauconite, siderite, ankerite, minrecordite, jacobsite, and clays such as illite, and chlorite (Table 4-1). The lithology of the samples, using the sCore lithofacies classification scheme for organic mudstones, is either a mixed mudstone, mixed carbonate mudstone, carbonate/siliceous mudstone, or silica-rich carbonate mudstone (Figure 4-2). Calcite- and dolomite-dominated samples have a silica-rich or mixed carbonate mudstone lithology; whereas, quartz-dominated samples are classified as a mixed mudstone (Figure 4-2).

A)

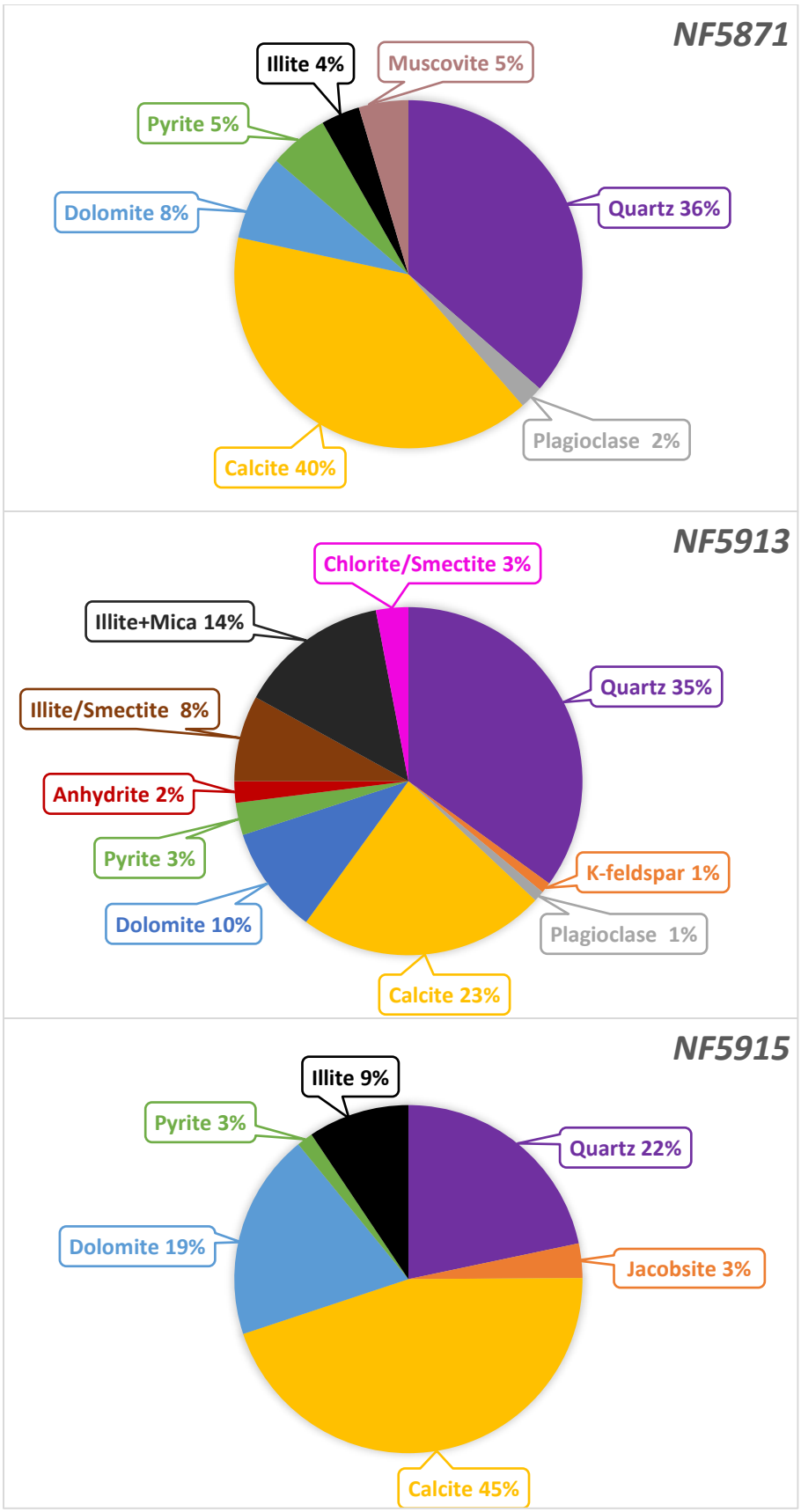
NF5871
Illite 4%
Muscovite 5%
Pyrite 5%
Dolomite 8%
Quartz 36%
Plagioclase 2%
Calcite 40%
NF5913
Chlorite/Smectite 3%
Illite+Mica 14%
Quartz 35%
Illite/Smectite 8%
Anhydrite 2%
Pyrite 3%
K-feldspar 1%
Dolomite 10%
Plagioclase 1%
Calcite 23%
NF5915
Illite 9%
Pyrite 3%
Quartz 22%
Dolomite 19%
Jacobsite 3%
Calcite 45%

B)

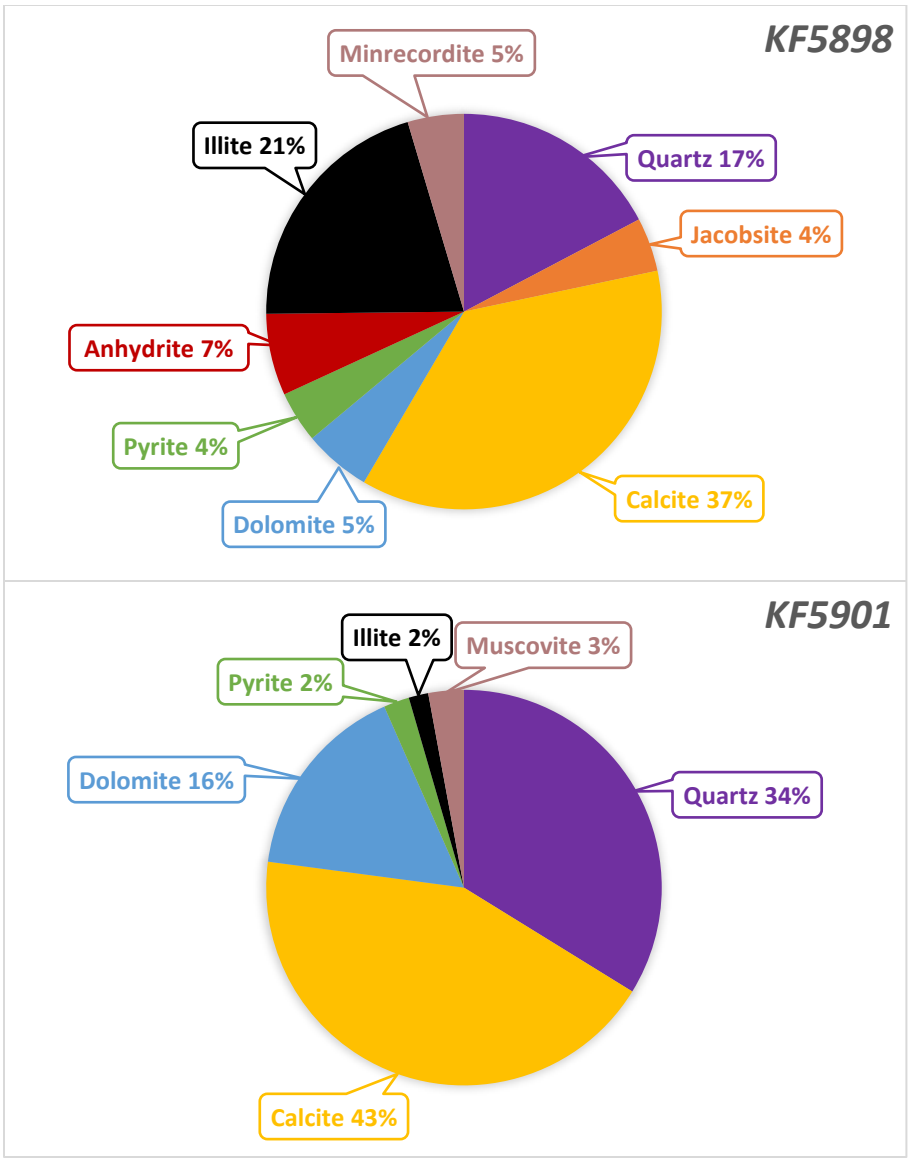
KF5898
Minrecordite 5%
Illite 21%
Quartz 17%
Jacobsite 4%
Anhydrite 7%
Pyrite 4%
Dolomite 5%
Calcite 37%
KF5901
Illite 2%
Muscovite 3%
Pyrite 2%
Dolomite 16%
Quartz 34%
Calcite 43%

C)

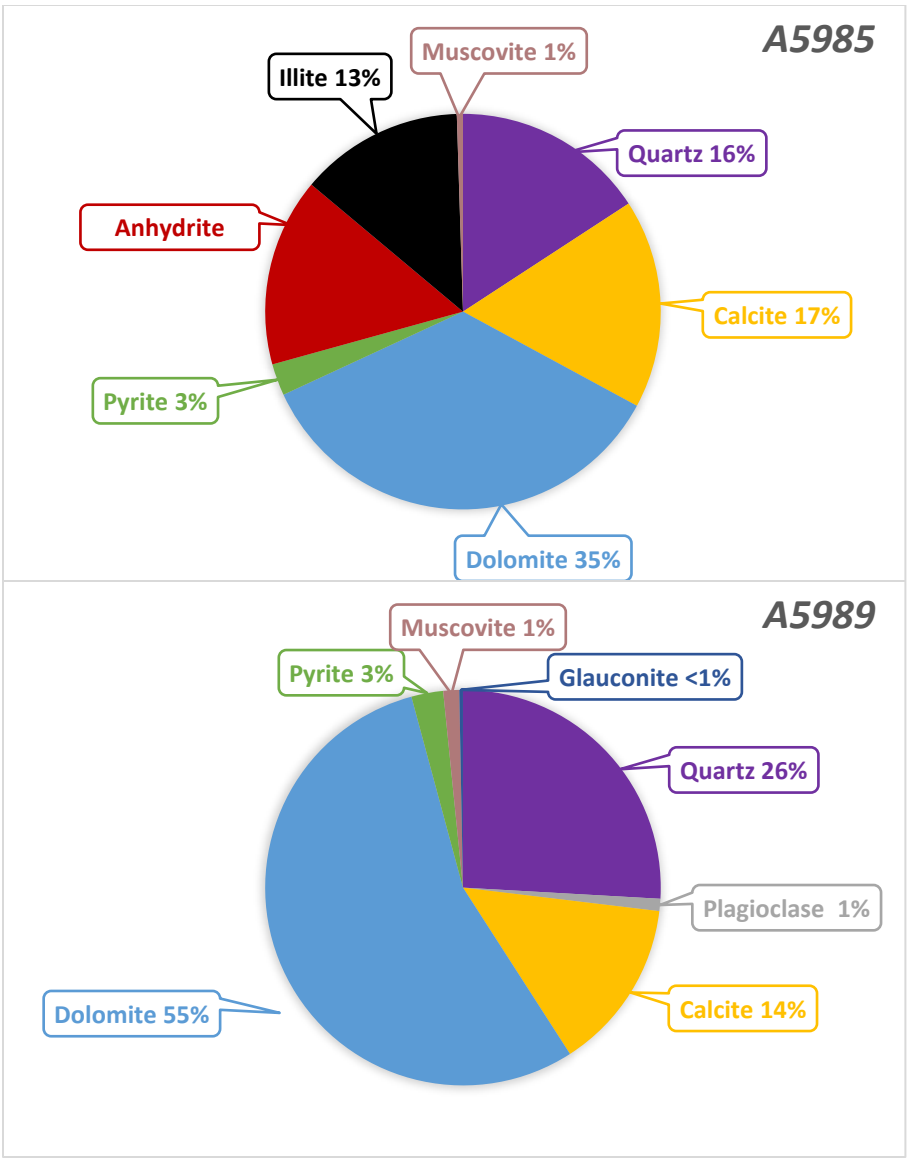
A5985
Muscovite 1%
Illite 13%
Quartz 16%
Anhydrite
Calcite 17%
Pyrite 3%
Dolomite 35%
A5989
Muscovite 1%
Pyrite 3%
Glauconite <1%
Quartz 26%
Plagioclase 1%
Dolomite 55%
Calcite 14%

D)

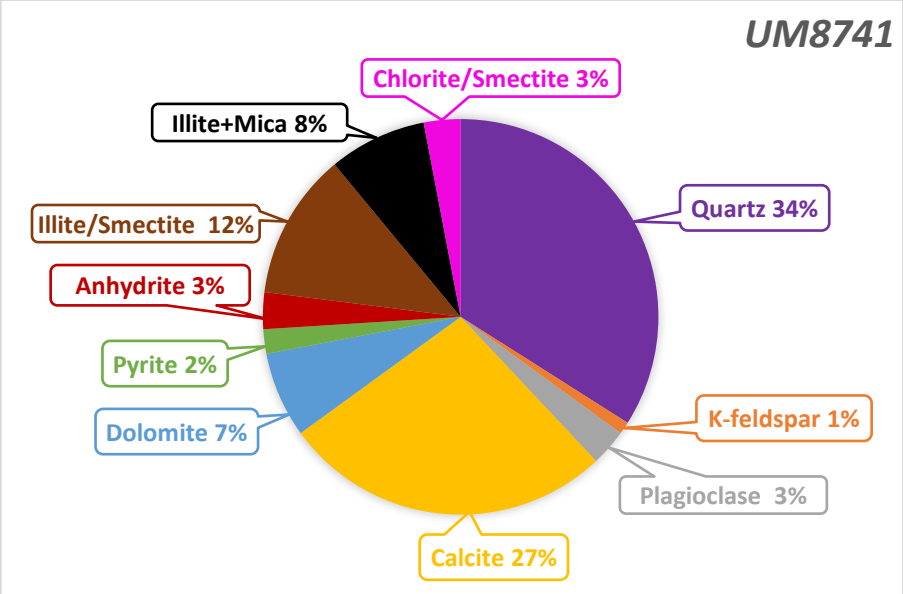


**Figure 4-1**. X-ray diffraction (XRD) results for samples from wells 1-4 Norton Federal (A), 1-4 Kissinger Federal (B), 9-21 Antelope (C), and 44-34 Ute Mountain (D).

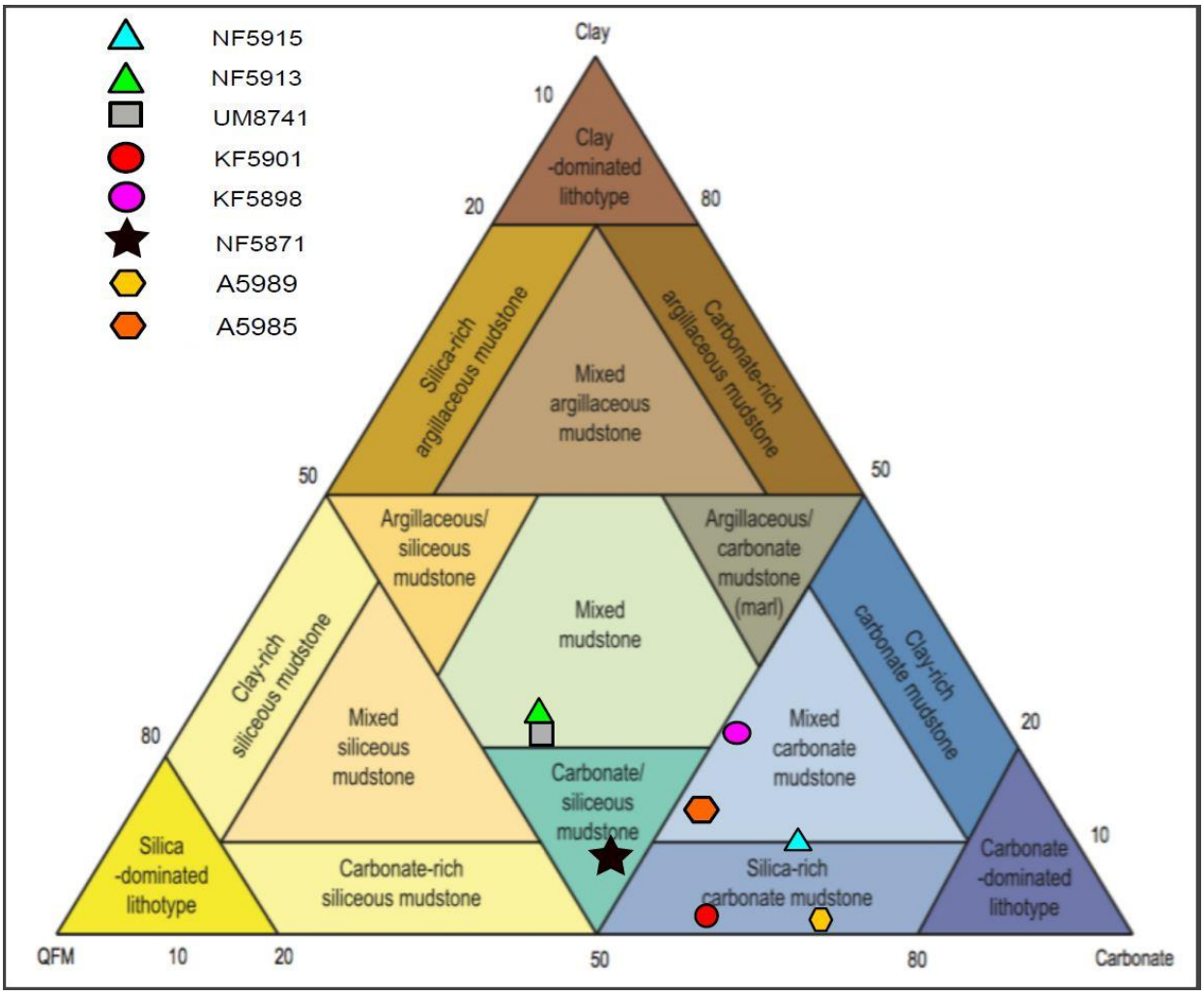


**Figure 4-2**. Core samples plotted on sCore lithofacies classification scheme for organic mudstones (modified from Gamero-Diaz et al., 2013).

**Table 4-1.** Summary of XRD results from Shimadzu and Weatherford Laboratories.

| | Sample Name | | | | | | | |
|---|---|---|---|---|---|---|---|---|
| ***Mineral*** | ***NF5871*** | ***NF5913*** | ***NF5915*** | ***KF5898*** | ***KF5901*** | ***A5985*** | ***A5989*** | ***UM8741*** |
| *Quartz* | 36.4 | 35 | 21.7 | 17.3 | 33.8 | 15.8 | 25.9 | 34 |
| *K-feldspar* | | 1 | | | | | | 1 |
| *Plagioclase* | 2.2 | 1 | | | | | 1 | 3 |
| *Calcite* | 39.8 | 23 | 45 | 36.8 | 43.3 | 17.1 | 14 | 27 |
| *Ankerite* | | | | | | | | <1 |
| *Dolomite* | 7.9 | 10 | 19.2 | 5.5 | 16.3 | 35.2 | 54.9 | 7 |
| *Pyrite* | 5.5 | 3 | 1.5 | 4.2 | 2.1 | 2.6 | 2.6 | 2 |
| *Anhydrite* | | 2 | | 6.7 | | 15.4 | | 3 |
| *Muscovite* | 4.6 | | | | 2.9 | | 1.3 | |
| *Glauconite* | | | | | | | 0.3 | |
| *Siderite* | | | | | | 0.5 | | |
| *Minrecordite* | | | | 4.6 | | | | |
| *Jacobsite* | | | 3.2 | 4.4 | | | | |
| *Illite* | 3.6 | | 9.4 | 20.6 | 1.6 | 13.4 | | |
| *Illite/Smectite* | | 8 | | | | | | 12 |
| *Illite+Mica* | | 14 | | | | | | 8 |
| *Chlorite/Smectite* | | 3 | | | | | | 3 |

*4-2 Geochemistry*

Geochemistry data of all samples are presented in Table 4-2. The percent carbonate of all samples ranges from 42 – 69%, with sample UM8741 having a bit lower percentage of carbonate at 34%. TOC content varies within the dataset, containing values from 0.74 – 2.14. $T_{max}$ values ranged from 445 – 529 ºC and are subsequently used to calculate vitrinite reflectance for some samples. Calculated values of vitrinite reflectance (performed in April of 2017, 40 years after the samples were cored) showed little variance and had a medium value of 0.92; however, measured vitrinite reflectance ranged 1.03 – 1.79 (performed in October of 2010). The calculated vitrinite reflectance values suggest oil was produced and falls at the beginning of the oil generation window, differing from the measured vitrinite reflectance, which suggest gas generation. The maturity log further displays that the measured vitrinite reflectance generates gas, both wet and dry, while

calculated vitrinite reflectance suggest only oil generation (Figure 4-3). Additionally, pyrolysis source potential logs indicate the oil potential is poor to fair (Figure 4-4); has excellent percent carbonate, but only fair to good total organic carbon (Figure 4-5); and that all samples are gas prone (Figure 4-6). More support for gas generation is found in the hydrocarbon indicator log, via the production index ($S_1/(S_1+S_2)$) (Figure 4-7). The kerogen types for all samples were determined using the pseudo van Krevelen plot and are displayed in Figure 4-8.

**Table 4-2.** Geochemical analyses for all samples (data from Weatherford Laboratories are in black; data from Geomark Research highlighted red).

| Sample ID | Percent Carbonate (wt%) | Leco TOC (wt%) | S1 (mg HC/g) | S2 (mg HC/g) | S3 (mg CO2/g) | Tmax (°C) | Measured %Ro (Vitrinite Refl.) | Calculated %Ro (RE TMAX) | Hydrogen Index (S2x100/TOC) | Oxygen Index (S3x100/TOC) | S2/S3 Conc. (mg HC/mg CO2) | S1/TOC Norm. Oil Content | Production Index (S1/(S1+S2) | Experimental Notations |
|---|---|---|---|---|---|---|---|---|---|---|---|---|---|---|
| NF5871 | 47.70 | 1.36 | 0.38 | 0.32 | 0.46 | 529 | 1.79 | | 24 | 34 | 1 | 28 | 0.54 | |
| NF5873 | 43.11 | 0.74 | 0.22 | 0.11 | 0.25 | | | | 15 | 34 | 0 | 30 | 0.67 | S2 to low to measure |
| KF5898 | 52.79 | 0.98 | 0.52 | 0.23 | 0.21 | 447 | | 0.89 | 23 | 21 | 1 | 53 | 0.69 | |
| KF5901 | 59.60 | 1.56 | 0.72 | 0.44 | 0.54 | 489 | 1.40 | | 28 | 35 | 1 | 46 | 0.62 | |
| NF5913 | 42.14 | 1.12 | 0.68 | 0.39 | 0.32 | 449 | | 0.92 | 35 | 29 | 1 | 61 | 0.64 | |
| NF5915 | 64.20 | 1.41 | 0.74 | 0.59 | 0.56 | 449 | | 0.92 | 42 | 40 | 1 | 52 | 0.56 | |
| A5985 | 50.62 | 2.14 | 1.37 | 3.53 | 0.36 | 449 | | 0.92 | 165 | 17 | 10 | 64 | 0.28 | Low Temp S2 Shoulder |
| A5989 | 68.90 | 2.05 | 1.49 | 3.26 | 0.60 | 445 | 1.17 | | 159 | 29 | 5 | 73 | 0.31 | |
| UM8741 | 34.00 | 1.21 | 0.25 | 0.18 | 0.09 | 455 | 1.03 | | 15 | 7 | 2 | 21 | 0.58 | |

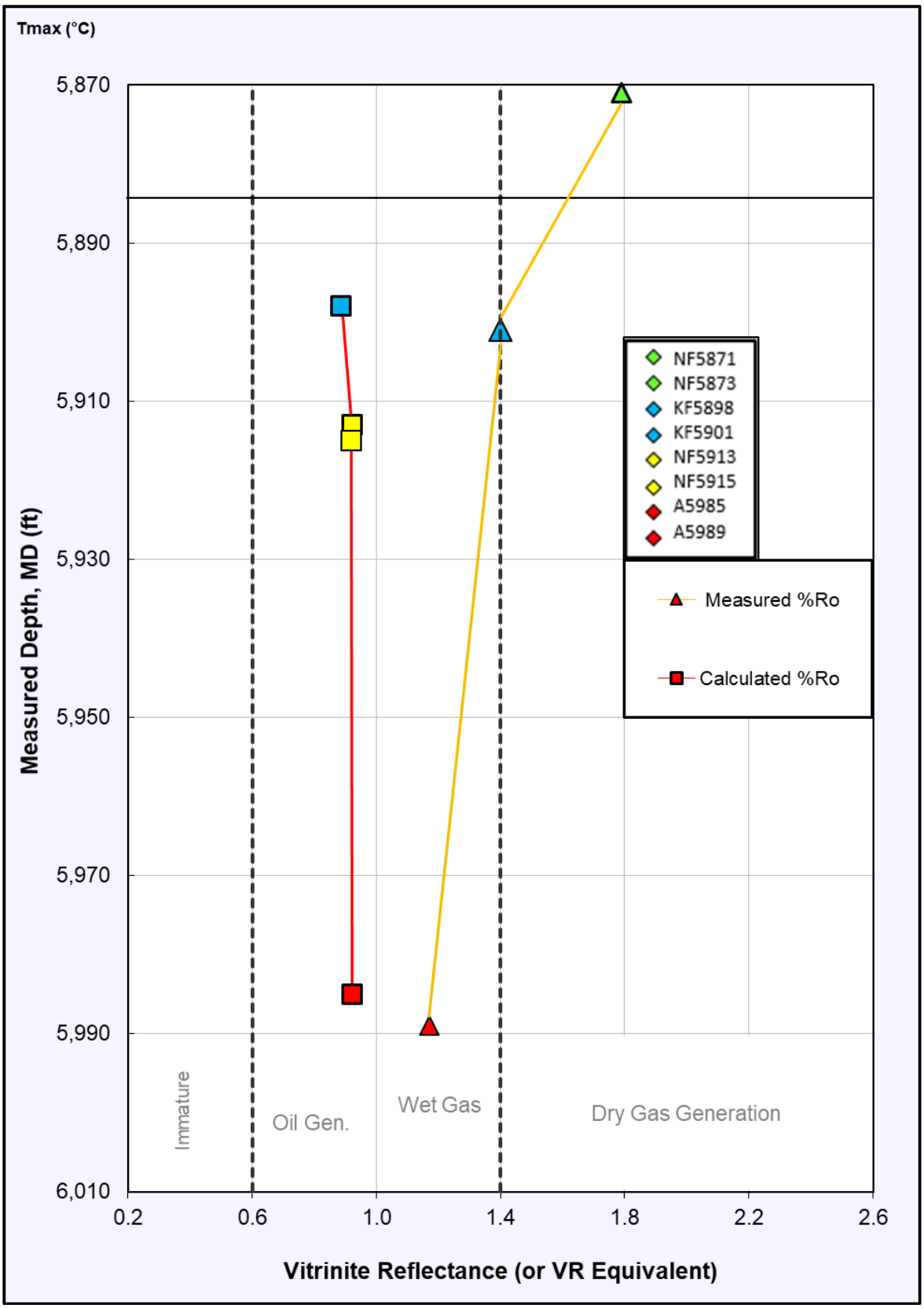


**Figure 4-3.** Maturity log of vitrinite reflectance vs. measure depth (feet).

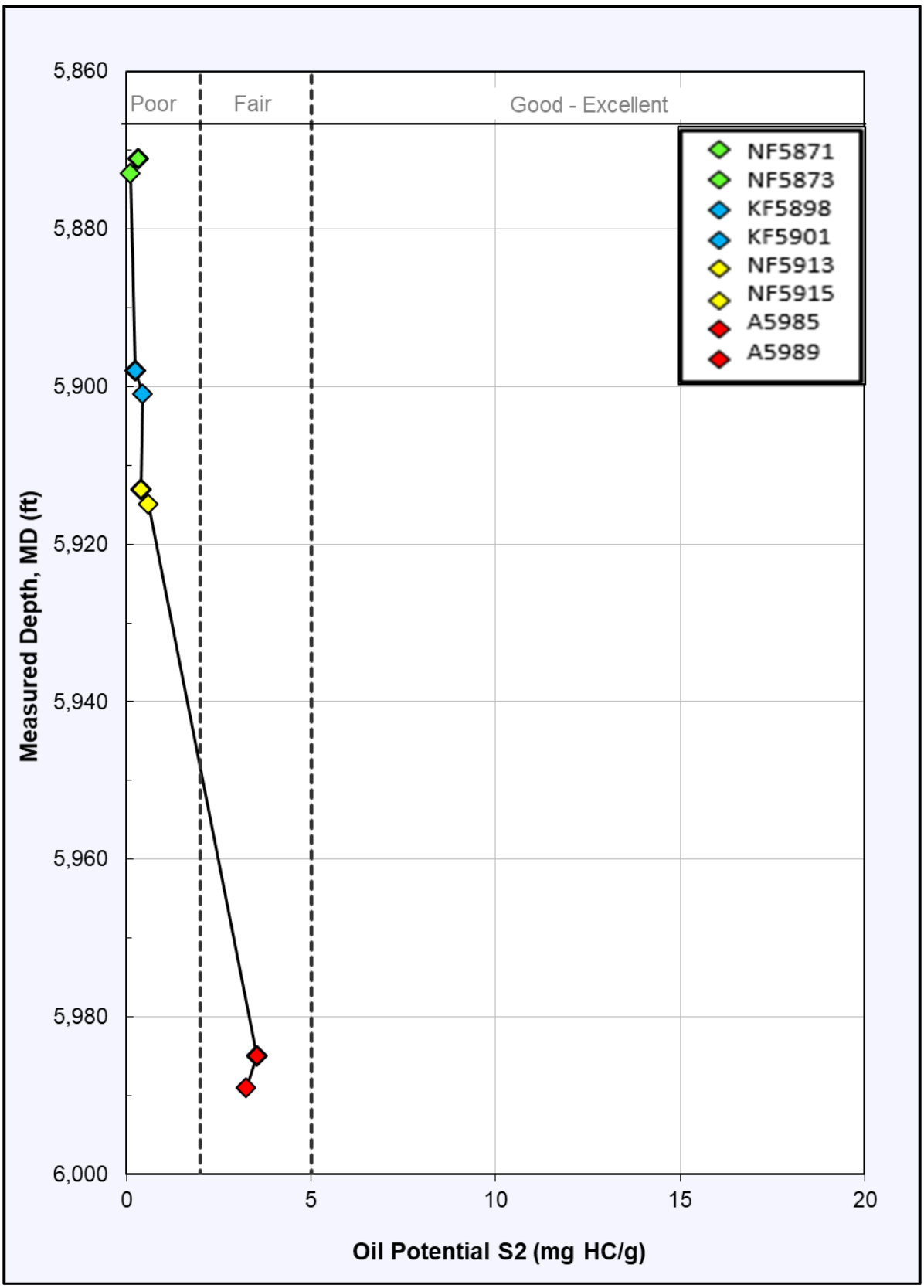


**Figure 4-4.** Pyrolysis source potential log displaying oil potential.

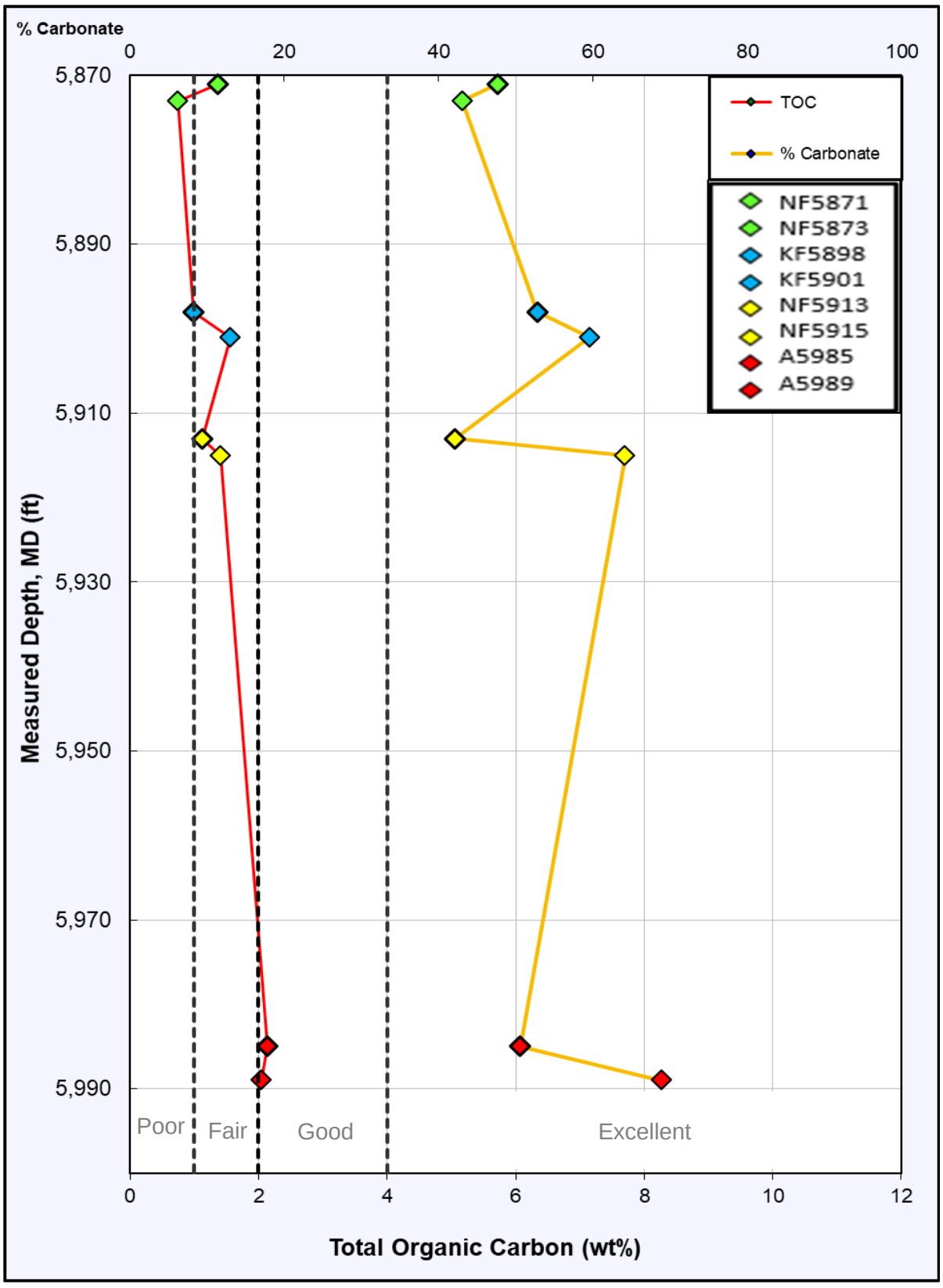


**Figure 4-5.** Pyrolysis source potential log of TOC vs. measured depth (feet).

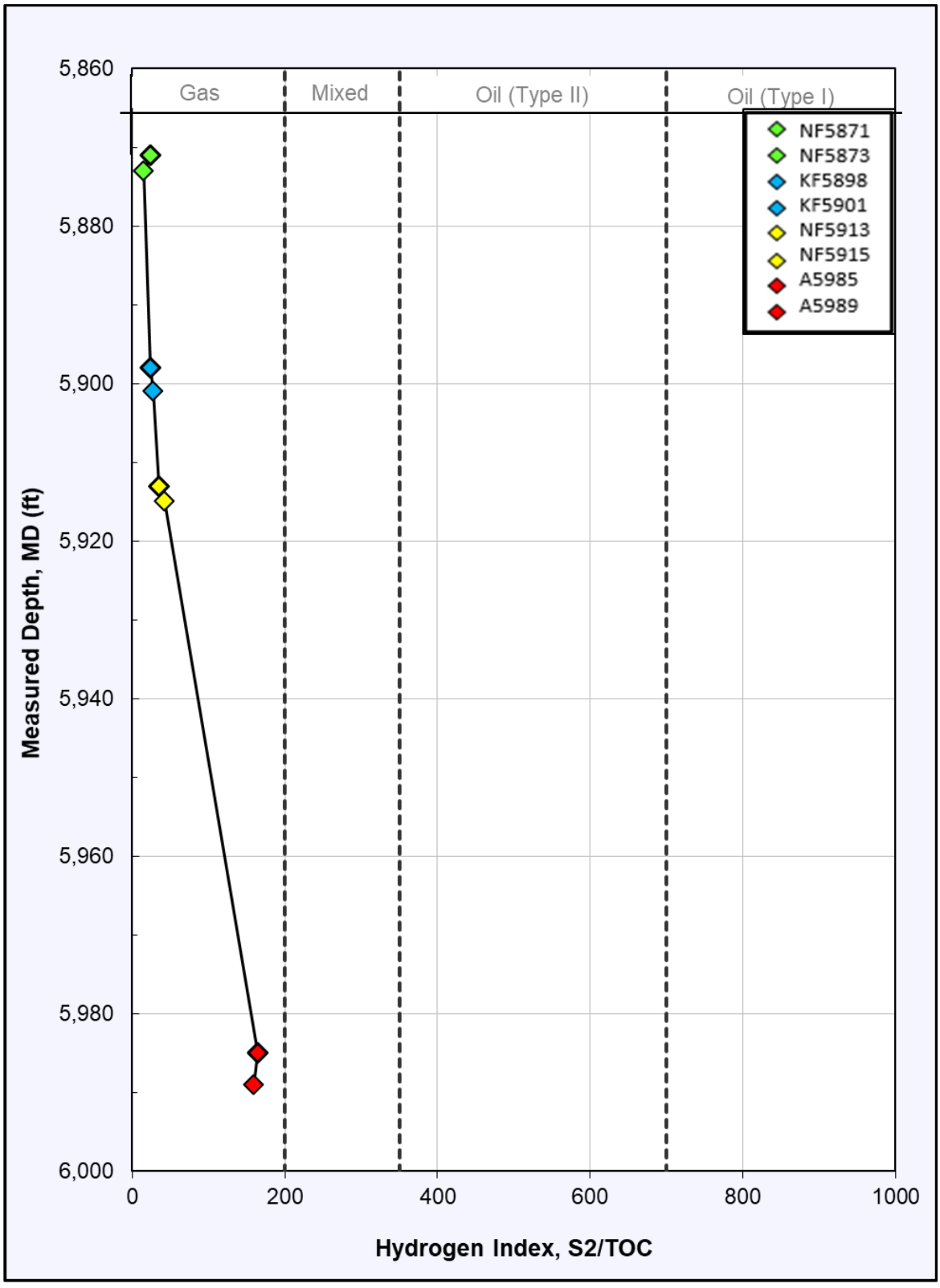


**Figure 4-6.** Pyrolysis source potential log of HI vs. measured depth (feet).

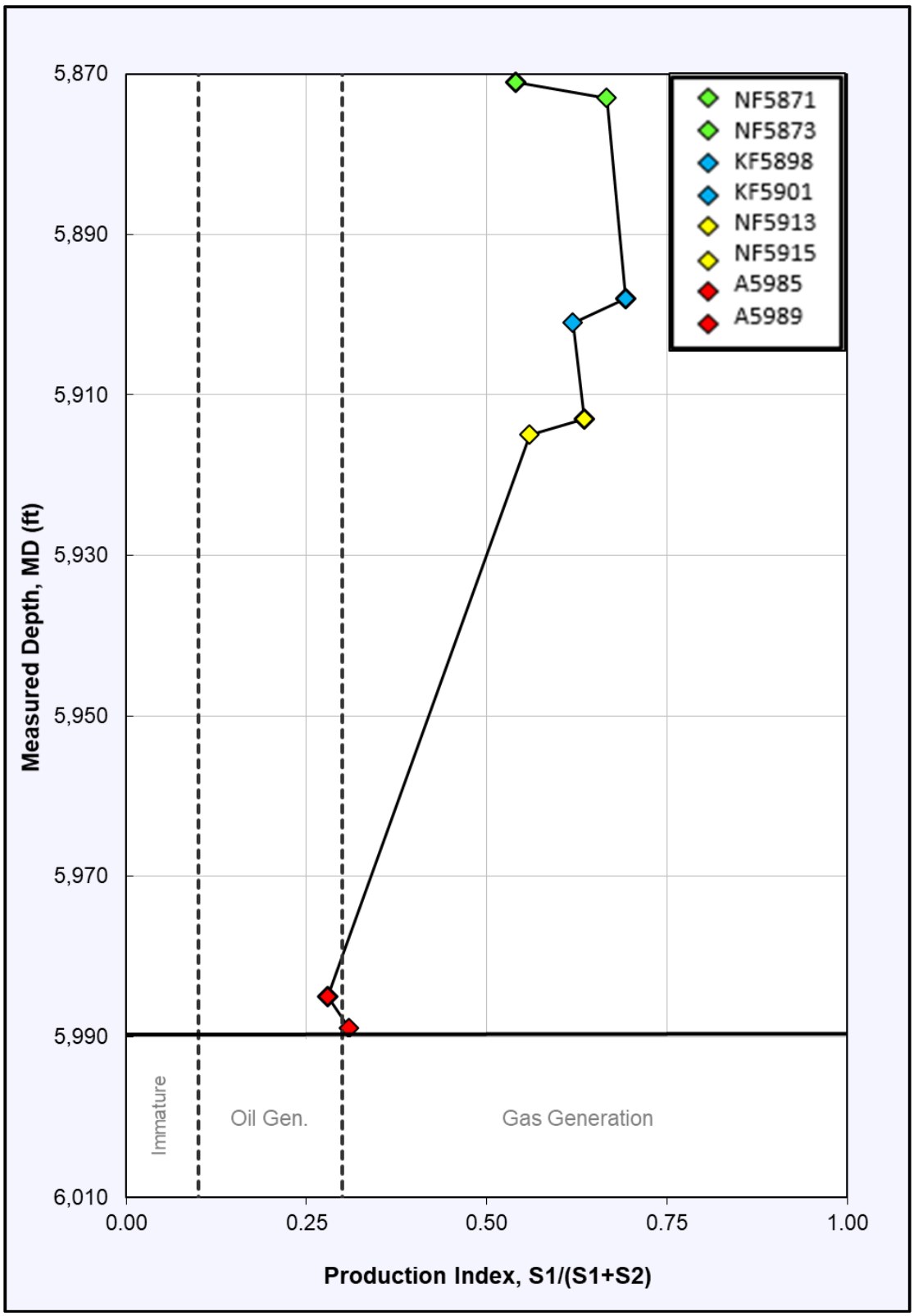


**Figure 4-7.** Hydrocarbon indicator log.

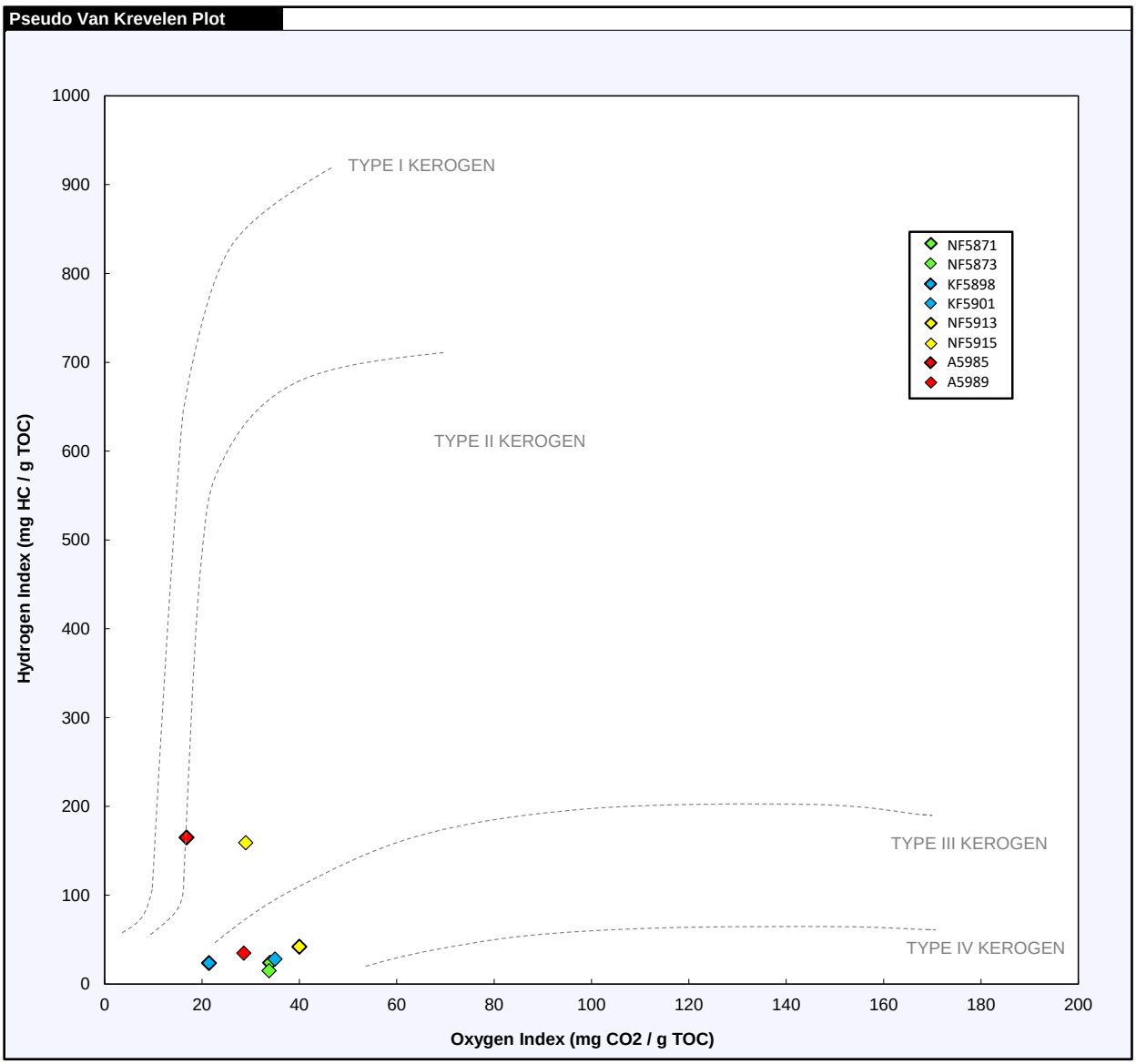


**Figure 4-8.** Kerogen type for samples**.**

*4-3 Mercury Intrusion Capillary Pressure (MICP)*

MICP tests produce direct data that can be processed to obtain various petrophysical properties for each sample. To obtain the secondary data, such as permeability and tortuosity, methods detailed by Gao and Hu (2013) were followed to characterize pore structure. All the acquired core samples were analyzed using MICP and their results are shown in Table 4-3.

**Table 4-3.** Pore structure characteristics obtained from MICP tests.

| Sample ID | Bulk Density (g/cm3) | Porosity % | Permeability (mD) | Median pore-throat diameter $D_{50}$ (Volume) (µm) | Median pore-throat diameter (Area) (µm) |
|---|---|---|---|---|---|
| A5985 | 2.632 | 0.543 | 0.5778 | 1980 | 81.0 |
| A5989 | 2.619 | 0.654 | 1.3775 | 42.6 | 14.2 |
| NF5871 | 2.537 | 0.951 | 0.2524 | 7.0 | 4.10 |
| NF5873 | 2.647 | 0.611 | 0.2895 | 114 | 24.2 |
| NF5913 | 2.638 | 0.384 | 0.4828 | 13.6 | 4.00 |
| NF5915 | 2.658 | 0.224 | 0.4769 | 1823 | 54.7 |
| KF5898 | 2.626 | 0.821 | 0.3481 | 11.1 | 4.10 |
| KF5901 | 2.616 | 0.422 | 0.4503 | 49.1 | 4.20 |
| UM8741 | 2.597 | 0.729 | 0.6099 | 11.1 | 3.20 |

Many of the samples have porosity that falls within the range 0.5-1.0%. The dataset had an average porosity of 0.593% with the lowest porosity (0.224%) found in the NF5915 sample, and the highest (0.951%) in sample NF5871. Furthermore, the bulk density is relatively consistent among all the samples with a minimum value of 2.596 g/cm$^3$ and a maximum value of 2.658 g/cm$^3$, found in UM8741 and NF5915, respectively.

An inflection point, which signifies that the mercury intrusion into the sample has entered into a specific pore throat system, was chosen according to Gao and Hu (2013). Using the chosen inflection points and the modified Washburn equation allow for the determination of the pore-throat size distribution for connected pore network from μm to nm ranges. An example of inflection points can be seen in Figure 4-9 and are identified for each sample run. In addition, the permeability and tortuosity values for an inflection point associated with the most abundant pore-throat system are present in Table 4-4. Permeability values reach 1.378 mD for sample A5989; however, this is an exception. The average value of the dataset was 0.541 mD with a minimum of 0.252 mD. For tortuosity, values range greatly from 7.762 in the NF5915 sample to 6521 in the UM8741 sample.

**Table 4-4.** Permeability and tortuosity values associated with the most abundant pore-throat system.

| Sample ID | Most Abundent Pore Type | Matrix Tortuosity (Do/De) | Permeability (md) |
|---|---|---|---|
| NF5871 | Organic Pores | 1546.406 | 1.14E-06 |
| NF5873 | Intragranular Pores | 483.488 | 3.86E-05 |
| KF5898 | Inter-clay platelet pore spaces | 2951.250 | 7.37E-07 |
| KF5901 | Microfractures | 12.274 | 2.92E-02 |
| NF5913 | Inter-clay platelet pore spaces | 4191.178 | 2.48E-07 |
| NF5915 | Microfractures | 7.762 | 1.01E-01 |
| A5985 | Microfractures | 11.828 | 5.92E-02 |
| A5989 | Intragranular Pores | 523.167 | 3.22E-05 |
| UM8741 | Inter-clay platelet pore spaces | 6521.345 | 2.70E-07 |

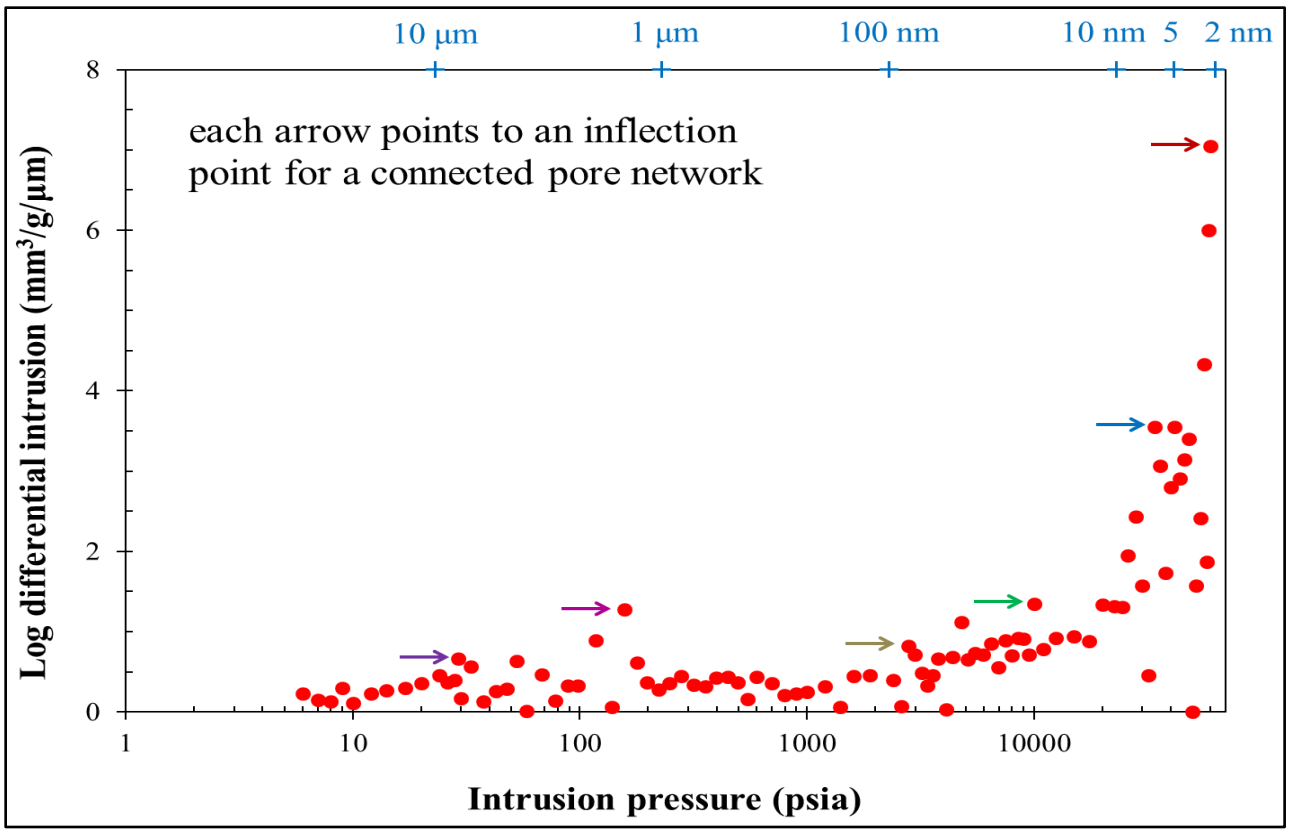


**Figure 4-9.** Illustration showing inflection points (arrows) of MICP results in KF5898 sample.

Pore throat diameters are broadly affiliated with different pore types (Hu et al., 2017), such as: (a) 50 – 1 micrometer equates to micro-fractures in the rock; (b) 0.5 – 1 micrometer equates to intergranular pore space; (c) 50 – 10 nm are intragranular pore space; (d) 10 – 5 nm sized pores are organic pores; and (e) 5 – 2.8 nm sized pores are inter-clay platelet pore spaces. Most of the samples have pore types that are dominated by either micro-fractures, particularly 1-10 micrometer sized pores, or inter-clay platelet pores (5-2.8 nm sized pores) (Table 4-5). The other samples, A5989, NF5873, and NF5871, were dominated by intraganular and organic pore types, respectively. Sample pore-throat size distributions were wide-ranging and can be viewed in Figure 4-10.

**Table 4-5.** Histograms of pore-throat diameters (%) from MICP analysis.

| SAMPLE ID | 0.0028-0.005 µm (%) | 0.005-0.01 µm (%) | 0.01-0.05 µm (%) | 0.05-0.1 µm (%) | 0.1-1 µm (%) | 1-10 µm (%) | 10-50 µm (%) |
|---|---|---|---|---|---|---|---|
| ***NF5871*** | 26.0 | 28.6 | 18.6 | 5.973 | 10.783 | 7.439 | 2.593 |
| ***NF5873*** | - | - | 38.561 | 10.981 | 9.964 | 33.530 | 6.964 |
| ***KF5898*** | 23.1 | 21.084 | 20.477 | 5.317 | 10.618 | 13.652 | 5.710 |
| ***KF5901*** | 17.9 | 15.838 | 12.513 | 8.178 | 18.023 | 20.505 | 7.031 |
| ***NF5913*** | 22.4 | 18.601 | 20.954 | 8.491 | 16.082 | 5.121 | 8.342 |
| ***NF5915*** | - | - | 3.230 | 7.534 | 25.811 | 46.082 | 17.343 |
| ***A5985*** | - | - | 9.522 | - | 15.899 | 68.521 | 6.058 |
| ***A5989*** | - | 0.802 | 41.524 | 39.715 | - | 10.336 | 7.623 |
| ***UM8741*** | 28.4 | 13.360 | 17.157 | 6.577 | 11.774 | 13.397 | 9.347 |

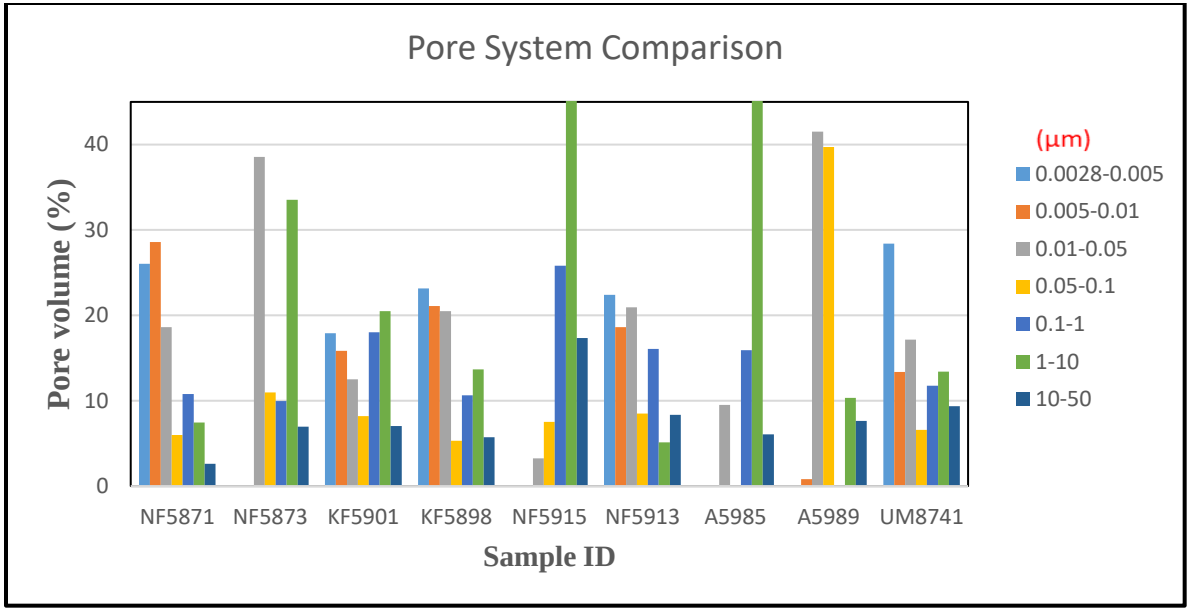


**Figure 4-10.** Graphic comparison of pore-throat size distribution from MICP results.

*4-4 Helium Porosity and Permeability of Core Plugs*

Table 4-6 displays the results from helium porosity alongside the porosity obtained via MICP. Due to the sample size required to run this experiment (e.g. core plugs) only one sample per well was chosen. When compared to MICP results, the porosity values for all plug samples were larger, probably due to the lamionations/micro-fractures present at core scale, but not at cube scale. All samples were found to have low porosity. Using helium to test porosity, sample UM8741 increased by more than 100% when compared to MICP porosity. Sample UM8741 had the highest porosity of 1.763, and sample A5985 had the lowest porosity of 0.814.

**Table 4-6.** Porosity Comparison using two different methods.

| Sample ID | Helium | | MICP | |
|---|---|---|---|---|
| | Sample Dimensions (cm-plug) | Porosity (%) | Sample Dimensions (cm) | Porosity (%) |
| KF5898 | 2.50 D x 6.1 H | 0.941 | 1-cm cube | 0.8208 |
| A5985 | 2.36 D x 7.9 H | 0.814 | 1-cm cube | 0.5429 |
| NF5915 | 2.41 D x 3.9 H | 0.961 | 1-cm cube | 0.224 |
| UM8741 | 2.42 D x 3.7 H | 1.763 | 1-cm cube | 0.7285 |

Permeability values for samples showed a wide range (Table 4-7). Samples A5985 and KF5898 show good permeability with Klinkenberg corrected permeability values of 2.94E+07 nD and 1.06E+06 nD. Samples NF5915 and UM8741have a Klinkenberg corrected permability value of 2.02E+03 nD.

**Table 4-7.** Permeability comparison using helium expansion and MICP methods

| Sample ID | Helium | | MICP | | |
|---|---|---|---|---|---|
| | Sample Dimensions (cm-plug) | k Klinkenberg (nD) | Sample Dimensions (cm) | Permeability | |
| | | | | Geometric (nD) | Harmonic (nD) |
| KF5898 | 2.50 D x 6.1 H | 1.06E+06 | 1-cm cube | 2.31E+01 | 1.81 |
| A5985 | 2.36 D x 7.9 H | 2.94E+07 | 1-cm cube | 4.99E+03 | 4.84 |
| NF5915 | 2.41 D x 3.9 H | 2.02E+03 | 1-cm cube | 4.04E+04 | 1.87E+03 |
| UM8741 | 2.42 D x 3.7 H | 5.15E+05 | 1-cm cube | 7.86E+01 | 0.93 |

*4-5 Contact Angle for Wettability*

Due to sample size limitations, the wettability of one sample with relative depth was taken. All these samples were tested using API brine and 10% IPA in DI water. API brine, composed of 8% NaCl and 2% $CaCl_2$, is water wetting and was utilized due to its' high salinity, similar to formation water (Wendell, 1969). IPA is a zwittering fluid, which is both hydrophilic and hydrophobic. Sample results show both API brine and 10% IPA are good wetting fluids, with samples generally displaying better wettability to 10% IPA.

**Table 4-8.** Contact angle (degrees) for each fluid-sample pair.

| Sample ID | API Brine | 10% IPA |
|---|---|---|
| NF5873 | 30.63 | 16.4 |
| KF5898 | 31.16 | 29.22 |
| NF5913 | 51.34 | 29.91 |
| A5985 | 48.80 | 29.46 |
| UM8741 | 28.64 | 33.48 |

*4-6 Fluid Imbibition*

As previously mentioned, both water and n-decane were used on all samples for fluid imbibition tests. When performing water imbibition testing, surface tension causes a pull-down effect, leading to an "apparent" weight gain, due to its modestly weak wettability. This increases the error and as of now, cannot be accounted for, only minimized, via multiple runs. While causing the "apparent" weight to be larger than the check weight, however, this effect seems to not affect the imbibition slope.

During imbibition, three slopes, each representing a different stage, can typically be identified (Figure 4-11). The first slope (Stage I) lasts up to 5 minutes and represents the initial contact phase between the sample and fluid. The second slope (Stage II) generally last up to 15-45 minutes. This phase is attributed to the fluid migration onto the samples surface. The third slope (Stage III, termed as connectivity slope) best represents the pore connectivity of the rock matrix and generally last for the remainder of the experiment. Occasionally, as seen in KF5901, n-decane imbibition runs a fourth slope (Stage IV) as displayed in Figure 4-12. If found, this slope ranges from ~0 – 0.1 and represents fluid reaching the top of the sample (Hu et al, 2001).

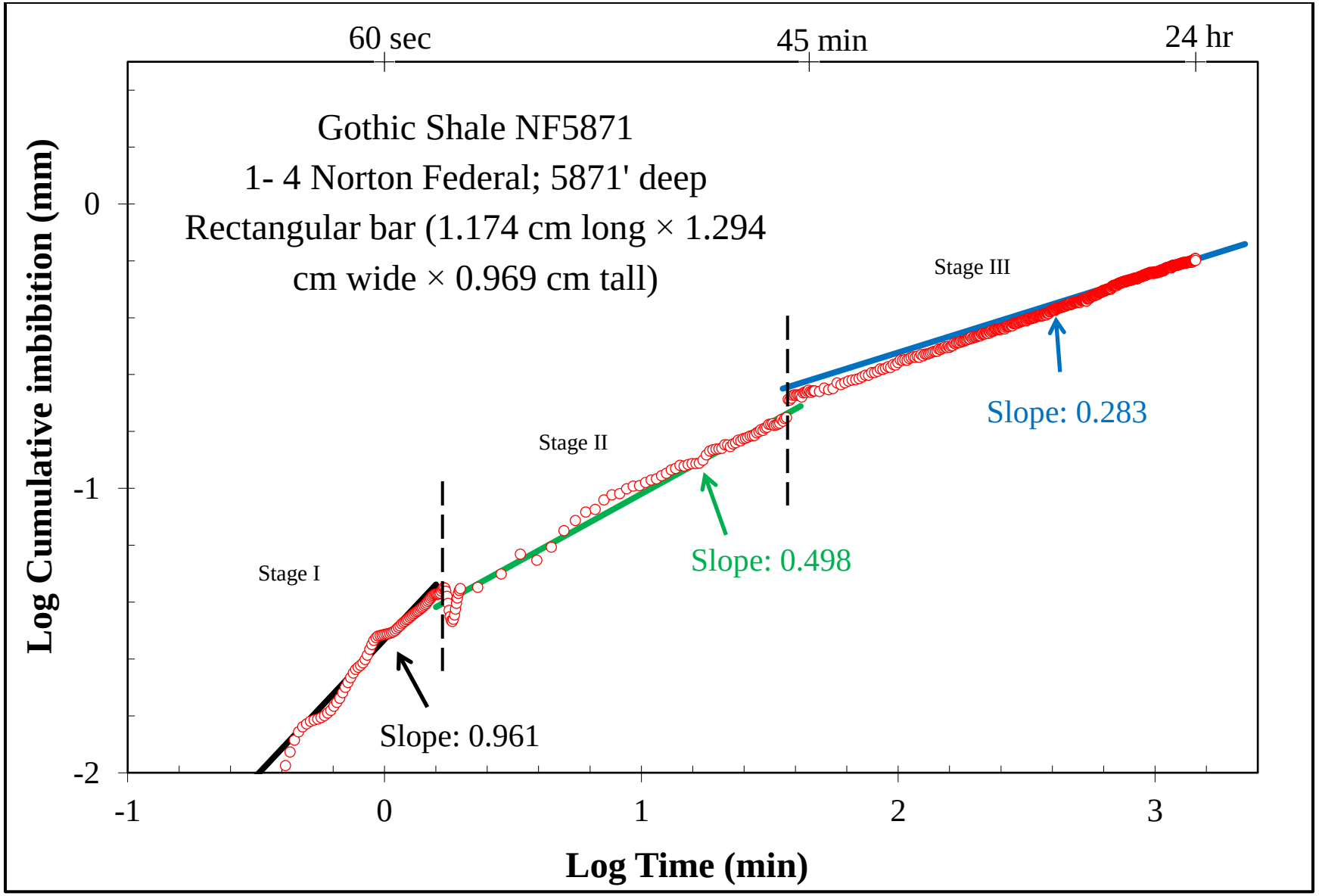


**Figure 4-11.** DI water imbibition for NF5871 sample; displaying the typical three slopes.

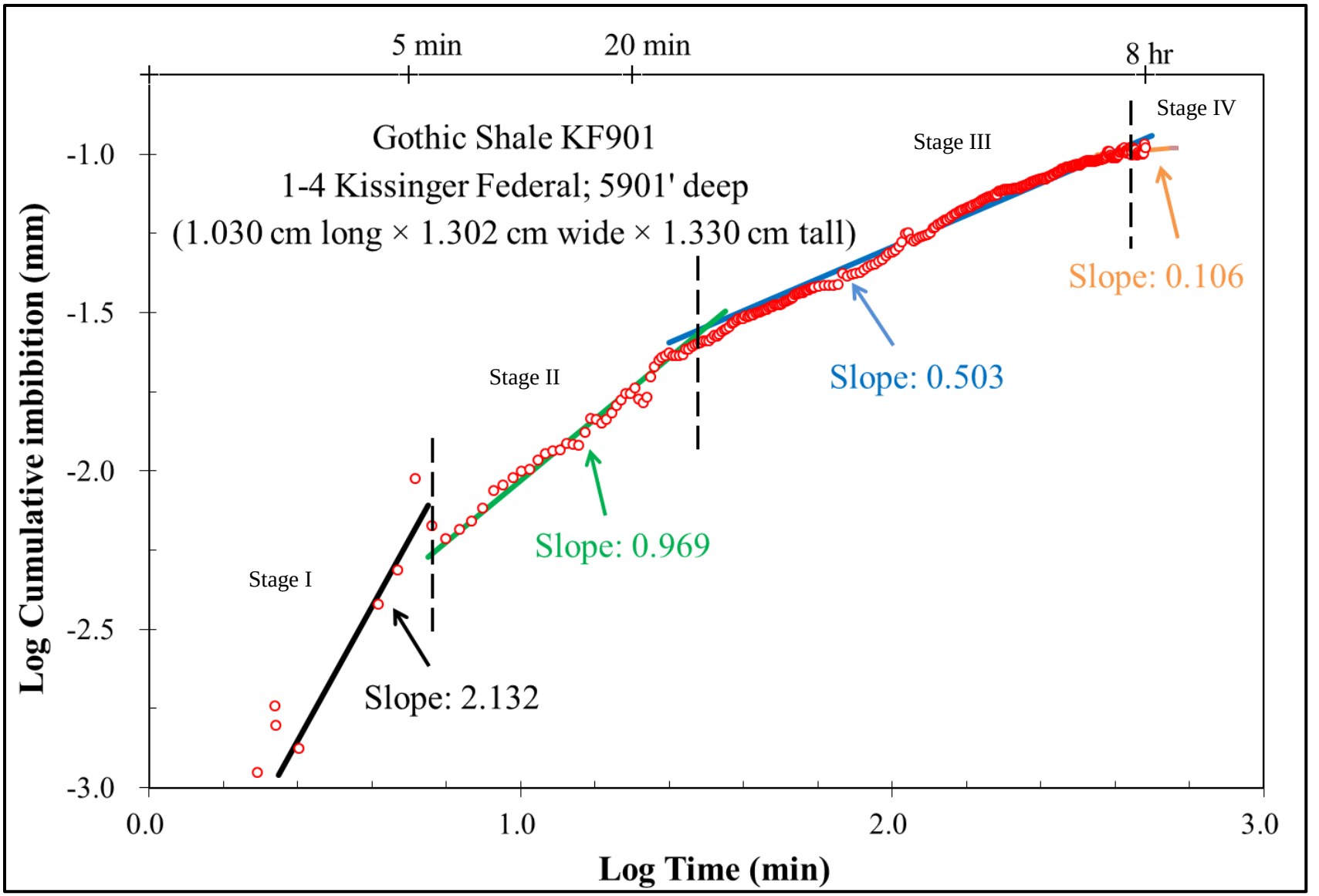


**Figure 4-12.** Example of n-decane imbibition into sample KF5901 with all four stages of imbibition.

Table 4-9 shows the calculated slopes for all imbibition runs. Lower stage III slopes (~ 0.25) indicate poor connectivity, while higher slopes (~ 0.5) show a well-connected pore network for the imbibing fluid. For most samples, n-decane imbibition showed higher slopes, indicating that the pore system has a better connection to oil wetting fluids; the only exceptions being KF5898 and A5989 (the most-right column of Table 4-9 being highlighted in red for connectivity slopes).

The overall results suggest that there is low pore connectivity with respect to water in the samples, however sample NF5915 showed that its pore system has a good connection to oil wetting and water wetting fluids.

**Table 4-9.** Calculated slopes for imbibition tests.

| Sample ID | Fluid | Stage I Slope | Stage II Slope | Stage III Slope |
|---|---|---|---|---|
| ***NF5871*** | DI water | 0.961 | 0.498 | 0.283 |
| | n-decane | 0.692 | — | 0.435 |
| ***NF5873*** | DI water | 3.694 | 0.621 | 0.222 |
| | n-decane | 3.923 | 2.062 | 0.502 |
| ***KF5898*** | DI water | 0.758 | 0.630 | 0.276 |
| | n-decane | 0.031 | 0.043 | 0.259 |
| ***KF5901*** | DI water | 0.693 | — | 0.277 |
| | n-decane | 2.132 | 0.969 | 0.503 |
| ***NF5913*** | DI water | 1.150 | 0.581 | 0.246 |
| | n-decane | — | 1.662 | 0.458 |
| ***NF5915*** | DI water | 0.836 | — | 0.532 |
| | n-decane | — | 2.097 | 0.594 |
| ***A5985*** | DI water | — | 0.185 | 0.223 |
| | n-decane | — | 0.257 | 0.350 |
| ***A5989*** | DI water | — | 0.450 | 0.384 |
| | n-decane | — | 1.007 | 0.249 |
| ***UM8741*** | DI water | 0.819 | 0.621 | 0.190 |
| | n-decane | 2.177 | 1.055 | 0.575 |

*4-7 Production Data*

For all four wells data was scarce and did not contain any well logs (Table 4-10). Well completion for these wells occurred in the late 1970's to early 1980's. Three out of the four wells targeted the Ismay-Desert Creek formation (Figure 2-4), but without more analytical data the interval targeted within the formation cannot be determined. 1-4 Norton Federal has a "well 2" possibly indicating horizontal drilling but information obtaining to it is either locked or unknown.

**Table 4-10.** Well information gathered from DrillingInfo.

| Wells | 1-4 Kissinger Federal | 1-4 Norton Federal | 44-34 Ute Mountain | 9-21 Antelope |
|---|---|---|---|---|
| Target Formation | Ismay | Desert Creek | Mississippian | Ismay |
| Completion Date | 4/1/1977 | 12/1/1979 | 1/5/1977 | 9/19/1984 |
| Well Status | Inactive (dry hole) | Inactive (dry hole) | Inactive (dry hole) | Inactive (dry hole) |

# Chapter 5 – Discussion

## *5-1 Maturity*

Common pore types, such as mineral associated or organic matter pores, could not be attributed to different maturity levels. Four samples were in the "peak maturity" range with a $R_o$ value of 0.9, which corresponds to the late oil window (Peters and Cassa 1994). The pore systems of these samples varied significantly (Figure 5-1). Two samples are also associated with the late maturity range ($R_o$ ~1.1) and overmature ($R_o$ >1.35) range, falling in the wet gas and dry gas window, respectively. Again, samples within the wet gas range also show a great variety in their pore systems. Lohr et al. (2015) observed pore clogging by migrated bitumen in this maturation level. Maturity, along with other factors such as mineralogy (e.g., carbonate content, clay contents and types), affect pore evolution.

One sample had a majority of micro-fracture pores while the other sample contains a mostly intragranular pore system (Figure 5-2). Samples in the dry gas window are relatively similar as both contain a wide range of pore systems and has a majority of nanopores (inter-clay platelet and organic pores) (Figure 5-3). Figure 5-4 encompasses all the samples for a quality comparison.

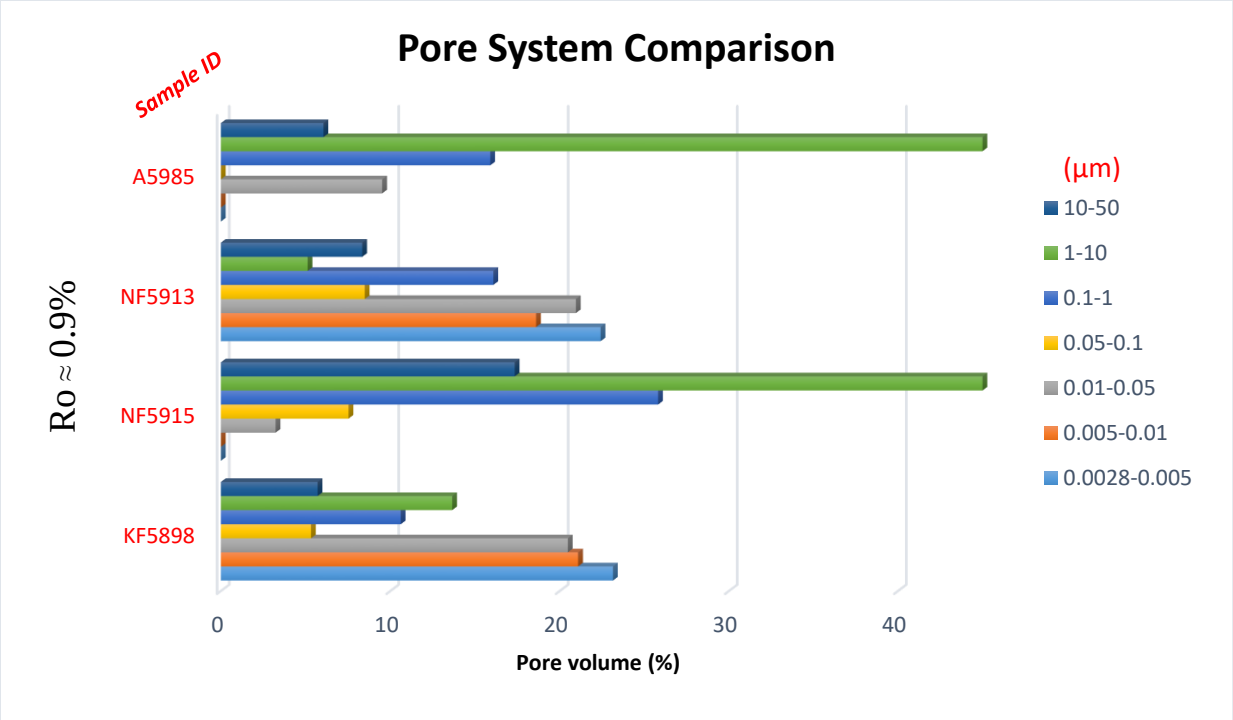


**Figure 5-1.** Relative percentage of pore-throat size intervals of samples with a $R_o \approx 0.9$.

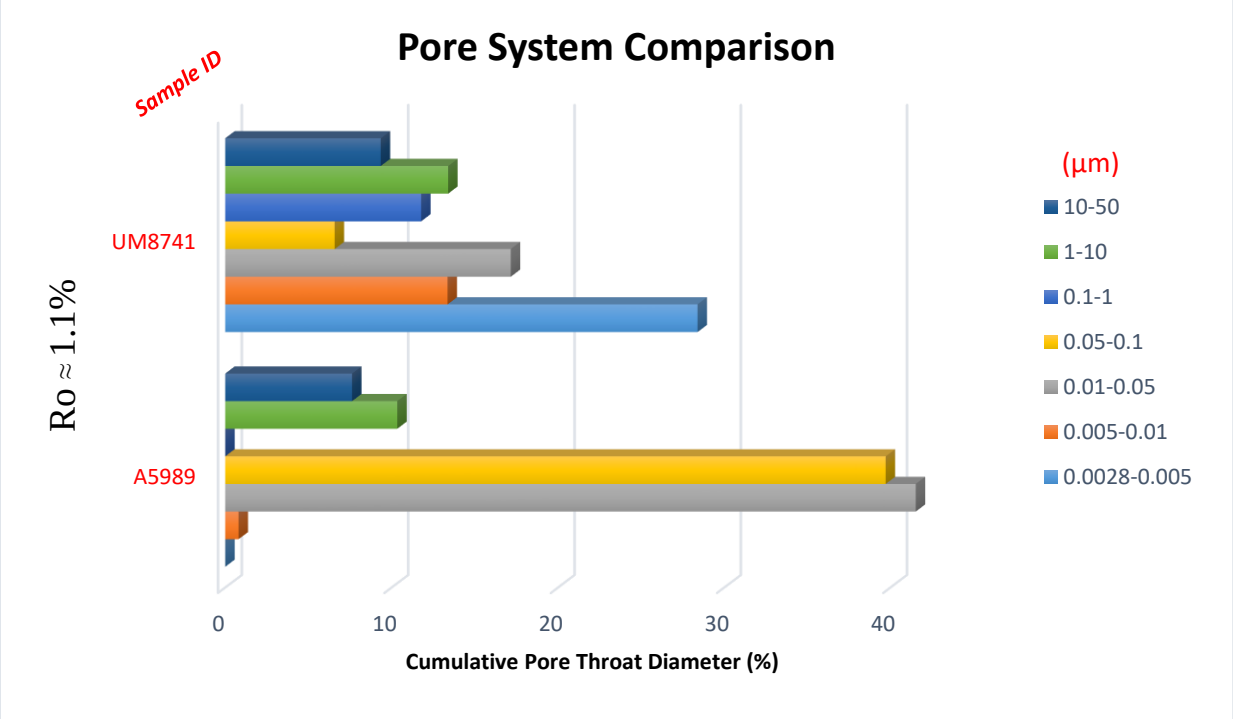


**Figure 5-2.** Pore throat percentages of samples with a $R_o \approx 1.1$.

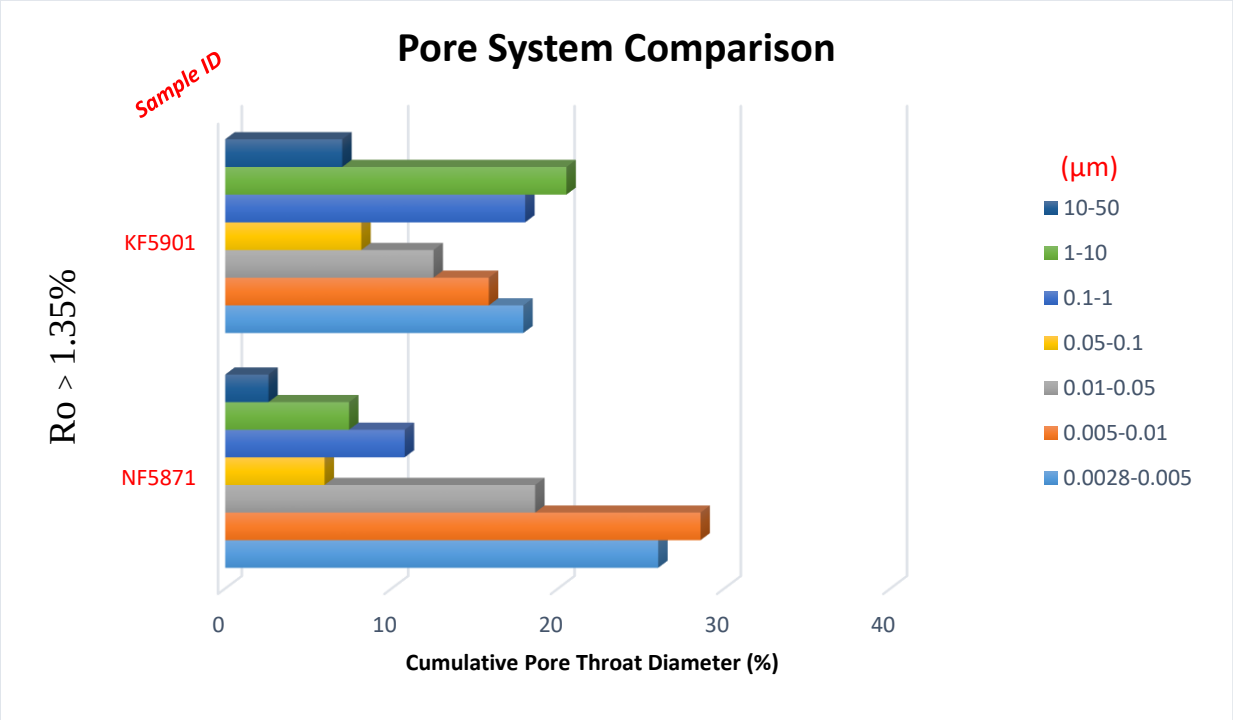


**Figure 5-3.** Pore throat percentages of samples with a $R_o > 1.35$.

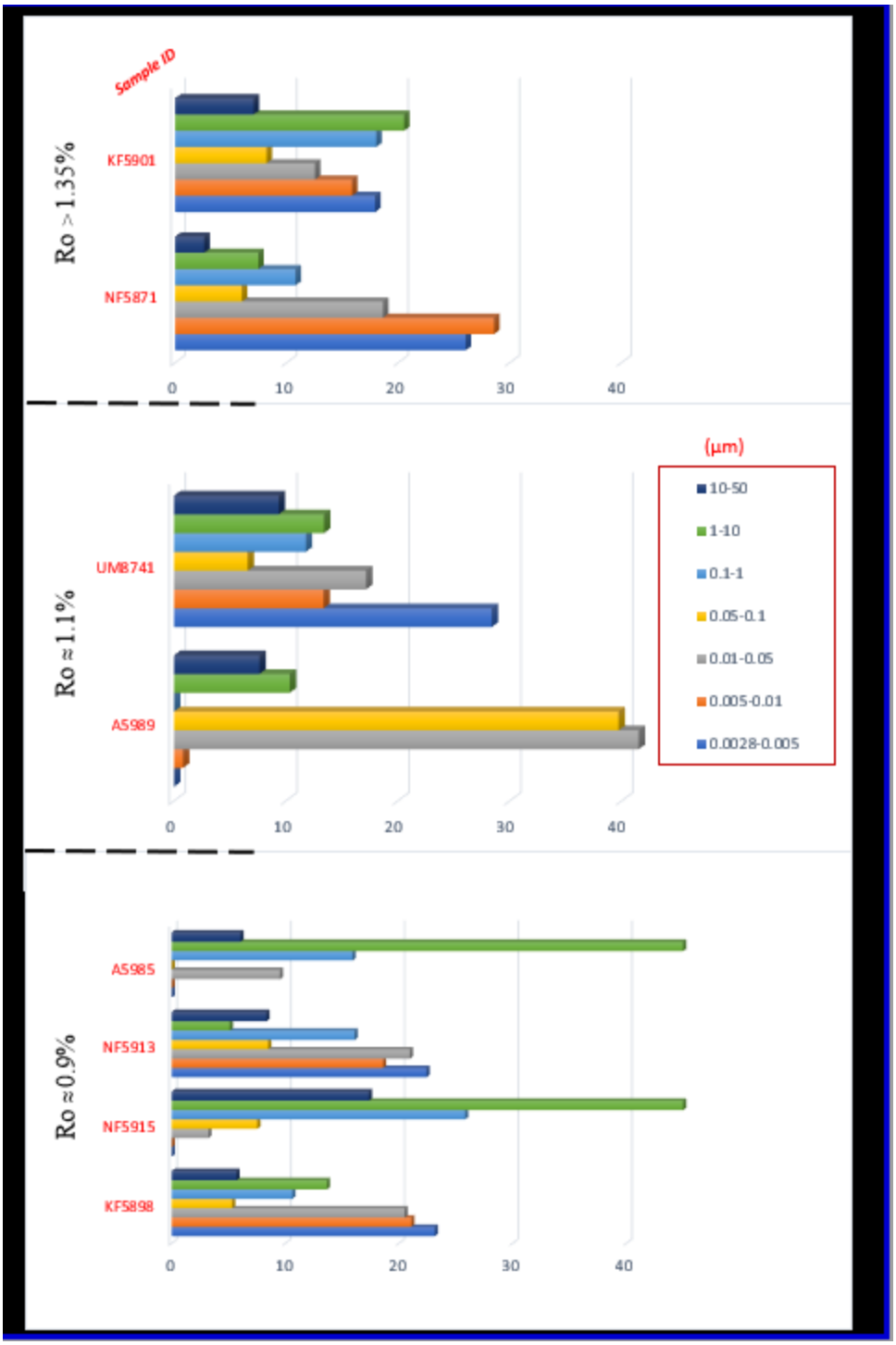


**Figure 5-4.** Comparison of sample maturity's and pore-throat size distributions.

*5-2 Mineralogy*

Pyrolysis results, along with X-ray diffraction, conclude that most samples are dominated by carbonate minerals. Comparing mineralogy, specifically the carbonate percentage, with pore-throat size distribution, no correlation could be identified (Figure 5-5). Furthermore, clay content does not appear to have any significant effect on the pore-throat size or porosity. This is in contrast with the findings of Niobrara shale documented in Villagas (2016) where it advocates a lower illite percentage may reduce intra- and inter-pore spaces and plays a key role in lowering porosity (Figure 5-6). Suggesting that the findings are formation specific as Bevers (2017) also finds no correlation between mineralogy (quartz, carbonate, or clay) and porosity in its shale samples.

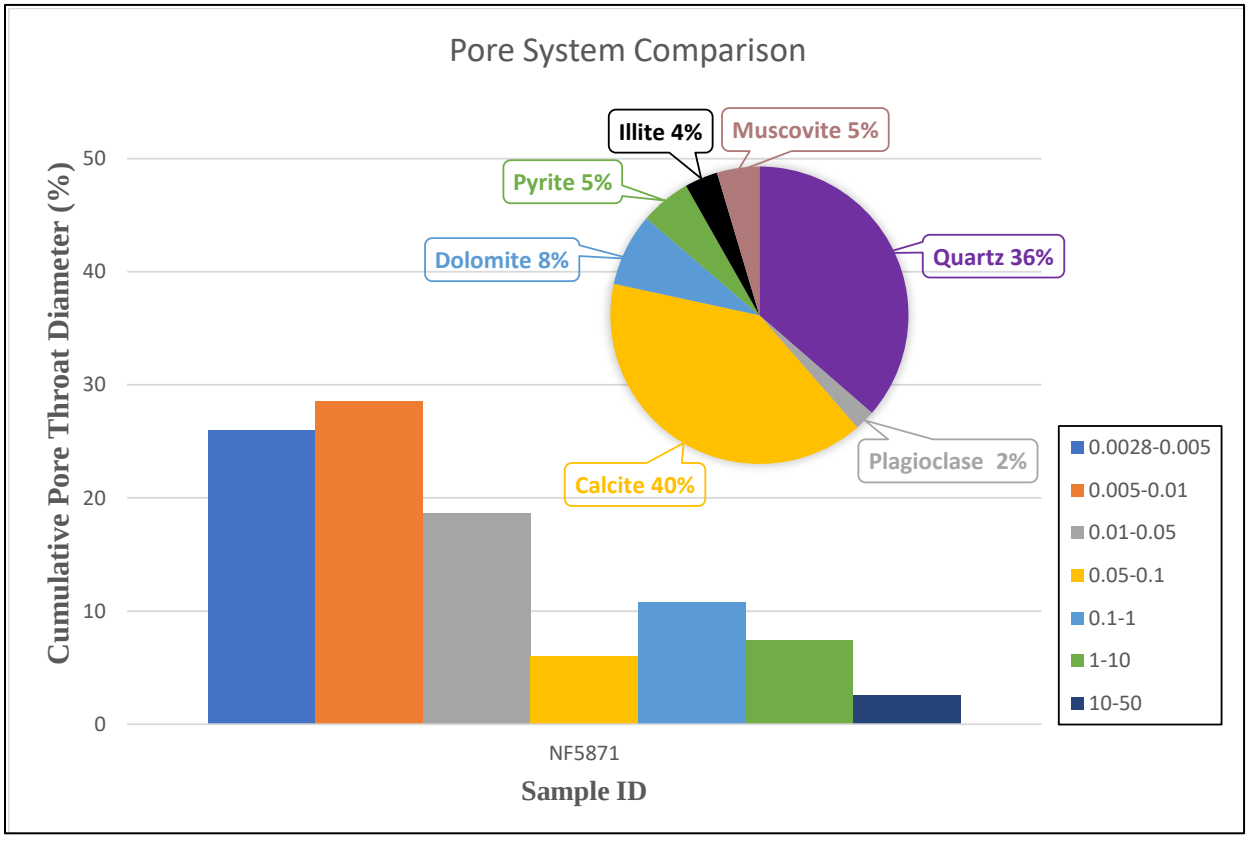

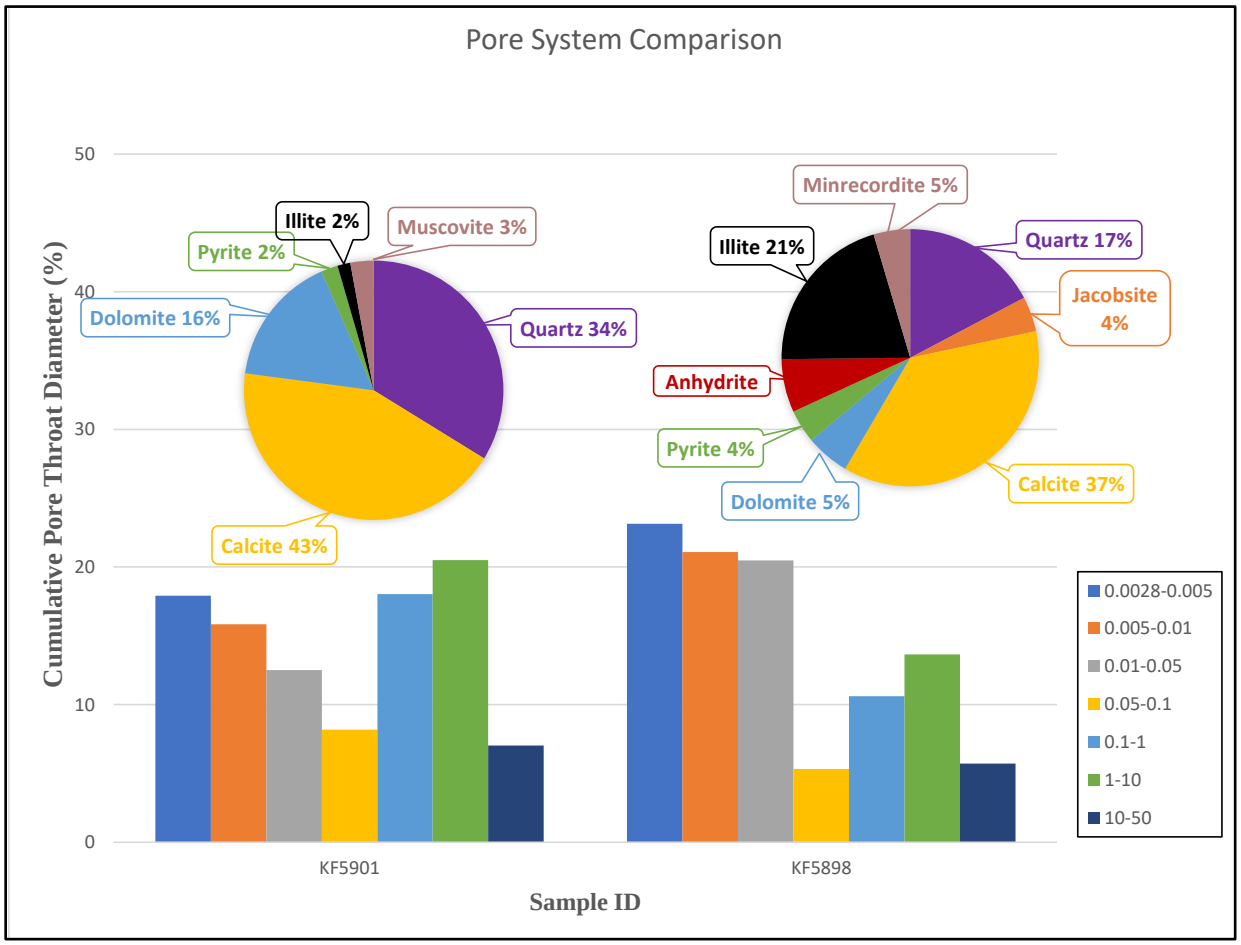
Pore System Comparison
Cumulative Pore Throat Diameter (%)
50
40
30
20
10
0
Illite 2%
Muscovite 3%
Pyrite 2%
Dolomite 16%
Quartz 34%
Calcite 43%
Minrecordite 5%
Illite 21%
Quartz 17%
Jacobsite 4%
Anhydrite
Pyrite 4%
Dolomite 5%
Calcite 37%
KF5901
KF5898
Sample ID
0.0028-0.005
0.005-0.01
0.01-0.05
0.05-0.1
0.1-1
1-10
10-50

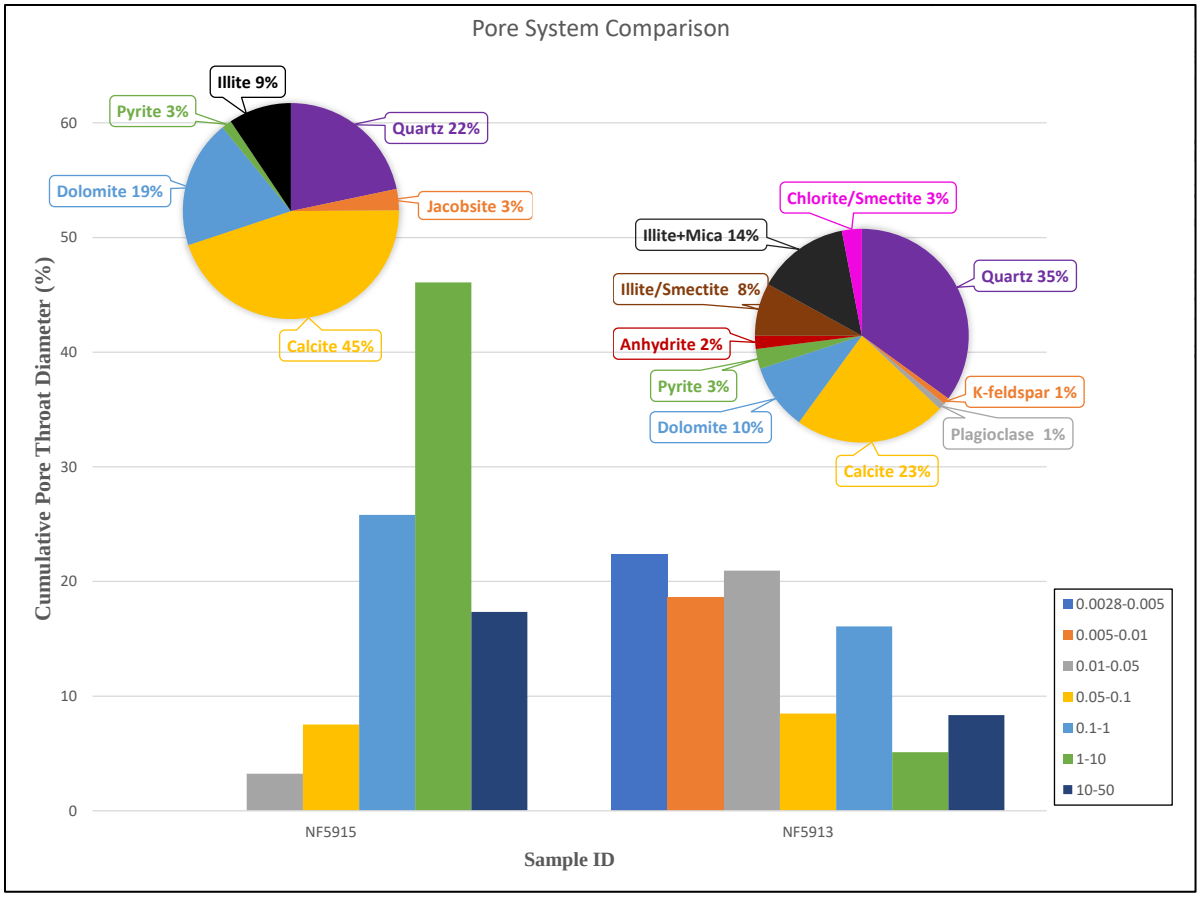
Pore System Comparison
Illite 9%
Pyrite 3%
Quartz 22%
Dolomite 19%
Jacobsite 3%
Calcite 45%
Chlorite/Smectite 3%
Illite+Mica 14%
Quartz 35%
Illite/Smectite 8%
Anhydrite 2%
Pyrite 3%
K-feldspar 1%
Dolomite 10%
Plagioclase 1%
Calcite 23%
Cumulative Pore Throat Diameter (%)
60
50
40
30
20
10
0
NF5915
NF5913
Sample ID
0.0028-0.005
0.005-0.01
0.01-0.05
0.05-0.1
0.1-1
1-10
10-50

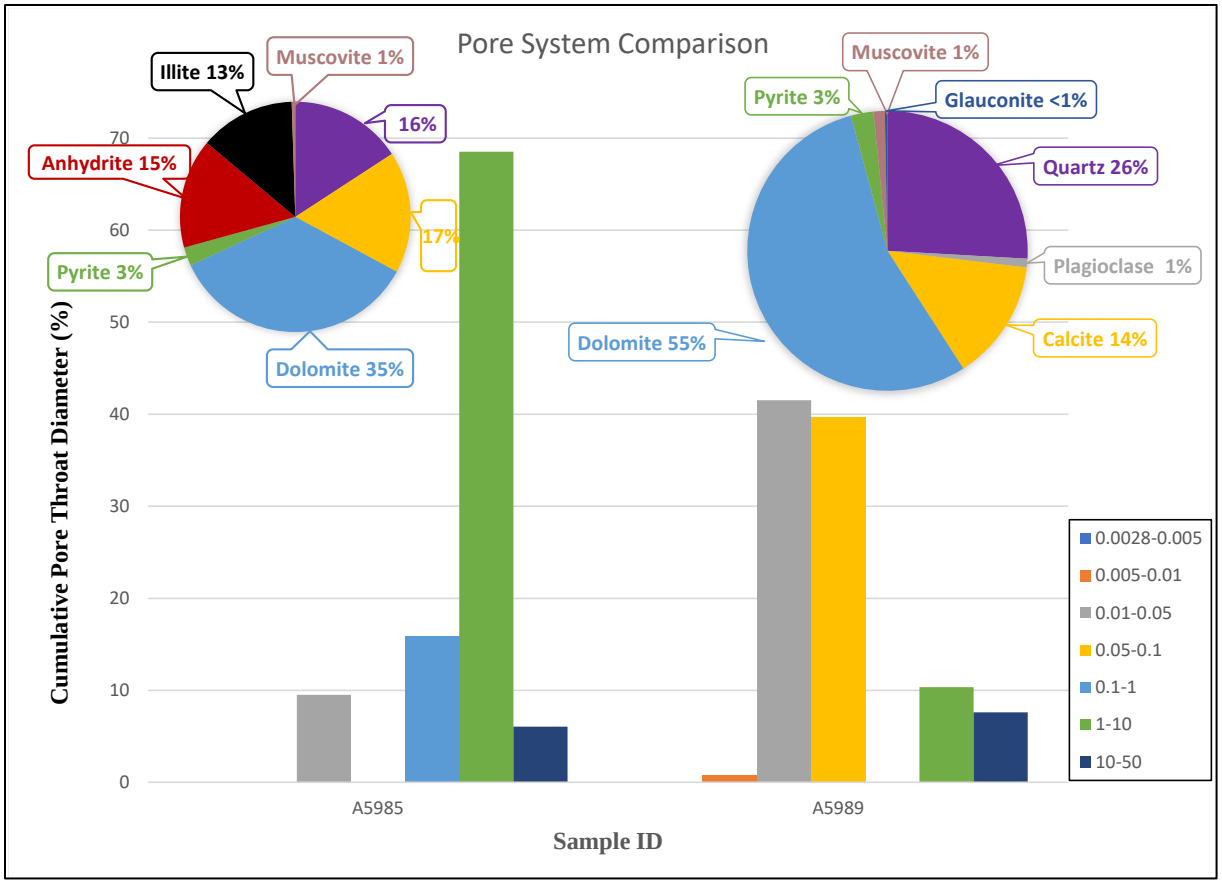
Pore System Comparison
Illite 13%
Muscovite 1%
16%
Anhydrite 15%
17%
Pyrite 3%
Dolomite 35%
Muscovite 1%
Pyrite 3%
Glauconite <1%
Quartz 26%
Plagioclase 1%
Dolomite 55%
Calcite 14%
Cumulative Pore Throat Diameter (%)
0
10
20
30
40
50
60
70
A5985
A5989
Sample ID
0.0028-0.005
0.005-0.01
0.01-0.05
0.05-0.1
0.1-1
1-10
10-50

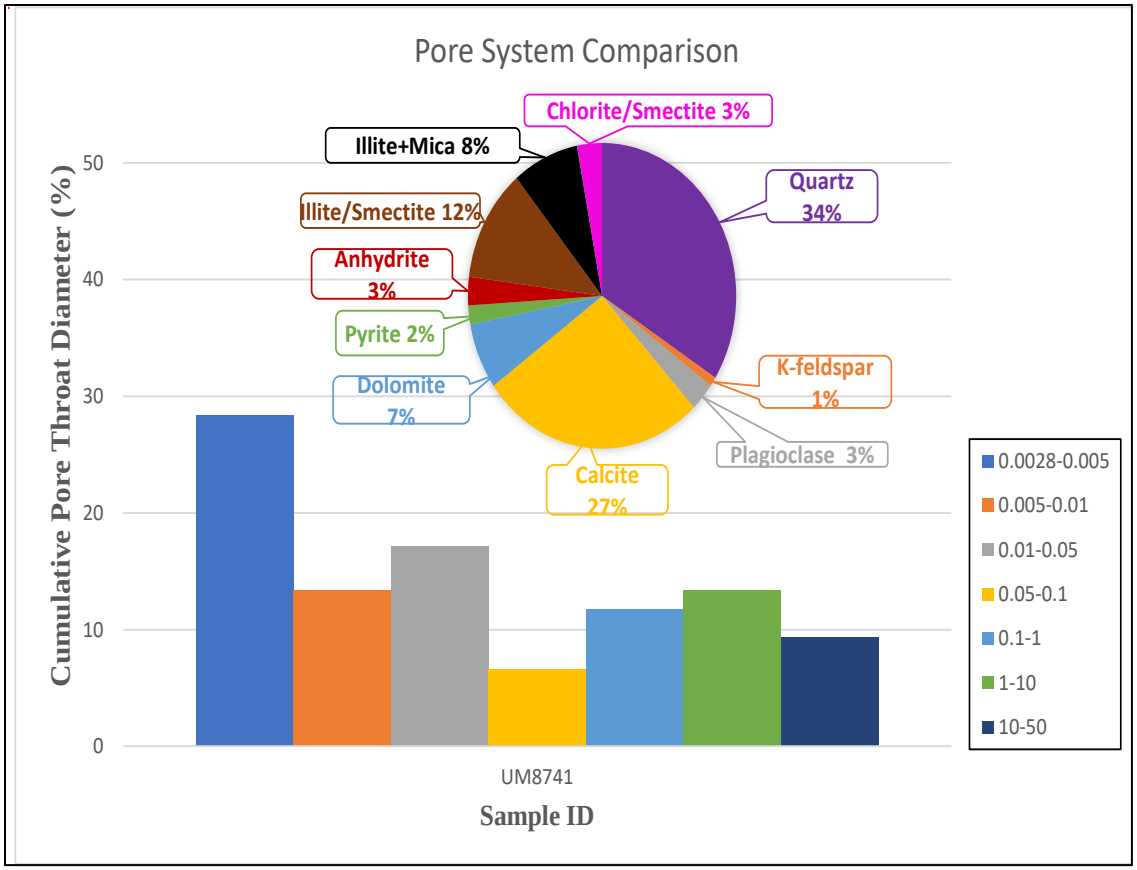


**Figure 5-5.** Mineralogy of samples compared to pore size distribution.

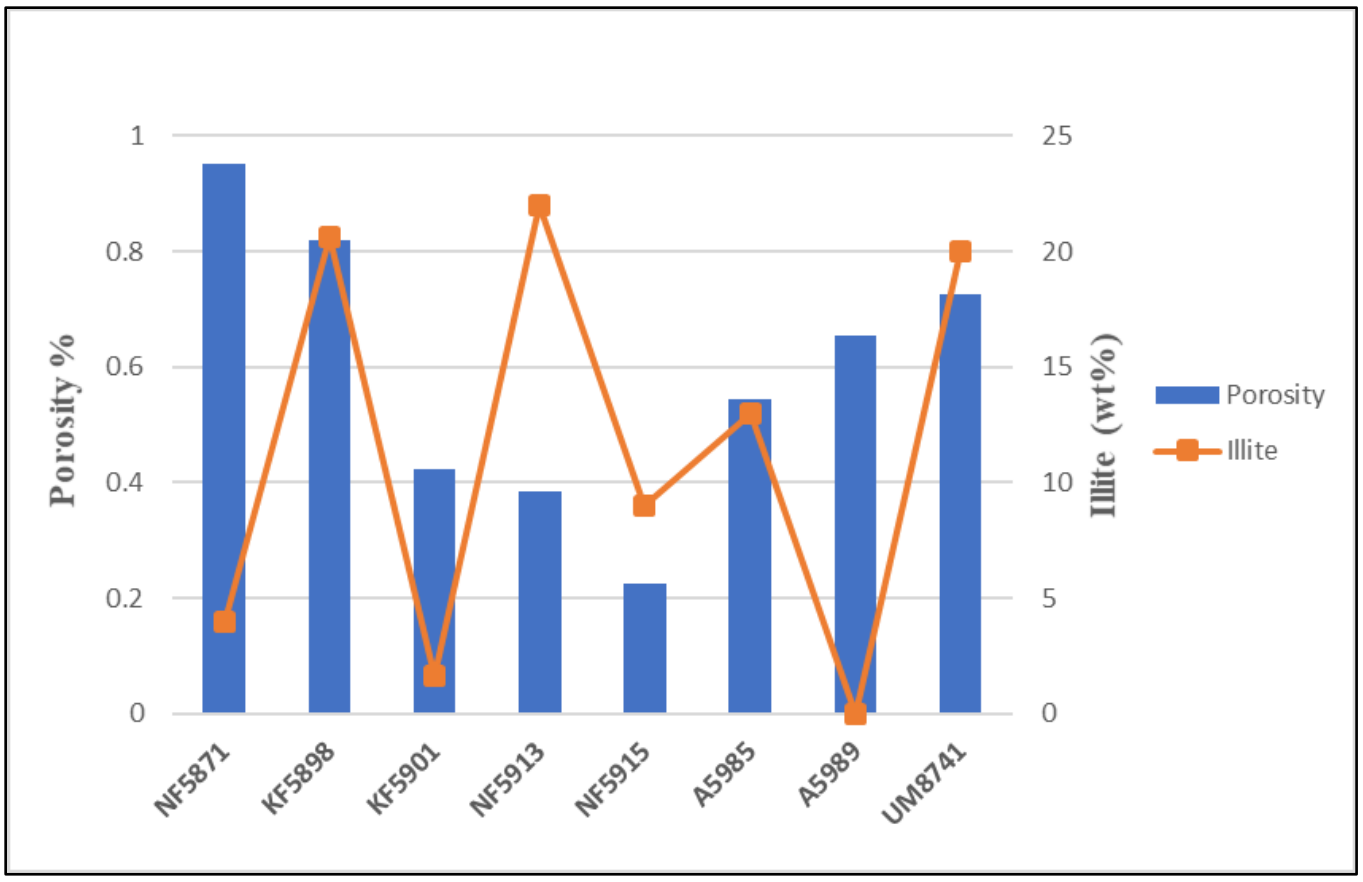


**Figure 5-6.** Porosity compared to illite percentage.

*5-3 Pore Connectivity*

Further examination of the matrix connectivity (stage III) with mineralogy (carbonate, clay, and quartz) provided correlations (Figure 5-7). Samples, A5985, A5989, and KF5898 show poor connectivity with both DI water and n-decane. These samples contained a lower percentage of quartz and were dominated by carbonates, with at least a 2:1 ratio of carbonate minerals to quartz. Carbonates and the matrix connectivity displayed a strong negative correlation - as carbonates increased, the pore connectivity worsened in oil-wet pores. Furthermore, there was no relationship between carbonates and pore connectivity in water-wet pores.

For samples NF5871, KF5901, UM8741, and NF5913, a poor connectivity with DI water was found; however, these samples showed good connectivity to n-decane. These samples had roughly a 1.5:1 ratio when comparing carbonate minerals to quartz. Represented by a correlation coefficient of 0.76, a strong relationship between quartz and pore connectivity was observed. As quartz mineral content increases, pore connectivity improves in oil-wet pores.

An outlier in the dataset, sample NF5915, had good pore connectivity with both DI water and n-decane. This is believed to be due to clay content, which only influenced the connectivity of water wet pores. A correlation coefficient of -0.50 displayed a strong negative correlation between clay and connectivity of water wet pores. When quartz and carbonates are close to a 1:1 ratio with a low clay content (<10%), this unusual connectivity was found. Table 5-1 shows the carbonates, clays, and quartz percentage of each sample, and stage III slopes.

**Table 5-1.** Mineralogy % and stage III slopes.

| Sample ID | *A5989* | *KF5898* | *A5985* | *NF5871* | *NF5913* | *KF5901* | *UM8741* | *NF5915* |
|---|---|---|---|---|---|---|---|---|
| **Clay Content (%)** | 2 | 21 | 13 | 8.2 | 25 | 4.5 | 20 | 9 |
| **Carbonate (%)** | 69 | 42 | 52 | 48 | 33 | 59 | 34 | 33 |
| **Quartz (%)** | 26 | 17 | 16 | 36 | 35 | 34 | 34 | 35 |
| **Connectivity Slope (n-decane)** | 0.249 | 0.259 | 0.35 | 0.435 | 0.458 | 0.503 | 0.575 | 0.594 |
| **Connectivity Slope (DI water)** | 0.19 | 0.223 | 0.246 | 0.276 | 0.277 | 0.283 | 0.384 | 0.532 |

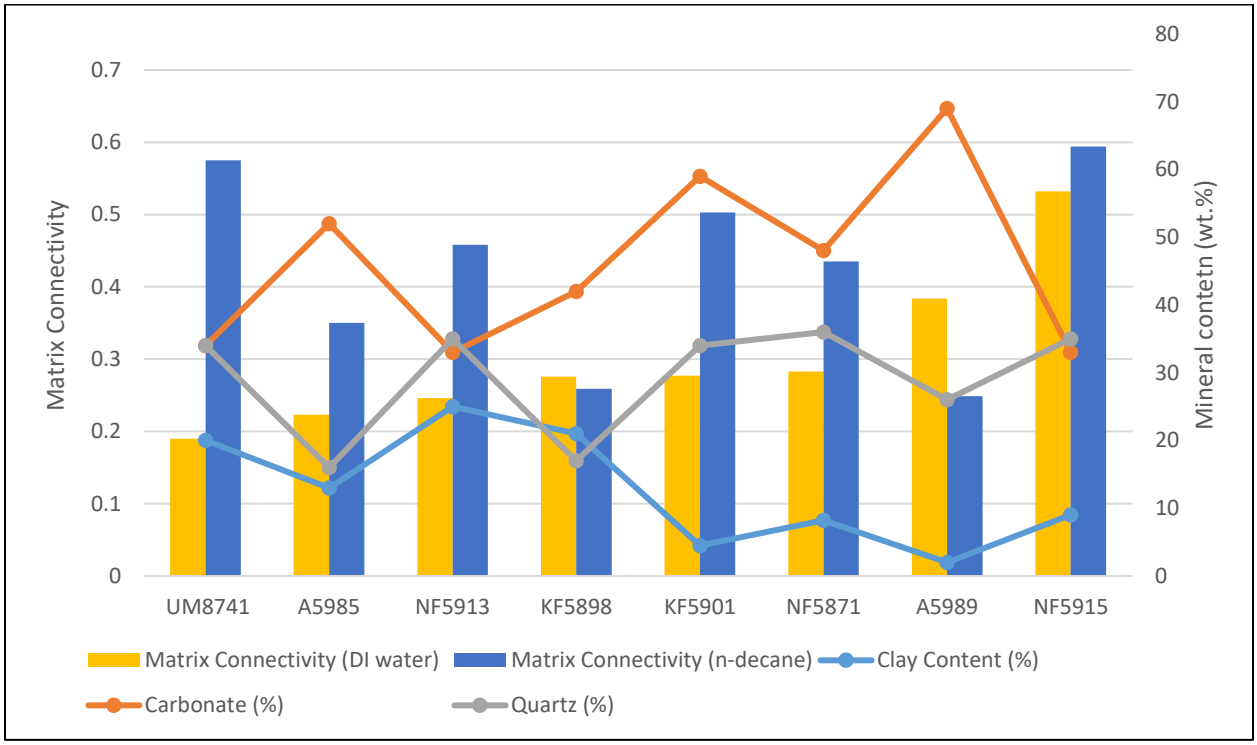


**Figure 5-7.** Examination of matrix connectivity and mineralogy.

*5-4 Porosity and Permeability*

Porosity plays an important role in geology. It controls fluid storage, and the extent and connectivity of the pore structure control fluid flow and transport through geological formations. In order to quantify the relationships between porosity, storage, transport and rock properties, however, the pore structure must be measured and quantitatively described. The primary goal in pore assessment is to quantify these pores and how they contribute to the overall fabric of the rock and its ability to transmit fluids, and the bulk physical properties of the rock itself. Anovitz (Anovitz 2015) notes how porosity has become difficult to quantify due to its range of magnitude (i.e. nanometer to 100s cm or larger).

Quantifying the porosity of geologic materials, has become more difficult as there has been an increase in the complexity of analysis. Porosity measurements in the Gothic shale vary significantly, ranging from 0.224 to 1.763%, different values were obtained between MICP and helium porosity (Table 5-2) showing the difficulty in quantifying porosity. Helium porosity consistently showed higher porosity values.

**Table 5-2.** Porosity Comparison

| Sample ID | MICP Porosity | He Porosity |
|---|---|---|
| NF5871 | 0.951 | - |
| NF5873 | 0.611 | - |
| KF5898 | 0.821 | 0.941 |
| KF5901 | 0.422 | - |
| NF5913 | 0.384 | - |
| NF5915 | 0.224 | 0.961 |
| A5985 | 0.543 | 0.814 |
| A5989 | 0.654 | - |
| UM8741 | 0.729 | 1.763 |

Permeability values were wide ranging with values from 0.002 to 29.485. Permeability values obtained via the helium method provided results significantly different results from the MICP arithmetic mean permeability values (Table 5-3).

**Table 5-3.** Permeability measurements with different methods.

| Sample ID | MICP Geometric k (uD) | Helium Permeability (mD) |
|---|---|---|
| NF5871 | 21.82 | - |
| NF5873 | 13.95 | - |
| KF5898 | 2.85 | 1.066 |
| KF5901 | 33.58 | - |
| NF5913 | 3.06 | - |
| NF5915 | 49.89 | 0.002 |
| A5985 | 9.72 | 29.485 |
| A5989 | 0.69 | - |
| UM8741 | 11.59 | 0.516 |

Loucks (2012) expanded the understanding of porosity by examining in detail very fine-grained, tight formations such as shale for hydrocarbon potential. Permeability pathways are porous, this enables hydrocarbons to migrate from induced fractures to the well bore. By means of a scatterplot chart (Figure 5-8) no correlation between permeability and MICP porosity was found.

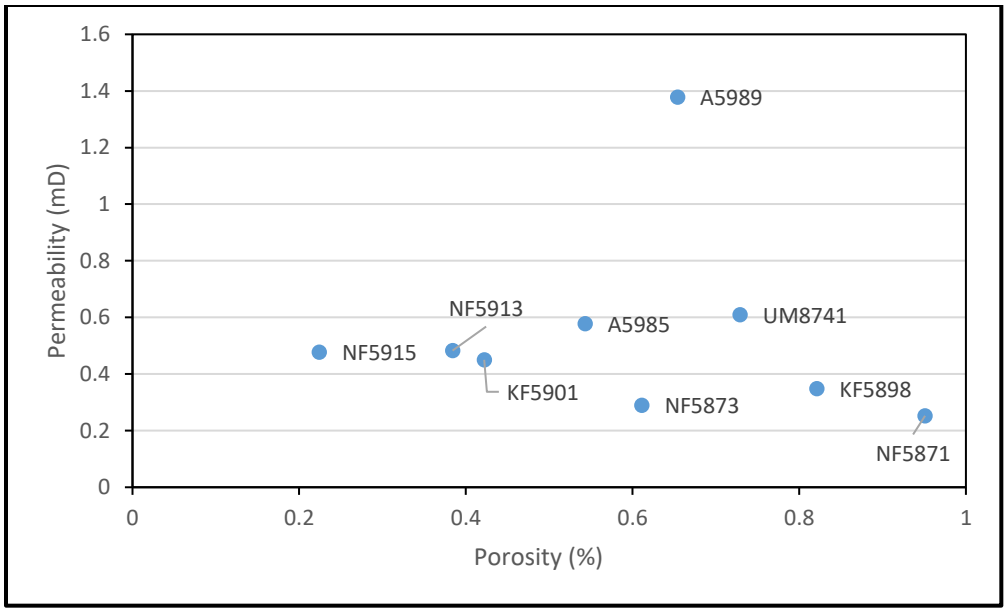


**Figure 5-8.** Porosity vs Permeability from MICP analyses.

Studies done on mature gas shales (Loucks et al., 2009), have proven that OM-hosted pores are a significant component of the pore system; therefore, we should expect to see a strong correlation between TOC and total porosity. Sample maturity ranged from mature-overmatured (Peters and Cassa 1994) however, there was no correlation between porosity and TOC (Figure 5-9).

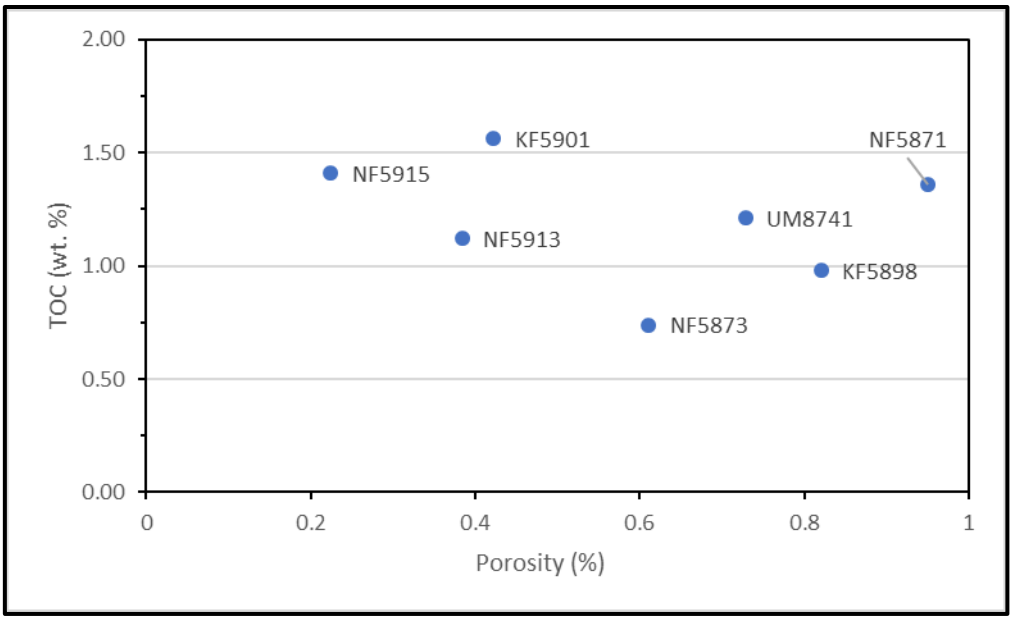


**Figure 5-9.** Porosity vs TOC.

As rocks mature, OM-hosted pores develop as hydrocarbons are expelled from the kerogen. The bitumen content in shale is indicted by the pyrolysis parameter S1, which represents the amount of free hydrocarbons (gas and oil) in the sample (Cao et al., 2015). Figure 5-10 compares S1 to MICP porosity values. A weak negative correlation is found, with a correlation coefficient -0.27. This negative correlation may represent bitumen occupying pore space as kerogen is broken down, which causes a negative impact on the overall porosity.

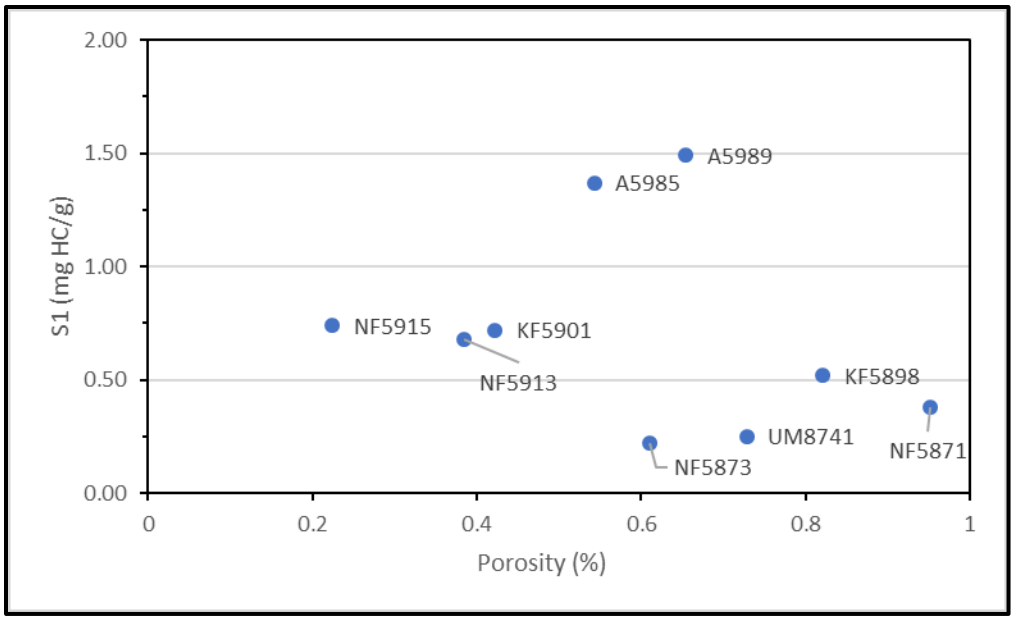


**Figure 5-10.** S1 vs Porosity.

Jarvie (2012) proposed the oil crossover line for unconventional reservoirs where S1 values (oil content) are plotted against TOC (organic richness). The oil crossover line is a one to one ratio, and formations above the line are expected to be productive. The idea behind his study is that oil or gas will adsorb to organic grains in the rock and a certain level of saturation is needed before unconventional oil wells are likely be productive (oil crossover or saturation index). Using the oil crossover ratio, all samples, except NF871, NF5873, and UM8741 would be productive (Figure 5-11). This does not match up with production history of the wells.

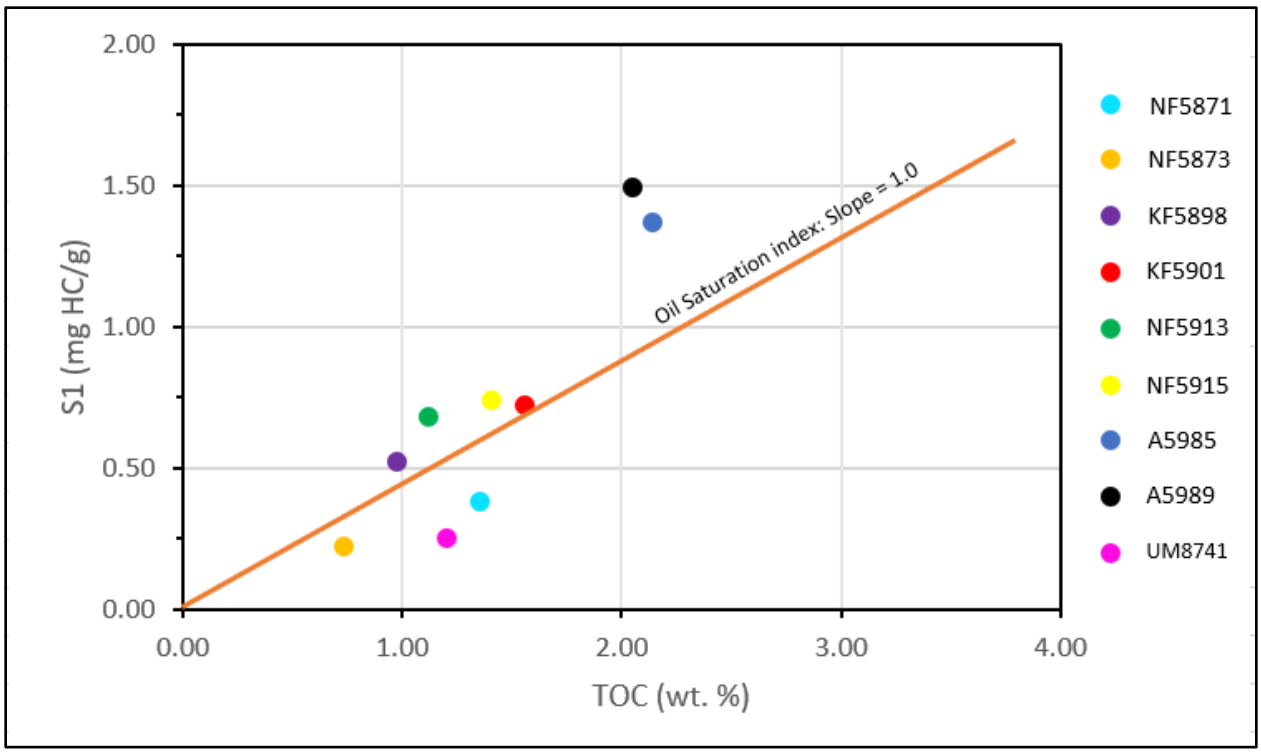


**Figure 5-11.** Jarvie (2012) oil crossover line of S1 vs. TOC.

# Chapter 6 – Conclusions

The Gothic shale interval was used to explore the pore structure of shale and to examine the effects of maturity and mineralogy on the pore systems. Petrophysical data was collected via XRD, pyrolysis, MICP, as well as contact angle measurements and spontaneous imbibition of both hydrophobic and hydrophobic fluids. Wettability tests were first conducted to determine sample affinities with different fluids such as API brine and 10% IPA. All samples tested show a better wettability to 10% IPA than API brine, except sample UM8741.

Imbibition tests were run using DI water and n-decane. DI water test for all samples showed poor connectivity except for sample NF5915. This sample was an anomaly and displayed good connectivity for both fluids. Although n-decane always indicated better connectivity than DI water, the results varied, showing both poor connectivity and good connectivity.

MICP tests were conducted on all samples to better understand the pore-throat size distribution and allowed an understanding of pores ranging in size from 2.8 nm to 50 μm. Most samples had pore types that were dominated by either micro-fractures, particularly 1-10 micrometer sized pores, or interclay platelet pores (5-2.8 nm sized pores).

Comparing pyrolysis results with MICP analyses, no correlation between maturity and pore size distribution could be found. Maturity levels range from peak maturity ($0.9 \sim R_o$) to over-mature ($R_o$ >1.35). To validate overall results, additional research needs to be conducted examining lower maturity levels of Gothic shale. Pyrolysis results, along with X-ray diffraction, conclude that most samples are dominated by carbonate minerals. Comparing mineralogy,

specifically the carbonate percentage, with pore-throat size distribution, no correlation could be identified.

Carbonates and the matrix connectivity displayed a strong negative correlation, as carbonates increased the pore connectivity worsened in oil-wetting pores. A strong relationship between quartz and pore connectivity is observed, as quartz content increases better pore connectivity in oil-wetting pores is found. Clay content only affects connectivity in water wet pores. A correlation coefficient of -0.50 display a strong negative correlation between clay and connectivity of water wet pores.

For the same samples, inconsistencies occur in porosity and permeability values. This may be based on the sample size (core plug versus cube sample). Larger samples allow micro fractures and laminations to play a greater role as compared to smaller samples. Helium porosity consistently showed higher porosity values than MICP porosity. Dataset also showed no correlation between permeability and MICP porosity. A weak negative correlation is found, with a correlation coefficient -0.27. The overall porosity is negatively impacted by the breakdown of kerogen into bitumen.

In order to gain a better understanding of the Gothic shale play more sampling of each formation needs to be done with the same exact study (e.g., sample size). To improve on these results a wider area of the Gothic shale formation needs to be investigated. Varying lithologies exist in the Gothic shale formation, and more data is needed to make generalizations about the wider area.

# Chapter 7 – Appendix

## *Appendix A - Methods and Procedures for X-ray Diffraction Analysis at the Shimadzu Center*

XRD patterns of the samples were collected on a Shimadzu MaximaX XRD-7000 powder X-ray diffractometer in the Shimadzu Center for Environmental, Forensics, and Material Science at the University of Texas at Arlington. The X-ray beam was set to a voltage of 40 kV and current of 30 mA and the scans were collected over a 2θ range of 2 to 70° with a step of 0.02 and a speed of 2° per minute. The samples were rotated at a speed of 6 RPM in order to maximize the irradiated volume of the sample and minimize any effects relating to potential heterogeneity in the sample powders. Soller slits with a 1° width were used between the beam and the sample (i.e., the divergence slit) and between the sample the monochromator (i.e., the scattering slit) and a 0.3 mm receiving slit was used between the monochromator and the detector to filter out extraneous X-rays.

The XRD patterns were post-processed in the MDI's Jade version 9 software. The minerals identified in the samples were identified by comparing the calculated 'd' values of various peaks in the collected spectra with those in the International Center for Diffraction Data's Powder Diffraction File-4 (PDF-4) database. Quantitative phase abundances were calculated using the built-in reference intensity ratio (RIR) method of the Jade software in conjunction with the PDF-4 database. The RIR method has been shown to produce results accurate to within ~±3 wt.% at the 95% confidence level under ideal conditions (Hillier, 2000).

# *Appendix B - Methods and Procedures of X-ray Diffraction Analysis at Weatherford Laboratories*

## *Bulk Sample Preparation*

### Spray Dry

A representative portion (6 grams minimum, preferably 10 grams) of each sample is selected for XRD analysis. Samples are disaggregated using mortar and pestle and portioned out for bulk and clay analyses. The bulk portion is ground into a slurry using a McCrone Micronizing Mill. The slurry is transferred to an air brush assembly and spray dried using a James Hutton Institute Spray Drying Oven. Randomly oriented spherical aggregates are then loaded into stainless steel sample holders. This method eliminates preferred orientation of minerals and allows for improved reproducibility of the bulk XRD patterns. [Sp. Ed. Bish, D. L. and Post, J. E. (1989); Hillier, S (2002b)].

### Minimal Material

A representative portion (2 grams minimum) of each sample is selected for XRD analysis. Samples are hand ground in an agate mortar and pestle to a fine powder. A portion of each ground sample is loaded into a stainless-steel sample holder, modified to accommodate a side loading method. This side loading method allows the sample to be sifted and promotes a random particle orientation, minimizing preferred orientation.

*Bulk/Whole Rock Analysis*

These bulk sample mounts are scanned with a Bruker AXS D4 Endeavor X-ray diffractometer using copper K-alpha radiation. To eliminate K-beta peaks and reduce background noise, nickel filter slits and air scatter screens are utilized, respectively. The scanning parameters for a bulk scan are from 5° 2θ to 70° 2θ at a step size of 0.02° per step. Full scanning parameters are defined below (for both bulk and clay):

- Operating voltage: 50Kv
- Operating amperage: 40mA
- Axial soller slit is in place
- Goniometer diameter: 400mm
- Lynx Eye High speed detector with a 2θ scanning range of 4°
- A nickel filter for K beta peaks
- An air scatter screen to reduce fluorescence
- Variable divergent slit at 0.3mm for bulk and 0.5mm for clay

Bulk Mineral Quantification

MDI Jade TM 9+ software and ICDD PDF 4+ 2015 database, with over 790,000 known compounds, are used to identify mineral phases present in the bulk diffractograms. Reference Intensity Ratio (RIR) method is used to quantify the whole rock. The RIRs (e.g., Mineral Intensity Factors (MIF)) are generated for each diffractometer using pure mineral standards mixed with quartz. The primary peaks of the minerals present are measured using the area under

the curve to one standard deviation (subtracting the background). When an uncommon mineral that is not in our RIR library and pure mineral standards are not available, whole pattern fitting with Rietveld refinement is applied.

X-ray diffraction cannot identify non-crystalline (amorphous) material, such as organic material and volcanic glass. However, samples containing a large amount of amorphous material show an anomalous “hump” in the XRD pattern. If further evaluations are required, Bruker AXS TOPAS v4.2 software is used to provide an estimate of the amount of amorphous material. Scans undergo full-pattern-fitting and Rietveld refinement using structure phase files previously identified by Jade and ICDD software (see above).

*Clay Sample Preparation*

An oriented clay fraction mount is prepared for each sample from hand ground powder. The samples are treated with a small amount of sodium hexametaphosphate as a deflocculant mixed with distilled water. The samples are then physically dispersed using a Fisher Scientific Ultra Sonifier to bring the clays into suspension. The samples are sized fractionated by centrifuging. After centrifuging, the supernatant containing the less than 2 micron clay fraction is vacuumed through a filter membrane glass tube that collects the solids on to a millipore filter.

These oriented solids are mounted on glass slides producing highly uniform diffraction mounts [Drever, 1973]. The glass slides are loaded into desiccant bowls containing 99.9% ethylene glycol for an extended period of time at a temperature of 110°C. The samples are loaded directly from the desiccant bowl to ensure maximum sample glycolation. The glycolated clays are also scanned in a Bruker AXS diffractometer using the following scan parameters: 2° 2θ to 30° 2θ at a step size of 0.02° per step. After the glycolated slide is scanned, the slides are

heat-treated in a furnace at 375°C for one hour and rescanned at the same clay parameters stated above. This process aids in identifying the expandable, water-sensitive minerals. When samples contain high levels of carbonates combined with low clay quantities, we may need to return to the sample and remove the carbonates to obtain a better clay scan for accurate identification and quantification.

*Clay Mineral Identification and Quantification*

Mixed-layer clays, particularly illite/smectite (I/S) are identified following the multiple peak method of Moore and Reynolds (1997). This entails measuring the 001/002 and 002/003 peaks of the illite/smectite. NEWMOD clay mineral generation program is used to create theoretical clay patterns, clay mixtures, and illite crystallinity. Identification of the amount of smectite (percent expandability) is also verified using the heat treated diffractogram overlain on the glycolated diffractogram in MDI Jade.

Kaolinite and chlorite are identified by the relative proportions of the peaks at 3.59 Å (kaolinite 002) and 3.54 Å (chlorite 004).

Clay mineral quantification includes: (1) the actual amount of discrete clay mineral species in the sample, and (2) the "expandability" or amount of smectite in mixed-layer clays, if present. Illite/Smectite (I/S) is the most common mixed-layer clay, but there are also chlorite/smectite (corrensite) and kaolinite/smectite. There are several tables in Moore and Reynolds (1997) that list 2θ positions and their correlative percent smectite in I/S (Table 8.3, p.273) or C/S (Table 8.4, p.281).

The Mineral Intensity Factor (MIF) method of Moore and Reynolds (1997) is applied to quantify the clay species. Weatherford has calculated MIFs for most clay minerals encountered.

The area of the specific mineral peak being used is divided by the MIF in the quantification process. The clay species is normalized to the total clay value derived from the bulk analysis.

Appendix Reference

Bish D.L. and Reynolds R.C. Jr. (1989) Sample preparation for X-ray diffraction. Pp. 73-99 in: Modern Powder Diffraction (D.L. Bish and J.E. Post, editors) Reviews in Mineralogy, Volume 20, Mineralogical Society of America, USA.

Drever, James I. (1973) The Preparation of Oriented of Clay Mineral Specimens for X-ray Diffration Analysis by a Filter-Membrane Peel Technique.

Hillier S. (2002b) Spray drying for X-ray powder diffraction specimen preparation. IUCR Commission on Powder Diffraction Newsletter No. 27. June 2002.

Moore, D.M. and Reynolds, R.C. (1997) X-ray Diffraction and the Identification and Analysis of Clay Minerals, 2nd edition. Oxford University Press, Oxford, 332 pp.

# *Appendix C - Methods and Procedures for Geochemical Analysis at Weatherford Laboratories*

## *Rock Sample Preparation*

Samples for Total Organic Carbon (TOC) and/or Programmed Pyrolysis may each require varying levels of sample preparation. Groups of samples are evaluated as to their respective condition as received and are handled differently depending on the various types of contaminants, lithologies, and analytical objectives. Samples are not high-graded prior to grinding unless specifically instructed by the client. When necessary and as instructed, water washing may be required to remove water-based mud. Solvent washing can be utilized to remove oil-based and/or synthetic-based mud. Additional solvent extraction of the crushed rock will be necessary to completely remove the contaminating oil-based and/or synthetic-based mud. Sample picking may also be necessary to remove lost circulation material or known cavings. Samples for TOC and Programed Pyrolysis are then ground to pass through a fine mesh sieve prior to analysis.

## *Total Organic Carbon*

Approximately 0.10 g of crushed rock is accurately weighed and then digested with concentrated hydrochloric acid to remove all carbonates from the sample. At this point, gravimetric carbonate content can be determined if requested. Following digestion, the sample is washed through a filtering apparatus, placed in a combustion crucible and dried. After drying, the sample is analyzed with a LECO Carbon Analyzer with detection limits to 0.01 weight percent. Standards and sample duplicates are tested regularly to assure superior instrument performance.

*Programmed Pyrolysis (Rock-Eval II, Rock-Eval VI, Source Rock Analyzer)*

Programmed pyrolysis (Rock-Eval and SRA) is performed to assess source rock quality and thermal maturity (e.g., Peters, 1986; Peters and Casa, 1994). In programmed pyrolysis, crushed rock samples are heated in an inert environment to determine the yield of hydrocarbons and CO2. The sample is initially held isothermally at 300°C for 3 minutes, producing the S1 peak by vaporizing the free (unbound) hydrocarbons. High S1 values indicate either large amounts of kerogen-derived bitumen (as in an active source rock) or the presence of migrated hydrocarbons. The oven then increases in temperature by 25°C/minute to a final temperature of approximately 600°C, depending on the instrument type. During this time, hydrocarbons that evolve from the sample as a function of the pyrolytic degradation of the kerogen are measured, generating the S2 peak and is proportional to the amount of hydrogen-rich kerogen in the rock. The temperature at which the S2 peak reaches a maximum, "T max ", is a measure of the source rock maturity. Accuracy of T max is 1-3°C, depending on the instrument, program rate and sample size, but can also vary by organic matter type. Tmax values for samples with S2 peaks less than 0.2 mg HC/g rock is often inaccurate and should be rejected unless a definitive kerogen peak is noted from the pyrogram. Any carbon dioxide released between 300° and 390°C is also measured, generating the S3 peak, providing an assessment of the oxygen content of the rock. In addition to the standard programmed pyrolysis method, we have several additional methods available designed to provide the client with additional useful information as it relates to the geochemical nature and potential of a rock sample including but not limited to TOC quantification, Carbonate quantification, Reservoir Oil Quality, APIR and Kerogen Kinetic analyses. A summary of analytical results from Programmed Pyrolysis follows.

S1: free oil content (mg hydrocarbons per gram of rock)

S2: remaining hydrocarbon potential (mg hydrocarbons per gram of rock)

S3: organic carbon dioxide (mg CO 2 per gram of rock)

TOC: total organic carbon content (wt. %)

Tmax: temperature at maximum evolution of S2 hydrocarbons

Ratios: hydrogen index (HI), oxygen index (OI), production index (PI),

S2/S3, and S1/TOC

*Vitrinite Reflectance and Visual Kerogen Assessment*

Visual kerogen assessments complement chemical assessments by recording information from the discrete particles (macerals) that make up the sedimentary organic matter. Vitrinite macerals are particles of sedimentary organic matter derived from wood, and their reflectance of incident light under oil immersion is used to assess the thermal maturity of a sample. Vitrinite reflectance (%Ro) increases with increased depth of burial (i.e., increased thermal exposure), and is an indication of the maximum temperature to which these particles have been exposed. The reflectance microscope measures the amount of reflected light relative to the incident light and expresses this ratio as a percentage. Vitrinite reflectance values range from about 0.25% (immature) to a high of about 5 or 6% (very mature). A population of vitrinite particles is found in almost all rock samples of Devonian or younger age (older samples pre-date the evolution of land plants, the source of vitrinite). Selecting the appropriate vitrinite population for subsequent reflectance measurements is a somewhat subjective process. The in-situ population must be identified, and must exclude vitrinite derived from cavings and reworked organic matter.

Reworked vitrinite that was redeposited in the sediments may have higher reflectance that will skew the measurements towards higher R o values if not recognized and removed from the average. In cuttings samples, cavings from overlying less mature sediments may skew the average towards lower values. Generally, when cavings are excluded, the lowest reflecting population is found to be indicative of the indigenous population, but this evaluation is made in combination with visual kerogen assessments, Rock-Eval Tmax measurements, and data for the extent of kerogen conversion.

Vitrinite reflectance values are divided into the following stages of thermal maturity:

| *Stage* | *Reflectance Range* |
|---|---|
| Immature | 0.2% to 0.6% |
| Oil window maturity | 0.6% to 1.1% |
| Condensate or wet-gas window | 1.1% to 1.4% |
| Dry gas window | 1.40% plus |

Thermal alteration indices (TAI) are determined from the color of organic matter when viewed under transmitted light through a strewn slide mount of kerogen. Lighter colored organic matter is indicative of low maturity, whereas darker material is indicative of higher thermal maturity.

Maceral composition is an assessment of the percentages of various organic particles found in kerogen samples. These particles are related to the oil and gas potential of the organic matter and are generally described as amorphous, exinitic, vitrinitic, inertinitic, or solid bitumen percentages. The former two macerals are primarily oil-prone particulate matter, whereas vitrinitic particles are indicative of gas-prone organic matter. Inertinitic matter is very hydrogen-poor and has no potential for generation of commercial quantities of hydrocarbons. The presence

of solid bitumen is indicative of in situ generated hydrocarbons, migrated hydrocarbons, or contamination. Other observations from visual kerogen assessment include the quality of the organic matter (oxidized, well preserved), and the presence of palynomorphs (which can reveal key aspects of the depositional environment).

# *Appendix D - Methods and Procedures for Geochemical Analysis at GeoMark Research*

## 1. Sample Requirements for a Typical Geochemical Program

For geochemical analysis a teaspoon (ca., 10 g) of sample material is needed when TOC, Rock-Eval, vitrinite reflectance and residual hydrocarbon fluid fingerprinting is to be completed. If possible, a tablespoon is preferred. However, it is possible to complete a detailed program with even less sample, although there is dependent on the sample characteristics (e.g., organic richness, abundance of vitrinite, amount of staining). Sample prep includes grinding the sample with mortar and pestle until it passes through a 60-mesh sieve.

## 2. Total Organic Carbon (TOC) – LECO C230 instrument

Leco TOC analysis requires decarbonation of the rock sample by a treatment with hydrochloric acid (HCl). This is done by treating the samples with concentrated HCl for at least two hours. The samples are then rinsed with water and flushed through a filtration apparatus to remove the acid. The filter is then removed, placed into a LECO crucible and dried in a low temperature oven (110 $^{o}$C) for a minimum of 4 hours. Samples may also be weighed after this process in order to obtain a % carbonate value based on weight loss.

The LECO C230 instrument is calibrated with standards having known carbon contents. This is completed by combusting these standards by heating to 1200$^{o}$C in the presence of oxygen. Both carbon monoxide and carbon dioxide are generated, and the carbon monoxide is

converted to carbon dioxide by a catalyst. The carbon dioxide is measured by an IR (infra-red) cell. Combustion of unknowns is then completed and the response of unknowns per mass unit is compared to that of the calibration standard, thereby the TOC is determined.

Standards are analyzed as unknowns every 10 samples to check the variation and calibration of the analysis. Random and selected reruns are done to verify the data. The acceptable standard deviation for TOC is 3% variation from established value.

**3. Rock Eval / HAWK Pyrolysis**

Approximately 100 milligrams of washed, ground (60 mesh) whole rock sample is analyzed in the Rock-Eval or HAWK instrument. Organic-rich samples are analyzed at reduced weights whenever the S2 value exceeds 40 mg/g or TOC exceeds 7-8%. Samples must be re-analyzed at lower weights when these values are obtained at 100 mg.

**RE-II Operating Conditions**

S1: 300$^{o}$C for 3 minutes

S2: 300$^{o}$C to 550$^{o}$C at 25$^{o}$C/min;
hold at 550$^{o}$C for 1 minute

S3: trapped between 300 to 390$^{o}$

**RE-VI Operating Conditions**

S1: 300°C for 3 minutes

S2: 300°C to 650°C at 25°C/min;

hold at 650°C for 0 minute

S3: measured between 300 to 400°

**HAWK Operating Conditions**

S1: 300°C for 3 minutes

S2: 300°C to 650°C at 25°C/min;

hold at 650°C for 0 minute

S3: measured between 300 to 400°

Measurements from Rock-Eval are:

S1: free oil content (mg HC/g rock)

S2: remaining generation potential (mg HC/g rock)

$T_{max}$: temperature at maximum evolution of S2 hydrocarbons (°C)

S3: organic carbon dioxide yield (mg $CO_2$/ g rock)

Several useful ratios are also utilized from Rock-Eval and TOC data. These are:

Hydrogen Index (HI): S2/TOC x 100 (in mg HC/g TOC)

Oxygen Index (OI): S3/TOC x 100 (in mg CO2/g TOC)

Normalized Oil Content: S1/TOC x 100 (in mg HC/g TOC)

S2/S3:

Production Index (PI): S1/ (S1+S2)

Instrument calibration is achieved using a rock standard. Its values were determined from a calibration curve to pure hydrocarbons of varying concentrations. This standard is analyzed every 10 samples as an unknown to check the instrument calibration. If the analysis of the standard ran as an unknown does not meet specifications, those preceding data are rejected, the instrument recalibrated, and the samples analyzed again. However, normal variations in the standard are used to adjust any variation in the calibration response. The standard deviation is considered acceptable under the following guidelines:

$T_{max}$: $\pm 2^{o}C$

S1: 10% variation from established value

S2: 10% variation from established value

S3: 20% variation from established value

Analytical data are checked selectively and randomly. Selected and random checks are completed on approximately 10% of the samples. A standard is analyzed as unknown every 10 samples.

**4. Turnaround Time:**

The standard turnaround time for sample orders over the past 12 months is approximately 2 to 3 weeks, depending on number of samples in the order.

# Chapter 8 – References

American Petroleum Institute Recommended Practice (API RP) 40. 1998. Recommended Practice for Core Analysis (2nd Ed.). Am. Petrol. Inst., Washington, DC.

Anna, L.O., P.G. Lillis, K.M. Pearson, and K.J. Whidden. 2011. Assessment of Undiscovered Oil and Gas Resources in the Paradox Basin Province, Utah, Colorado, New Mexico, and Arizona, 2011. United States Geological Survey. http://energy.cr.usgs.gov/oilgas/noga/.

Anovitz, L.M., and D.R. Cole, 2015, Characterization and Analysis of Porosity and Pore Structures: Reviews in Mineralogy and Geochemistry, v. 80, p. 61-164. doi:10.2138/rmg.2015.80.04.

Baars, D.L., J.W. Parker, and J. Chronic. 1967. Revised stratigraphic nomenclature of Pennsylvanian System, Paradox Basin. AAPG Bulletin, 51(3): 393-403.

Baars, D.L., and G.M. Stevenson. 1981. Tectonic Evolution of the Paradox Basin, Utah and Colorado, in Wiegand, D.L. (ed.), Geology of the Paradox Basin: Rocky Mountain Association of Geologists, p. 23-31.

Binazadeh, M., D. Bryan, H. Dehghanpour, A. Habibi, and G. Uswak. 2016. Advances in Understanding Wettability of Tight Oil Formations: A Montney Case Study. Society of Petroleum Engineers. Paper SPE 175157 presented at the SPE Annual Technical Conference and Exhibition, Houston, 28-30 September 2015. Revised manuscript received 7 March 2016.

Bevers, J. 2017. Nano-Petrophysics of the Hybrid Shale-Oil Bone Spring Formation, Lea County, New Mexico. M.S. Thesis, Department of Science, University of Texas at Arlington, USA.

Buckner, D.H., and R.J. Hite. 1981. Stratigraphic correlations, facies concepts, and cyclicity in Pennsylvanian rocks of the Paradox basin, in Wiegand, D.L., ed., Geology of the Paradox Basin: Rocky Mountain Association of Geologists, pp. 147-159.

Cao, T., Song, Z., Wang, S., Cao, X., Li, Y., and Xia, J. 2015. Characterizing the pore structure in the Silurian and Permian shales of the Sichuan Basin, China. Marine and Petroleum Geology, 61: 140-150.

Chidsey, T.C., Jr., C.D. Morgan, D.E Eby, J.N. Moore, L.H. Taylor, and J.D. Humphrey. 2009. Diagenetic analysis of the Leadville Limestone, Lisbon case-study field, *in* Chidsey, T. C., Jr. (ed.), The Mississippian Leadville Limestone exploration play, Utah and Colorado—Exploration techniques and studies for independents: Final Report for DOE Award No. DE-FC26-03NT15424, pp. 4-1–4-20.

Condon, S.M. 1997. Geology of the Pennsylvanian and Permian Cutler Group and Permian Kaibab Limestone in the Paradox Basin, southeastern Utah and southwestern Colorado: U.S. Geological Survey Bulletin 2000-P, pp. 1-46.

Condon, S.M., and V.F. Nuccio. 1996. Burial and thermal history of the Paradox Basin, Utah and Colorado, and petroleum potential of the Middle Pennsylvanian Paradox Formation. USGeological Survey Bulletin. 2000-O. pp. 1-41.

Coretest Systems. 2012. AP-608 Operator's manual, 6.1-7: d.

Eberle, A.P.R., D. Ertas, C. Huynh, H.E. King. Jr., C.E. Kliewer, and C.C. Walters. 2015. Pore architecture and connectivity in gas shale. Energy & Fuels. 29 (3): 1375–1390.

Gamero-Diaz, H., Miller, C.K., and Lewis, R., sCore: a mineralogy based classification scheme for organic mudstones. SPE Annual Technical Conference and Exhibition, Presentation at the Society of Petroleum Engineers, New Orleans, LA, USA, September 30, 2013, 10.2118/166284-MS.

Gao, Z.Y., and Hu, Q.., 2012, Using spontaneous water Imbibition to measure the effective permeability of building materials. Special Topics & Reviews in Porous Media: An International Journal, v. 3, p. 209, doi: 10.1615/SpecialTopicsRevPorousMedia.v3. i3.20.

Gao, Z.Y., and Hu, Q.H., 2013, Estimating permeability using median pore-throat radius obtained from mercury intrusion porosimetry. Journal of Geophysics and Engineering, v. 10, p. 025014.

Hu, Q.H., Persoff, P., and Wang, J.S., 2001, Laboratory measurement of water imbibition into low-permeability welded tuff. Journal of Hydrology, 242: 64-78.

Hu, Q.H., Ewing, R.P., and Dultz, S., 2012, Low pore connectivity in natural rock. Journal of Contaminant Hydrology, 133: 76-83.

Hu, Q.H., Ewing, R.P., and Rowe, H.D., 2015, Low nanopore connectivity limits gas production in Barnett formation. Journal of Geophysical Research: Solid Earth, 120: 8073-8087.

Hu, Q.H., Y.X. Zhang, X.H. Meng, Z. Li, Z.H. Xie, and M.W. Li. 2017. Characterization of multiple micro-nano pore networks in shale oil reservoirs of Paleogene Shahejie Formation in Dongying Sag of Bohai Bay Basin, East China. Petroleum Exploration and Development, 44(5): 720–730.

Jarvie, D. M. 2012, Shale resource systems for oil and gas: Part 2—Shale-oil resource systems, in J. A. Breyer, ed., Shale reservoirs—Giant resources for the 21st century: AAPG Memoir 97, pp. 89–119.

Jarvie, D., Claxton, B., Henk, F., and Breyer, J., 2001, Oil and shale gas from the Barnett Shale, Fort Worth Basin, Texas: AAPG Annual Meeting Program, v. 10, p. A100.

Kathel, P., and K.K. Mohanty. 2013. Wettability alteration in a tight oil reservoir. Energy & Fuel. 27 (11): 6460-6468. http://dx.doi.org/10.1021/ef4012752.

Klinkenberg, L.J. 1941. The permeability of porous media to liquids and gases. Drilling and Production Practice. 57–73.

Loucks, R.G., R.M. Reed, S.C. Ruppel and D.M. Jarvie. 2009. Morphology, genesis, and distribution of nanometer-scale pores in siliceous mudstones of the Mississippian Barnett Shale. Journal of Sedimentary Research, 79(11-12): 848-861.

Loucks, R., Reed, R., Ruppel, S., and Hammes, U. 2012. Spectrum of pore types and networks in mudrocks and a descriptive classification for matrix-related mudrock pores. AAPG Bulletin, 96(6): 1071−107.

Manrique, E., C. Thomas, R. Ravikiran et al. 2010. EOR: Current Status and Opportunities. Presented at the SPE Improved Oil Recovery Symposium, Tulsa, 24-28 April. SPE-130113-MS. http://dx.doi.org/10.2118/130113-MS.

Peters, K.E. and Cassa, M.R. (1994) Applied Source-Rock Geochemistry. In: Magoon, L.B. and Dow, W.G., Eds., The Petroleum System. From Source to Trap, American Association of Petroleum Geologists, Tulsa, 93-120.

Tesoro, L. 2014. Will the Gothic Shale Ever Pan Out. DI Blog. http://info.drillinginfo.com/will-the-gothic-shale-pan-out/.

Villegas, R. 2016. Nanopetrophysics of the Niobrara Formation in Berthoud State #3 well of Colorado, USA. M.S. Thesis, Department of Science, University of Texas at Arlington, USA.

Wang, S., Javadpour, F., and Feng, Q., 2016, Confinement correction to mercury intrusion capillary pressure of shale nanopores. Scientific Reports, v. 6, p. 20160, doi: 10.1038/srep20160 [doi].

Washburn, E.W., 1921, Note on a Method of Determining the Distribution of Pore Sizes in a Porous Material. Proceedings of the National Academy of Sciences of the United States of America, 7: 115-116.